POLYTECHNIQUE MONTRÉAL

affiliée à l'Université de Montréal

Non-Planar Multinozzle Additive Manufacturing of Thermoset Composites

JEAN-FRANÇOIS CHAUVETTE

Département de génie mécanique

Thèse présentée en vue de l'obtention du diplôme de *Philosophiæ Doctor*

Génie mécanique

Avril 2023

© Jean-François Chauvette, 2023.

POLYTECHNIQUE MONTRÉAL

affiliée à l'Université de Montréal

Cette thèse intitulée :

Non-Planar Multinozzle Additive Manufacturing of Thermoset Composites

présentée par **Jean-François CHAUVETTE**

en vue de l'obtention du diplôme de *Philosophiæ Doctor*

a été dûment acceptée par le jury d'examen constitué de :

Louis LABERGE LEBEL, président

Daniel THERRIAULT, membre et directeur de recherche

Sylvain TURENNE, membre

Patricia KRAWCZAK, membre externe

DEDICATION

To all those who have ever given up,

and ultimately kept going.

ACKNOWLEDGEMENTS

I would especially like to thank my PhD supervisor, Prof. Daniel Therriault for recruiting me during the capstone project of my undergrad studies. I am extremely grateful to him for recognizing my potential and always believing in my abilities to complete this project from day one. His constructive criticism over the years has helped me realize my full potential and hone my interpersonal and professional skills, which will surely follow me throughout my career.

I would like to express my special thanks to Dr. Rouhollah D. Farahani. His unfailing support helped me a lot in the definition of my research project, the realization of experiments and the writing of scientific articles. I thank my other colleagues from the Objective 4 of the FACMO Chair, Mr. David Brzeski and Dr. Iee Lee Hia who conducted the material development of the two epoxy formulations used in this work. I could not have accomplished my project without their work and dedication. I also thank Dr. Nicola Piccirelli and Mr. Benoit Bazin, our industrial partners from the Safran Group, for their collaboration and for providing countless technical advice. I would also like to thank all of my colleagues and friends at the Laboratory for Multiscale Mechanics (LM²) with whom I have worked over the years or who have helped me in any way, especially Juliette Pierre, Alessandra Lingua, Olivier Duchesne, Filippo Iervolino, Paul Gregorio, Rui Tao, Josué Costa Baptista, Shibo Zou, Kambiz Chizari, Facundo Sosa-Rey, Gabriel Chenier and Yahya Abderrafai. I would also like to thank Benedict Besner, Yanik Landry-Ducharme, Tomy Arial, Christian Charles Martel, Moustapha Jadayel, Tanja Pelzmann and Nadine Bernardini for their technical and administrative assistance.

Funding of this work has been provided by the FACMO Chair supported by the Natural Sciences and Engineering Research Council of Canada (NSERC, CRDPJ 514761-1), the Canada Foundation for Innovation (CFI, Project #36450), the Government of Québec (Project #36450), and Safran Group (France). I would also like to acknowledge the company Mëkanic, especially Thierry Lafrance and Francis Trudeau-Lalonde for their technical participation to the project, without whom the results of this project would have been very difficult to achieve.

Finally, I would like to thank my partner Catherine, my parents, Hélène and Denis, and the rest of my family for their love, encouragement and support over the years.

RÉSUMÉ

Au cours de la dernière décennie, l'industrie aérospatiale a progressivement adopté des technologies de fabrication additive (FA) pour fabriquer des pièces fonctionnelles plus complexes tout en réduisant les déchets de matériaux qui étaient auparavant produits par les techniques traditionnelles de fabrication soustractive. Dans le monde de la recherche académique, la conception de systèmes d'impression avancés et le développement de matériaux ont contribué à faire progresser la FA des polymères et des composites et ont démontré leur potentiel pour la fabrication de pièces multifonctionnelles légères. Dans l'industrie aérospatiale, les revêtements d'étanchéité abradables en polymère thermodurcissable sont principalement utilisés dans la région en amont des moteurs d'avion pour réduire leur consommation spécifique de carburant en générant un faible jeu entre les pièces rotatives et le carter. Cependant, les méthodes d'application actuelles, telles que le pistolet pneumatique ou le procédé de moulage, ne permettent pas un contrôle total de la géométrie du revêtement. L'écriture directe d'encre (DIW) est une technique de FA qui permet l'extrusion de matériaux tels que des encres viscoélastiques, des hydrogels et certains composites thermodurcissables. Il a été démontré que la DIW permet la FA d'échantillons abradables à petite échelle (*i.e.*, de quelques centimètres de large) sous la forme d'un empilement périodique tridimensionnel (3D) de filaments à micro-échelle appelé micro-échafaudages. Ces micro-échafaudages abradables ont montré des capacités d'absorption acoustique qui pourraient être utilisées pour réduire le bruit produit par les avions. Cependant, la vitesse d'impression lente et le long temps d'impression souvent associés à ces structures complexes à haute résolution, combinés aux défis de la DIW des composites thermodurcissables (*e.g.*, la polymérisation, la viscosité, le temps de gélification), rendent difficile la mise à l'échelle des micro-échafaudages à l'échelle du mètre pour la FA d'un revêtement abradable réel de grande taille destiné aux carters courbés des avions. Par conséquent, l'objectif principal de cette recherche est de développer une méthode de FA non planaire pour l'impression 3D rapide d'un matériau thermodurcissable abradable, permettant la production d'un revêtement abradable léger sous la forme d'un grand réseau de micro-échafaudages, inspiré de motifs d'absorption acoustique. La méthode développée implique une tête d'impression multibuses montée sur un bras robotique à 6 axes pour permettre l'extrusion simultanée de 26 filaments sur la surface non planaire d'un carter d'avion. Un modèle de prédiction de la pression ainsi qu'un générateur de trajectoires d'outils non planaires pour les têtes d'impression

multibuses ont été programmés pour prédire le processus de FA, générer des trajectoires de robot à 6 axes pour la tête d'impression multibuses sur des substrats non planaires, et contrôler la géométrie du revêtement abradable afin d'obtenir de grands réseaux de micro-échafaudages courbes avec une porosité à plusieurs niveaux. Des réseaux de micro-échafaudages mesurant jusqu'à ~ 9×10^4 mm^2 ont été fabriqués à des vitesses d'impression allant jusqu'à 250 mm/s, ce qui est ~ 3 fois plus rapide que des travaux similaires publiés. Un micro-échafaudage épais de 50 couches a été étudié et a montré une erreur moyenne d'alignement de l'empilement des couches de 57 µm. La FA multibuses non planaire a permis la fabrication de réseaux de micro-échafaudages courbes sur une surface de rayon aussi petit que ~ 240 mm, avec une erreur de parcours de 15 µm. L'aboutissement de ces travaux a conduit à la création d'un démonstrateur de composant d'avion utilisant une approche de FA multiprocessus non planaire, qui présente un revêtement de réseau courbé de micro-échafaudages fonctionnels abradables, avec des dimensions de ~ 520 mm × 78 mm × 5,6 mm et un rayon de 962 mm, ce qui n'avait jamais été réalisé auparavant. Le développement d'une méthode de FA multibuses non planaire à grande échelle et les différentes études de cas imprimées en 3D présentées dans cette recherche augmentent le potentiel de conception à grande échelle de pièces multifonctionnelles pour une grande variété d'applications allant de la FA de structures architecturales en béton, l'ingénierie tissulaire, les canaux microfluidiques, et l'avancement de la FA multiprocessus.

ABSTRACT

Over the last decade, the aerospace industry has progressively adopted additive manufacturing (AM) technologies to manufacture more complex functional parts while reducing the material waste that was previously produced by traditional subtractive manufacturing techniques. In academia, the design of advanced printing frameworks and materials development have helped to advance the AM of polymers and composites and have demonstrated their potential for the fabrication of lightweight multifunctional parts. In the aerospace industry, thermosetting polymeric abradable seal coatings are mainly used in the upstream region of aircraft engines to reduce their specific fuel consumption by generating low tip clearance between rotating parts and the casing. Yet, current application methods such as pneumatic gun or molding process, do not allow full control of the coating geometry. Direct ink writing (DIW) is an AM technique that allows for the material extrusion of viscoelastic inks, hydrogels, and some thermosetting composites. It has been shown that DIW enables the AM of small-scale abradable samples (*i.e.*, few cm wide) in the form of a three-dimensional (3D) periodic microscale stacking of filaments called microscaffolds. These abradable microscaffolds have exhibited sound absorption capabilities that could be used to reduce noise produced by aircraft. However, the slow printing speed and long printing time often associated with these complex high-resolution structures paired with challenges of thermosetting composites DIW (e.g., polymerization, viscosity, gelation time) make it difficult to scale up microscaffolds to the meter scale for the AM of an actual large abradable coating destined for curved aircraft casings. Therefore, the main objective of this research is to develop a non-planar AM method for rapid 3D printing of an abradable thermosetting material, allowing the production of a lightweight abradable coating in the shape of a large microscaffold network, inspired by sound absorption patterns. The developed method involves a multinozzle printhead mounted on a 6-axis robotic arm to allow simultaneous material extrusion of 26 filaments on the non-planar surface of an aircraft casing. A pressure prediction model as well as a non-planar toolpath generator for multinozzle printheads were programmed to predict the AM process, generate 6-axis robot trajectories for multinozzle printhead on non-planar substrates, and control the geometry of the abradable coating to obtain large curved microscaffold networks with multilevel porosity. Microscaffold networks measuring up to ~ 9×10^4 mm^2 were fabricated at printing speeds of up to 250 mm/s, which is ~ 3 times faster than similar published work. A thick microscaffold of 50-

layers was studied and showed an average layer stacking alignment error of 57 µm. Non-planar multinozzle AM enabled the fabrication of curved microscaffold networks on a surface with radius as small as ~ 240 mm, with a toolpath error of 15 µm. The culmination of this work led to the creation of an aircraft component demonstrator using a non-planar multiprocess AM approach that features an actual curved functional abradable microscaffold network coating, with dimensions of ~ 520 mm × 78 mm × 5.6 mm and a radius of 962 mm, which was never realized before. The development of a large-scale non-planar multinozzle AM method and the various 3D-printed case studies shown in this research increase the potential for large-scale design of multifunctional parts for a wide variety of applications ranging from AM of concrete architectural structures, tissue engineering, microfluidic channels, and advancement of multiprocess AM.

TABLE OF CONTENTS

DEDICATION III

ACKNOWLEDGEMENTS IV

RÉSUMÉ V

ABSTRACT VII

TABLE OF CONTENTS IX

LIST OF TABLES XIV

LIST OF FIGURES XV

LIST OF SYMBOLS AND ABBREVIATIONS XXIV

CHAPTER 1 INTRODUCTION 1

1.1 Background 1

1.2 Dissertation structure 2

CHAPTER 2 LITERATURE REVIEW 4

2.1 Additive manufacturing 4

2.1.1 Fused Filament Fabrication 4

2.1.2 Direct Ink Writing 5

2.1.3 Multiprocess additive manufacturing 7

2.1.4 Toolpath generation 9

2.2 Industrial 6-axis robot arms 10

2.2.1 Basic concepts and motion principles 10

2.2.2 Non-planar additive manufacturing using 6-axis robots 12

2.3 Multinozzle printheads for additive manufacturing 14

2.3.1 Principle, advantages, and disadvantages 14

2.3.2 Current multinozzle additive manufacturing printhead technologies 15

2.4 Abradable seal coatings in aerospace industry 20

2.4.1 Types of abradable materials 20

2.4.2 Current application methods 21

2.4.3 Additive manufacturing of abradable acoustic coating for aircraft 22

2.5 Summary of literature review 24

CHAPTER 3 RESEARCH OBJECTIVES AND COHERENCE OF ARTICLES 25

3.1 Problem identification 25

3.2 Research objectives 25

3.3 Coherence of articles 26

CHAPTER 4 ARTICLE 1: HIGH-SPEED MULTINOZZLE ADDITIVE MANUFACTURING AND EXTRUSION MODELING OF LARGE-SCALE MICROSCAFFOLD NETWORKS 28

4.1 Introduction 29

4.2 Experimental methods 31

4.2.1 6-DOF robotic AM infrastructure 31

4.2.2 Material preparation 32

4.2.3 Design and multinozzle AM of microscaffold networks 33

4.2.4 Characterization of printed microscaffold networks 35

4.3 Multinozzle Extrusion Prediction Model (MEPM) 35

4.3.1 Model development 35

4.3.2 Model comparison with results from the literature 38

4.3.3 Multinozzle data acquisition and extrusion prediction 38

4.4 Results and discussion 39

4.4.1 Design exploration of multinozzle configurations 39

4.4.2 Prediction of single and multinozzle extrusions 42

4.4.3 Case studies: Multinozzle AM of periodic microscaffold networks 45

4.5 Conclusion 53

4.6 Supplementary information 55

CHAPTER 5 ARTICLE 2: NON-PLANAR MULTINOZZLE ADDITIVE MANUFACTURING OF THERMOSET COMPOSITE MICROSCAFFOLD NETWORKS ... 58

5.1 Introduction 58

5.2 Experimental methods 60

5.2.1 Material preparation 60

5.2.2 Material rheology 61

5.2.3 3D-printing of the sinusoidal substrate and tooling 62

5.2.4 Non-planar substrate topography acquisition and reference frame calibration 62

5.2.5 Non-planar multinozzle AM using 6-axis robot 64

5.2.6 Printhead tool center point calibration and toolpath recording 65

5.2.7 Characterization of printed non-planar microscaffold networks 66

5.3 Multinozzle Toolpath Generator (MTG) 66

5.3.1 Parametrization of the scanned non-planar surface mesh 66

5.3.2 Non-planar toolpath generation 67

5.3.3 Inverse kinematic problem solving 69

5.4 Results and discussion 69

5.4.1 Material properties 69

5.4.2 AM of non-planar microscaffold networks 72

5.5 Conclusion 80

5.6 Supplementary information 82

5.6.1 Supplementary videos 82

5.6.2 Effect of the relative distance between nozzles tip and the substrate top surface 83

CHAPTER 6 ARTICLE 3: NON-PLANAR MULTIPROCESS ADDITIVE MANUFACTURING OF MULTIFUNCTIONAL COMPOSITES 86

6.1 Introduction 87

6.2 Results and discussion 89

6.2.1 Non-planar multiprocess FFF of HTRP sandwich panel and DIW of thermosetting microscaffold network 89

6.2.2 Multifunctionalities of 3D-printed aircraft component demonstrator 94

6.3 Conclusion 101

6.4 Experimental methods 102

6.4.1 Heated enclosure for AM of high-temperature reinforced polymer (HTRP) 102

6.4.2 Slicing and 3D printing of non-planar HTRP sandwich panel 102

6.4.3 Characterization of sandwich panel 103

6.4.4 Sandwich panel assembly 103

6.4.5 Abradable material preparation 103

6.4.6 Material's viscosity measurements 104

6.4.7 Three interval thixotropy test (3iTT) 104

6.4.8 Non-planar multinozzle toolpath generation 105

6.4.9 Multinozzle AM of abradable thermosetting material 105

6.4.10 Characterization of thermosetting microscaffold network 106

6.4.11 Abradability test samples preparation 106

6.4.12 Abradability tests 106

6.4.13 Analysis of abraded samples 107

6.4.14 Differential scanning calorimetry (DSC) 107

6.4.15 Density measurements 108

6.5 Supporting Information 108

6.5.1 Comparison of commercial and modified 3D-printable abradable materials 109

CHAPTER 7 GENERAL DISCUSSION 112

CHAPTER 8 CONCLUSION AND RECOMMENDATIONS 116

8.1 Conclusion 116

8.2 Recommendations 117

BIBLIOGRAPHY 121

LIST OF TABLES

Table 2.1. Summary of select multinozzle AM printhead technologies 19

Table 2.2. Summary of abradable material types and their application process 22

Table 4.1. Comparison between theoretical and experimentally measured pore size for θ = 0°, 30°, 45°, 60° and 75.5°. 48

Table 4.2. Experimental volumetric flow rate calculation for printing speed v = 50, 100, 150, 200 and 250 mm/s. 57

Table 6.1. Density of benchmark and parts of the aircraft component demonstrator. 95

Table 6.2. GM and FS loadings of abradable materials with the measured cured density. 109

LIST OF FIGURES

Figure 2.1. a) Schematic of the FFF process. A thermoplastic filament is melted and extruded by a heated nozzle using a gear mechanism. Adapted from [24]. b) Schematic of the DIW process. The ink is extruded under pressure at room temperature using a pneumatic pressure, a piston, or an endless screw. Adapted from [25]. 5

Figure 2.2. Characterization of the process-related apparent viscosity η_{app}. a) Extrusion of a shear-thinning ink and flow profile inside the nozzle: ηapp is dependant on the nozzle internal geometry, flow rate and applied pressure. Adapted from [40]. b) Example of a plot of viscosity as a function of the shear rate and apparent viscosity as a function of apparent shear rate for four shear-thinning materials. Both viscosity types are fitted with a power law model. Adapted from [11]. 7

Figure 2.3. a) Multiprocess AM combining DIW and FFF. b) Flexible piezoelectric energy harvester under bending deformation. Adapted from [47]. c) Schematic of multi-material 3D printing process using FFF. d) Multi-material piezoelectric nanocomposite shoe sole. e) Human stomp test generating a voltage of ~ 20 V. Adapted from [43]. 8

Figure 2.4. a) Typical AM toolpath generation (i.e., slicing) workflow. Adapted from [56]. b) Comparison between planar and non-planar slicing. Stair stepping effect resulting from planar slicing and smooth surface counterpart resulting from non-planar slicing. Adapted from [56]. c) Non-planar AM using 3-axis and nozzle collision. d) Non-planar AM using more than 3-axis (with nozzle orientation). Adapted from [57]. 10

Figure 2.5. a) Schematic of a 6-axis robot arm. Each actuator is connected by a pivot link. b) Reference frames involved in the motion of an industrial robot arm. Adapted from [77]..... 11

Figure 2.6. Approximated linear tool movement by several continuous robot motion (CNT) at 0 (FINE), 50, 70 and 100%. Adapted from [77]. 12

Figure 2.7. Non-planar AM research work using 6-axis robot arm. a) Cylindrical projection method. Adapted from [65]. b) Multi-resolution non-planar AM. Adapted from [94]..... 13

Figure 2.8. Early concepts of multinozzle AM printhead devices. a) Multi-material DIW of hydrogel tissue using four individual nozzles. Adapted from [114]. b) Microvascular

multinozzle array fabricated using PMMA, composed of 64 square-shaped nozzles. Adapted from [13]. c) Fabricated microscaffold made of microcrystalline wax. Adapted from [13]..15

Figure 2.9. Multi-material multinozzle 3D printing device. a) Pneumatic solenoids concept for seamless switching of multi-material at high-frequency. b) Fabrication of 3D voxelated pattern using a multinozzle printhead composed of 16 nozzles in a 4 × 4 arrangement. c) 3D printing of a soft robot made of flexible (blue) and stiff (grey) silicone inks. Adapted from [101]. 16

Figure 2.10. FFF technique using more than one extrusion nozzle. a) Three-nozzle system for multi-resolution FFF on 6-axis robot. Adapted from [102]. b) E3D Kraken printhead for extrusion of up to four thermoplastic filaments. Adapted from [117]. c) Printhead rotation around the *Z* axis to simultaneously extrude four side-by-side filaments. d) Multinozzle 3D printing of a polygon shape using four different thermoplastic filaments. Adapted from [119]. 17

Figure 2.11. Multi-material multinozzle adaptive 3D printing of soft materials at 5 mm/s. a) 4 s into printing. b) 8 s into printing. The nozzles height varies with the substrate topography. c) Resulting 10 conformal layers. Adapted from [120].....18

Figure 2.12. a) Schematic of the abrasion of an abradable layer (red). Due to the rotation of the fan, the blade is elongated from its nominal path to remove a layer of abradable material. Adapted from [131]. b) Types of abradable materials (1-5) according to their operating temperature (0 – 1500 °C). Adapted from [132]. 20

Figure 2.13. a) Fabrication of a microscaffold sample in the shape of a disc. The filaments are printed using a 250 µm conical nozzle using a pneumatic dispensing system at 2.8 MPa. b) Internal microscaffold structure composed of orthogonal filaments. c) Impedance tube for acoustic absorption characterization. d) Acoustic absorption coefficient of the three promising abradable material blends compared with the JCAL simulation. Adapted from [11].....23

Figure 4.1. 6-DOF robotic AM infrastructure. a) The material contained in the 50 cm³ reservoir is pushed by a piston at required pressure through an array of 26 cylindrical nozzles (D = 250 µm, L = 6.5 mm). The piston's course is monitored via a position sensor, which allows accurate pressure setting in order to keep the extrusion flow rate constant. The tool center

point (TCP) is located at the center of the nozzle array. b) Close-up view of the multinozzle printhead showing the vertical extrusion of the material through the nozzle array. 32

Figure 4.2. Isometric view of a typical partitioned microscaffold network ($i \times j$ configuration, N number of layers). Detail A: view of a partition wall made by an offset toolpath. Detail B: top view of the pore size p = 750 µm (in blue). Detail C: side view of the filaments center-to-center spacing s = 1 mm and nominal filament diameter d = 250 µm. Detail D: Cross-sectional view of the filaments stacking in a wall (in red). 34

Figure 4.3. Multinozzle extrusion prediction modeling charts for organic ink. The current infrastructure parameters are shown in red. a) Applied pressure prediction for four multinozzle configurations with different nozzles inner diameter (α = 26, D = [100, 250, 500, 750] µm, L = 6.5 mm). The maximum extrusion pressure (65 MPa) is not reached with the use of organic ink (red dotted line). b) Total volumetric flow rate prediction for four multinozzle configurations with different nozzles inner diameter (α = 26, D = [100, 250, 500, 750] µm, L = 6.5 mm). The maximum reachable printing speed for the configuration used in this work (D = 250 µm) is 250 mm/s due to the printhead maximum piston displacement speed. c) Total volumetric flow rate prediction for five multinozzle configurations with different number of nozzles (α = [1, 4, 10, 26, 50], D = 250 µm, L = 6.5 mm). The 6-axis robot maximum tool movement speed limits the printing speed at 2000 mm/s. 41

Figure 4.4. a) Comparison of the MEPM and experimental values from the literature for single cylindrical nozzle extrusion (α = 1, D = 510 µm, L = 18.87 mm) of organic ink (60/40 wt.%) [40] and single cylindrical nozzle extrusion (α = 1, D = 200 µm, L = 12.24 mm) of dissolved Polylactic Acid (PLA, 20 wt.%) for solvent-cast 3D printing [26]. b) Applied pressure prediction and experimental results for multinozzle (cylindrical, α = 26, D = 250 µm, L = 6.5 mm) extrusion of organic ink at v = 50, 100, 150, 200 and 250 mm/s. Error bars represent the 95 % confidence interval. c) Total volumetric flow rate prediction and experimental results from the experiments in b). 43

Figure 4.5. 5-layer microscaffold network (9 × 15 configuration) printed at 250 mm/s (~ 1 min 36 s) for a total of 234 × 390 filaments wide. a) Top view of the entire print. b) Close-up top view of the microscaffold network. c) ×25 magnification image of the microscaffold filament

stacking showing the average filaments diameter d = 255 µm and average pore size p = 736 µm. d) Close-up view of the transition between two columns displaying a toolpath rounding, which reduces the microscaffold network size by 10 mm. Focus on details of print defects A, B, C and D. e-f) Close-up views of the spacing between printed columns (Details C, D). ...46

Figure 4.6. 2-layer microscaffold network (3 × 5 configuration) printed at 50 mm/s (~ 30 s) with variable pore size on the second layer. a) General view of the entire print. The nozzles orientation θ is given with respect to the X axis, which is perpendicular to the printing direction (Y axis). The first layer is printed at θ = 0°. The multinozzle is then rotated around its Z axis to increase θ (from 0° to 30°, 45°, 60° and 75.5°) for each column on the second layer. b) ×25 magnification images of the microscaffold filament stacking at θ = 30° (d = 259 µm, p = 606 µm), θ = 45° (d = 263 µm, p = 436 µm), θ = 60° (d = 267 µm, p = 233 µm) and θ = 75.5° (d = 250 µm, p = 0 µm). 49

Figure 4.7. 5-layer partitioned microscaffold network (9 × 15 configuration) printed at 50 mm/s (~ 8 min 45 s) for a total of 234 × 390 filaments wide and 135 microscaffold partitions. a) Top view of the entire print. b) Close-up top view of a partitioned microscaffold. Each microscaffold is a square of 26 mm wide surrounded by walls, made by the offset toolpath. c) ×25 magnification image of a wall. The toolpath offset leads to the robot slowing down, thus leading to over-extrusion and the printing of larger filaments (w = 847 µm). 50

Figure 4.8. 50-layer partitioned microscaffold network (3 × 3 configuration) printed at 50 mm/s (~ 8 min 45s) for a total of 78 × 78 filaments wide and 9 microscaffolds. a) General view of the entire print. Sections A-A, B-B and C-C were observed using an X-ray micro computer tomography scanner. b) Cross-sectional image of the network showing a printed microscaffold between two partition walls (A-A). c) Cross-sectional images of filaments position across layers for a width of 7 in-plane filaments near the microscaffold center (B-B) where s = 1006 µm (with σ = 57 µm), and near one of the wall (C-C) where s = 1008 µm (with σ = 150 µm). $s1$ = 614 µm is the minimum horizontal spacing between filaments and $s2$ = 1449 µm is the maximum. Vertical spacing $z1$ = 294 µm < $z2$ = 422 µm shows the slight collapsing of the microscaffold. Images c) and d) were digitally post-processed to hide the background and improve clarity of the desired features. 52

Figure 4.9. Measured pressure inside the multinozzle printhead for the extrusion of organic ink at 50 mm/s printing speed and the measured pressure for the empty reservoir at 50 mm/s printing speed (dry run), with respect to the same piston displacement. During the extrusion phase, the spring is compressed and applies a force on the cross-section area of the piston when the piston moves forward, constantly increasing the pressure in the hydraulic oil. The linear fit slopes exhibit the linear behavior of the spring, according to Hooke's law. The difference between the curves is mainly composed of the pressure gradient during material extrusion. Data was cleaned with a Gaussian filter (with standard deviation σ = 78 kPa). 55

Figure 4.10. MEPM computation for individual nozzle volumetric flow rates using the organic ink at v = 50 and 250 mm/s for each nozzle of the multinozzle printhead. The resulting recalculated individual flow rates (Iterative process, solid line) diverge from to the first flow rate estimates (Equation (4.1), dashed line). The divergence is more significant at 250 mm/s (high printing speed) than at 50 mm/s (moderate printing speed). 56

Figure 4.11. Viscosity as a function of the apparent shear rate calculation using the MEPM and experimental measurements for extrusion of organic ink (60/40 wt.%) using the multinozzle printhead (α = 26, D = 250 µm, L = 6.5 mm). Results reported in [40] for single nozzle geometry (α = 1, D = 510 µm, L = 18.87 mm) were superimposed for comparison.....56

Figure 5.1. Non-planar substate topography acquisition and reference frame calibration method. a) 3D scanning of the substate, including the calibration pyramids (mesh origin is arbitrarily generated). b) Creation of the mesh reference frame by aligning the mesh origin with the pyramids tip included in the scanned mesh. c) Creation of the experimental reference frame using the calibration tip. 63

Figure 5.2. Non-planar microscaffold networks manufacturing workflow (using the single curvature sinusoidal surface as example). a) Non-planar microscaffold networks generation using the developed MTG. b) Non-planar multinozzle additive manufacturing using 6-axis robot. c) Close-up 1: detailed view of the 3D printing of a non-planar microscaffold network. d) Close-up 2: detailed view of the multinozzle extrusion through the 1D multinozzle array. 65

Figure 5.3. Schematics of the two main MTG process steps where the non-planar sinusoidal surface is used as an example. a) NURBS surface parametrization on the calibrated scanned mesh of non-planar surface. b) Non-planar toolpath generation by projection of the planar toolpath on the NURBS surface. 68

Figure 5.4. Epoxy formulation rheological properties. a) Shear-thinning fluid behavior of viscosity (obtained by rotational rheology) and process-related apparent viscosity (obtained by capillary rheology). b) Time-dependency of complex viscosity over 45 min obtained by oscillatory time sweeps. c) Shear storage and shear loss moduli time-dependency of the epoxy formulation within four time periods tested after mixing via 3iTT. 71

Figure 5.5. Visualization module of the MTG process for the single curvature sinusoidal surface. a) Generated sinusoidal non-planar toolpath and orientation matrices. b) Collision detection between multinozzle footprint for the first two layers and the NURBS surface. c) Prediction of the non-planar microscaffold network printed geometry. Uneven spacings are created by distortion of the toolpath following the projection.....74

Figure 5.6. Non-planar AM of a microscaffold network on a sinusoidal surface (theoretical radius of both convex and concave region $r$theo = 240 mm). a) Microscaffold network dimensions: ~ 130 mm × 130 mm × 4.25 mm (130 filaments in both X and Y directions, and 20 layers). Filaments average diameter d = 254 µm (σ = 14 µm, MRE = 1.5%) and pore size p = 754 µm (σ = 25 µm, MRE = 0.5%). Average first layer radii of the print: r convex = 242 mm (σ = 7 mm, MRE = 1.0%) and r concave = 228 mm (σ = 9 mm, MRE = 5.0%). Average layer spacing z = 390 µm (σ = 13 µm, MRE = 2.4%). b) Cross-section A – A: side view of the layer stacking showing uneven spacings between each printing pass, due to distortion of the toolpath. Wider spacings (#1 & #2) dimension increases, and narrower spacings (#3 & #4) dimension decreases as the number of layers increase. Cross-section A – A view, the side view inset, and uneven spacing close-up views were digitally post-processed to hide the background and improve clarity of the desired features. 75

Figure 5.7. Non-planar AM of a large-scale microscaffold network on an aircraft casing. a) MTG result of the projected toolpath on the double curved surface of the casing. b) Microscaffold network dimensions: ~ 402 mm × 130 mm × 4.25 mm (390 × 130 filaments, and 20 layers).

Filaments average diameter d = 246 µm (σ = 14 µm), pore size p = 755 µm (σ = 40 µm) and layer spacing z = 392 µm (σ = 17 µm). The side view inset was digitally post-processed to hide the background and improve clarity of the desired features. c) Cloud-to-mesh comparison for the computation of the absolute euclidean distance between recorded and programmed toolpaths. Saturation is set at 20 µm to be consistent with the robot's repeatability and reaches a maximum distance of 148 µm in layer changes. The microscaffold network is composed of ~ 95% of the 17,196 recorded points (~ 5% material loss), whose error is below the saturation threshold. 80

Figure 5.8. Effect of relative distance between nozzles tip and the substrate top surface. a) Design of experiment for convex and concave surfaces: the printhead linearly travels from P_1 to P_2 at 50 mm/s. b) Mathematical relationships governing the surfaces: linear increase of h with L. c) Top and close-up views of deposition results for convex and concave surfaces. 85

Figure 6.1. Non-planar multiprocess FFF of an HTRP sandwich panel and multinozzle DIW of a thermosetting microscaffold network. a) (1) FFF of curved HTRP sandwich panel using custom heated enclosure and 6-axis robot arm (the enclosure is shown with an open cross-section to see the interior), (2) HTRP sandwich panel assembly on the aircraft casing, 3D scanning of the top surface topography and multinozzle toolpath generation, (3) non-planar multinozzle AM of abradable thermosetting microscaffold networks on top of HTRP panel assembly. b) Close-up view on FFF process and characteristics of a printed HTRP sandwich panel section, whose total thickness varies from 30 to 33.8 mm. c) Euclidean distance analysis from the comparison between CAD and scan mesh of a panel section. Max error on top surface is 0.28 mm. d) Abradable material (0GM12FS formulation) shear-thinning behavior of viscosity η (obtained by rotational rheology) and process-related apparent viscosity η_{app} (obtained by capillary rheology). e) Shear storage G' and shear loss moduli G'' time-dependency of the abradable material (0GM12FS formulation) obtained from three interval thixotropy test (3iTT). f) Close-up view of multinozzle DIW process and characteristics of the printed microscaffold network, whose thickness is 5.6 mm. g) Side view on the bottom porosity level, whose thickness $z$tot is 2.83 mm and pore size p is 726 µm. h) Side view on the top porosity level, whose $z$tot is 2.74 mm and p is 183 µm. i) Top view on the last printed layer, where d = 256 µm and p = 176 µm. j) Overall view of the aircraft component

demonstrator. Largest radius r ~ 996 mm, dimensions of the thermosetting microscaffold network is ~ 520 mm × 78 mm. Overall filament diameter d = 257 µm and layer stacking distance z = 397 µm. 93

Figure 6.2. Abradability test setup and blade trace results. a) Schematic of a 3D-printed abradable sample made of the 0GM12FS formulation using a single nozzle (~ 45 mm × 45 mm × 6 mm). b) Schematic of the abradability test rig. Three titanium blades are mounted on a rotating spindle while the abradable sample is mounted on a 3-axis stage. A thermal camera is used to record the temperature profile of the 3D-printed sample throughout the process. Once the spindle reaches the rotating speed of 15,000 rpm, the stage is moved toward the spindle at the linear speed of 0.15 mm s^{-1} and penetration depth of 1 mm. c) Microscopic top view of an abraded benchmark sample showing a blade trace of ~ 8.6 mm wide and ~ 35.1 mm long. d) Microscopic top view of an abraded 0GM12FS formulation sample. The blade trace shows that some pore sizes are reduced after abrasion (orange region) while some pores appear blocked (red regions). e) Side view from the thermal camera during the abradability test. The sample reached a temperature T = 160 °C at the location of the blade trace during abrasion. 97

Figure 6.3. Analysis of abradability results between 3D-printed samples made of 0GM12FS formulation ≡ and molded samples made of benchmark material ■. a) Measured percentage of open area (POA) of 3D-printed sample on the last layer before the test and on the top remaining layers after the test. The theoretical POA of the printed sample is 18 %. Error bars represent standard deviation (σ = 1 % and 2 %, respectively). b) Comparison of measured maximum blade penetration depth after test for benchmark and 3D-printed samples. Percentages are given with respect to the 1 mm setpoint. Error bars represent standard deviation (σ = 5 % and 4 %, respectively). c) Comparison of measured worst case blade length after test for benchmark and 0GM12FS formulation samples. Negative values represent a blade wear and positive values represent material accumulation on the blade. 100

Figure 6.4. a) Sandwich panel assembly. The panels were glued together side-by-side using the epoxy resin Epon 862 and Epikure 3274 curing agent, and installed on the aircraft casing using double-sided tape. b) Masking tape was installed on the side of the panel to protect it from

material losses during the multinozzle AM process. The 3D scanner was used to obtain a mesh representation of the top surface of the panel. c) Multinozzle Toolpath Generator (MTG): the scanned surface of the sandwich panel was used to generate a NURBS surface composed of 50 × 11 control points (in the *u* and *v* directions, respectively), and second degree interpolation splines. The MTG generated a non-planar multinozzle AM toolpath on top of the NURBS surface and corrected some nozzle array collisions with the substrate (that appear to be located at the bonding joints of the panels, probably due to misalignment during assembly). Rotation matrices were calculated for all positions of the toolpath and sent to simulation software RoboDK to solve the inverse kinematic problem that allows the 6-axis robot to manufacture the printed geometry predicted by the MTG. The programmed microscaffold geometry consists of filaments diameter d = 250 µm, same orientation layer height of z = 400 µm, bottom porosity level pore size p = 750 µm, and top porosity level pore size p = 184 µm. 110

Figure 7.1. Summary of required applied extrusion pressure ΔP as a function of the printing speed v for organic ink, Epon 828 formulation and 0GM12FS abradable formulation. Maximum pressure limits are 65 MPa (for 50 cm³ reservoir) and 20 MPa (for 250 cm³ reservoir). 113

LIST OF SYMBOLS AND ABBREVIATIONS

0GM12FS	Composition of 0 wt% glass microspheres (GM) and 12 wt% fumed silica (FS)
2D	Two-dimensional
3D	Three-dimensional
3iTT	Three interval thixotropy test
AM	Additive manufacturing
CAD	Computer-assisted drawing
CT	Computer tomography
DIW	Direct ink writing
DOF	Degrees of freedom
DSC	Differential scanning calorimetry
FA	Fabrication additive
FACMO	Fabrication additive des composites à matrice organique
FFF	Fused filament fabrication
FS	Fumed silica
GM	Glass microsphere
HTRP	High-temperature reinforced polymer
I/O	Input/output
LM^2	Laboratory for multiscale mechanics
LVER	Linear viscoelastic region
MAE	Mean absolute error
MEPM	Multinozzle extrusion prediction model
MRE	Mean relative error
MTG	Multinozzle toolpath generator

NURBS	Non-uniform rational b-spline
PEEK	Polyether ether ketone
PEI	Polyetherimide
PLA	Polylactic acid
POA	Percentage of open area
SLA	Stereolithography
TCP	Tool center point
TPP	Teach pendant programming
A_{avg}	Average nozzle area
$\boldsymbol{B}$	Orthogonal basis matrix
d	Filament diameter
$\bar{d}$	Measured average filament diameter
D	Theoretical nozzle inner diameter
D_{avg}	Average nozzle diameter
D_i	Individual nozzle inner diameter
f	Parametric function that generates the NURBS surface
G'	Shear storage modulus
G''	Shear loss modulus
h	Filament deposition distance from surface
i	Number of rows (printing passages along X) of a microscaffold network
j	Number of columns (printing passages along Y) of a microscaffold network
K	Flow consistency index
L	Nozzles length
n	Power-law index (also known as material flow behavior index)

$\vec{\boldsymbol{n}}$	Surface normal at evaluated point on the NURBS, aligned with printhead axis
n_x	Number of control points on the NURBS in the *X* direction
n_y	Number of control points on the NURBS in the *Y* direction
N	Number of layers
p	Pore size (distance between two filaments from the top view)
$\bar{p}$	Measured average pore size
Q_i	Average volumetric flow rate of each nozzle
$Q_{i,guess}$	Flow rate guess for the iterative calculation of Q_{tot}
$Q_{i,new}$	New calculated flow rate guess
Q_{tot}	Total volumetric flow rate of all nozzles
r	Curved surface radius
r_{min}	Curved surface radius (minimum)
$\boldsymbol{R}$	Rotation matrix
R_{eq}	Total equivalent flow resistance for all nozzles
R_i	Individual nozzle flow resistance
s	Center-to-center distance between nozzles
S	NURBS surface
t	Time after material mixing
$\vec{\boldsymbol{t_u}}, \vec{\boldsymbol{t_v}}$	Surface tangents at evaluated point on the NURBS
T	Temperature
T_g	Glass transition temperature
u, v	NURBS surface parameter
v	Printing speed
w	Over extruded filament width

x, y, z	Cartesian coordinates with respect to a given reference frame
x', y', z'	Cartesian coordinates of an evaluated point on a NURBS surface
X, Y, Z	Reference frame axes
z	Vertical stacking distance for layers in the same orientation
$\bar{z}$	Measured average vertical stacking distance for layers in the same orientation
$\bar{z}_{\mathrm{tot}}$	Measured average porosity level thickness
α	Number of nozzles of a multinozzle printhead
γ	Shear strain
$\dot{\gamma}$	Shear rate
$\dot{\gamma}_{\mathrm{i}}$	Wall shear rate of each nozzle
$\dot{\gamma}_{\mathrm{w}}$	Process-related apparent wall shear rate
ΔP	Required pressure gradient inside nozzles for material extrusion
ΔQ_{i}	Absolute relative error of flow rate calculation
Δz	Maximum relative distance between the TCP and the top of a non-planar surface
η	Viscosity
η_{app}	Process-related apparent viscosity
η_{i}	Dynamic process-related apparent viscosity for each nozzle
η^*	Complex viscosity
θ	Multinozzle angle of rotation around its axis
σ	Standard deviation
ω	Angular frequency

CHAPTER 1 INTRODUCTION

1.1 Background

Over the past few decades, the automotive and aerospace manufacturing industries have widely integrated additive manufacturing (AM) techniques to reduce costs and produce lighter, more complex parts [1]. In particular, the aerospace industry has been one of the key adopters of AM, with metal AM being popular for manufacturing some functional parts [2]. One of the most popular success stories of AM in aerospace is probably General Electric's LEAP engine fuel nozzle, which was manufactured by direct metal laser melting in 2012, reducing the previously welded assembly of twenty parts to a single one [3]. Recent advances in AM have led to a growing interest in AM of polymer composites, which exhibit attractive mechanical properties and high dimensional stability [4], [5]. AM of thermoplastic polymers has gained popularity through the Fused Filament Fabrication (FFF) technique, in which materials must be heated above their melting temperature to allow extrusion and layer-by-layer deposition on a heated platform. Another extrusion method, Direct Ink Writing (DIW) allows the extrusion at room temperature of a variety of viscoelastic materials such as hydrogels, inks, and also thermosetting polymers. A popular geometry fabricated by DIW is the woodpile lattice structure, also referred as a microscaffold [6], [7]. These micro-scale, three-dimensional periodic filaments stacking mostly have applications in tissue engineering but also as acoustic absorption patterns, which could be used to create functional sound-absorbing components for aircraft [8].

One of the key aircraft component is the abradable seal coating, which consists of a layer of sacrificial material deposited inside gas turbine engines to allow minimal clearances between the tips of the rotor blades and the surrounding casing. Abradable coatings are essential to ensure engine efficiency by reducing specific fuel consumption of aircraft. Used in many parts of the engine, some abradable coatings for low-temperature areas (i.e., the upstream region of the engine) are made of thermosetting polymer materials [9]. The DIW of such coatings has been explored by fabricating planar abradable thermosetting porous microscaffolds that feature sound absorption functionality [10], [11]. However, the AM scalability and feasibility of an actual full-size coating which conforms to the interior curvature of an engine is still unknown. The fabrication of large-scale thermosetting parts with high-resolution features is often impeded by extremely long printing

times, which can be further limited by the resins used due to their viscosity, curing time, working time and gelation time. A good solution to scale up the DIW of thermosetting porous microscaffolds under a relatively low printing time could be to use a multinozzle printhead. Those devices are generally composed of more than one nozzles to enable the simultaneous extrusion of filaments and have shown significant potential for enabling the rapid AM of viscoelastic inks such as thermosetting composites [12], [13]. Yet, the multinozzle DIW of large, curved parts has never been demonstrated. To overcome the geometrical constraints of commercial 3D printers and unlock the potential for large-scale non-planar parts, industrial 6-axis robot arms, typically used in manufacturing processes to automate tasks such as welding, painting, and assembly, have been progressively employed with AM technologies [14].

The doctoral research project presented in this dissertation is part of the FACMO Chair, an industrial research and development partnership between Safran S.A. (France) and the Laboratory for Multiscale Mechanics (LM²) at Polytechnique Montreal. The FACMO Chair is composed of several general objectives, ranging from materials composition, to advanced 3D printing, to mechanical characterization and simulation, which are undertaken by other doctoral students, master's students and post-doctoral fellows. The main objective of the chair is to develop the next generation of advanced manufacturing approaches and mathematical models for the creation of high performance composite structures for the aerospace industry. The current project focuses on investigating the potential of AM for manufacturing large thermosetting-based abradable seal coatings with microscaffold geometry inspired by sound absorption patterns. The project aims to demonstrate the AM of large high-resolution multifunctional aircraft components, focusing on the use of a 6-axis robotic arm equipped with a multinozzle printhead to enable large-scale non-planar AM with full printing orientation freedom while reducing printing time.

1.2 Dissertation structure

This dissertation includes eight chapters. Chapter 2 presents a literature review on additive manufacturing, industrial 6-axis robot arms used for additive manufacturing, multinozzle printheads for additive manufacturing and the state of the art of abradable seal coatings used by the aerospace industry. Chapter 3 provides information regarding the research objectives and the coherence of articles. The main results of this dissertation are given in the form of three articles

published or submitted to peer-reviewed scientific journals in chapters 4 to 6. Chapter 4 demonstrates the high-speed additive manufacturing of high-resolution, large-scale microscaffolds using a custom multinozzle printhead. Chapter 5 presents the development of a non-planar multinozzle AM method and its applicability by fabricating non-planar thermosetting-based microscaffolds on surfaces featuring complex curvature. Chapter 6 illustrates a large-scale multiprocess approach to rapidly fabricate a large non-planar multifunctional aircraft component demonstrator composed of an abradable coating printed as a thermosetting microscaffold. Chapter 7 provides a general discussion of the research while Chapter 8 concludes with a summary of the research and gives recommendations for future work.

CHAPTER 2 LITERATURE REVIEW

The literature review is composed of four main themes introducing some aspects of additive manufacturing, industrial 6-axis robot arms, multinozzle printhead devices (and their use for additive manufacturing) and the state of the art of abradable coatings used in the aerospace industry.

2.1 Additive manufacturing

Additive manufacturing (AM), also known as three-dimensional (3D) printing, is a group of manufacturing methods for fabricating objects and parts based on the principle of superimposing layers of material following the slicing of a computer-assisted drawing (CAD) model. These manufacturing methods have been expanding since the early 1980s [15] and were accounting for more than 12% of their applications in the aerospace sector in 2017 [16]. In 2022, the AM market is valued at more than USD 15 billion and is expected to grow by 24 % until 2027 [17].

Unlike more conventional manufacturing methods where the part geometry is obtained by removing material (*i.e.*, subtractive manufacturing), AM enables the addition of material at the desired location to obtain the final part geometry. AM offers several benefits such as accessibility, mass optimization, reduced material waste, great design freedom, and a wide variety of available materials [18]. However, AM also includes drawback, such as anisotropic material properties as a result of layer-by-layer manufacturing, making the produced parts less mechanically efficient when compared to subtractive manufacturing methods [19]. Also, AM can be a relatively slow process, with printing times occasionally ranging over several hours up to days depending on the size and resolution of the printed part [20], [21]. Encompassing several techniques which depend on the type of physical phenomenon involved in the process, AM includes a material extrusion category, which addresses the selective dispense of feedstock material on a printing substrate through a dispensing nozzle [22]. The material extrusion category involves, among others, the Fused Filament Fabrication (FFF) and the Direct Ink Writing (DIW) techniques.

2.1.1 Fused Filament Fabrication

The FFF technique is one of the most popular and accessible AM techniques. Figure 2.1a shows a schematic of how FFF usually works. The feedstock is first prepared in the form of a thermoplastic polymer or composite filament spool. The filament is fed into a printhead by a gear mechanism,

until it reaches a heated nozzle. The thermoplastic filament is then melted at a temperature above its melting temperature, after which it is extruded through the nozzle and deposited on a hot printing bed. As the fused material exits the nozzle, the deposited filament rapidly cools down below its glass transition temperature and returns to a solid state. The printhead is typically mounted on rails that allow movement in the *X* and *Y* axes for filament deposition. The orderly addition of multiple filaments forms a layer of the printed part. When a layer is complete, the printing bed is lowered along the *Z* axis to move the printhead to the next layer, until the geometry of the final part is achieved [23].

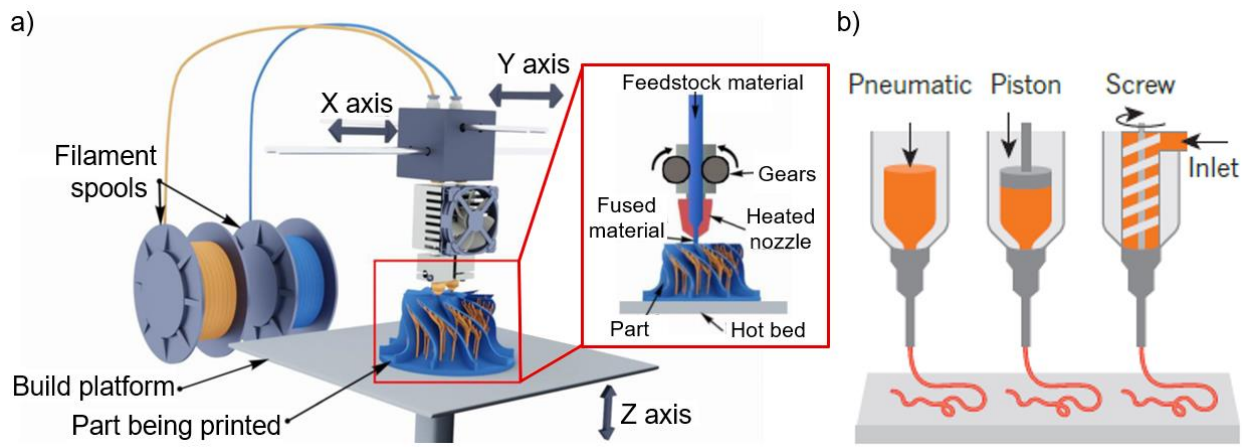

Figure 2.1. a) Schematic of the FFF process. A thermoplastic filament is melted and extruded by a heated nozzle using a gear mechanism. Adapted from [24]. b) Schematic of the DIW process. The ink is extruded under pressure at room temperature using a pneumatic pressure, a piston, or an endless screw. Adapted from [25].

2.1.2 Direct Ink Writing

The DIW technique relies on the principle of continuous extrusion of an ink through a dispensing nozzle. The ink used can be, for instance, in the form of a soft paste-like material [25], a dissolved thermoplastic [26] or an uncured thermosetting polymer [27]. Figure 2.1b shows the extrusion of an ink by DIW. The ink is pressurized in a finite volume reservoir (or syringe) using either a pneumatic system, a piston or an endless screw that is continuously fed by an inlet. As opposed to FFF, the ink is usually extruded at room temperature and the volumetric flow rate is generally lower [28]–[30]. Depending on the inner diameter, length, shape (*i.e.*, cylindrical or conical) of the nozzle used, the ink viscosity, and the pressure system used, the volumetric flow rates in DIW

usually result in a printing speed varying between 5 – 88 mm/s [29], [31]–[37]. Such relatively low printing speeds usually impede large-scale AM of thermosetting polymers using DIW as the printing time may exceed the working time or gel time of the material. It is possible to use conical nozzles (allows greater extrusion pressure to achieve higher printing speeds compared to cylindrical ones) and shear-thinning materials, to increase the printing speed of DIW at up to 175 mm/s [11].

Shear-thinning inks are viscous materials that tend to decrease their viscosity when they are subjected to high shear strain [38]. When printing a shear-thinning ink, the material is extruded by applying a shear strain γ inside the nozzle. As the shear rate $\dot{\gamma}$ increases, the viscosity η of the shear-thinning ink decreases, allowing the material to be extruded in the geometry of the desired shape [25], [38]. The viscosity η of the material as a function of the shear rate can be measured using a rheometer [38], [39]. Depending on the ink used, DIW extrusion can involve high shear rates, exceeding $\dot{\gamma} > 10^2$ s^{-1} [40] (including conical and cylindrical nozzles) which could make it difficult to characterize the viscosity using certain rheometers (using a rheometer with cone-and-plate or concentric disk geometry, for instance) [39]. To overcome this limitation, a method to characterize the process-related apparent viscosity η_{app} as a function of the process-related apparent shear rate $\dot{\gamma}_{\mathrm{w}}$ was developed by Bruneaux et al. [40], based on capillary rheology (Figure 2.2a). The method involves estimating the material's viscosity inside the nozzle as a function of the constant applied pressure, resulting volumetric flow rate, and internal geometry of the nozzle by using Hagen-Poiseuille equations and assuming laminar flow of the fluid in the nozzle. By combining both η and η_{app} measurements, the viscosity profile of most shear-thinning polymers can be described by fitting a simple power law model (Figure 2.2b), such that:

$$\eta = K\dot{\gamma}^{n-1} \text{ [38]} \tag{2.1}$$

where K is the flow consistency index (Pa·s^n), and n is the power law index (dimensionless). The material viscosity behavior is shear-thinning when $n < 1$, and shear-thickening when $n > 1$. The characterization of viscosity is essential for polymer processing because the viscosity can be used to predict the required pressure for material extrusion through a given nozzle or the injection pressure for parts manufactured by injection molding.

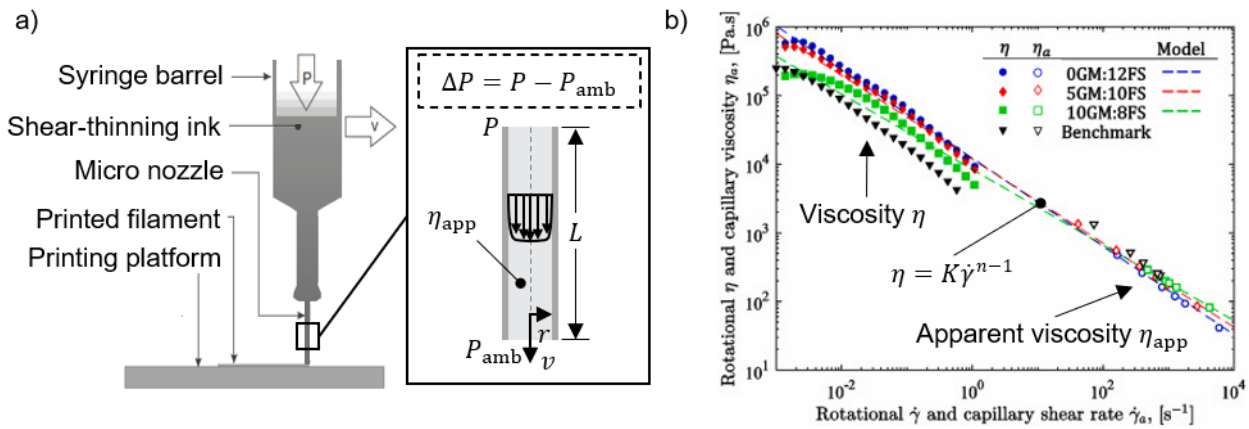

Figure 2.2. Characterization of the process-related apparent viscosity η_{app}. a) Extrusion of a shear-thinning ink and flow profile inside the nozzle: η_{app} is dependant on the nozzle internal geometry, flow rate and applied pressure. Adapted from [40]. b) Example of a plot of viscosity as a function of the shear rate and apparent viscosity as a function of apparent shear rate for four shear-thinning materials. Both viscosity types are fitted with a power law model. Adapted from [11].

2.1.3 Multiprocess additive manufacturing

The functionality of a 3D-printed part is "derived from the combination of the object's geometry and properties" [22]. By using specific materials, for instance, 3D-printed parts can involve electrical or thermal conductivity, integrated sensors, mechanical reinforcement or multi-material combination [18], [41]–[45]. Multiprocess AM is the combination of AM techniques that allows the fabrication of multifunctional parts [46]. Rafiee et al. [47] demonstrated the multiprocess AM of flexible piezoelectric devices for energy harvesting, by combining the FFF of polylactide acid (PLA) with the DIW of conductive inks and piezoelectric material. Two DIW dispensers and one FFF printhead were mounted on a 3-axis gantry motion system (Figure 2.3a) and were utilized in sequence to create a small flexible energy harvester that could generate a voltage after being submitted to a vibration load (Figure 2.3b). Similarly, Tao et al. reported a multiprocess AM method involving two FFF printhead in which a piezoelectric and a conductive filament were printed alternately to manufacture a 3D multi-material voltage-generator structure [43] (Figure 2.3c). The authors successfully fabricated a shoe sole (Figure 2.3d) from which a human stomp test yielded a measured voltage of ~ 20 V (Figure 2.3e).

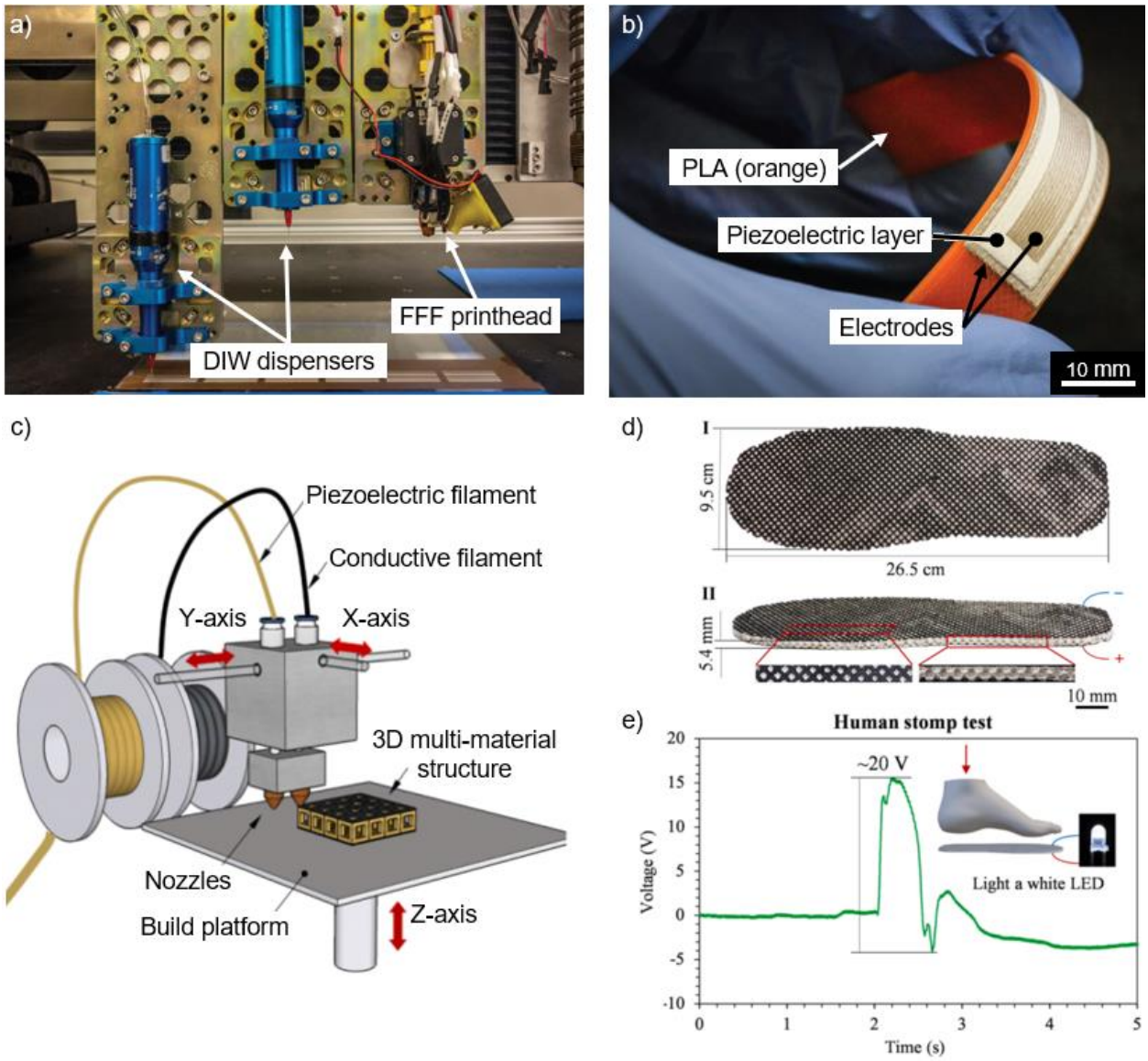

Figure 2.3. a) Multiprocess AM combining DIW and FFF. b) Flexible piezoelectric energy harvester under bending deformation. Adapted from [47]. c) Schematic of multi-material 3D printing process using FFF. d) Multi-material piezoelectric nanocomposite shoe sole. e) Human stomp test generating a voltage of ~ 20 V. Adapted from [43].

Other authors reported multiprocess AM involving the use of DIW and FFF for the fabrication of tactile sensors for soft robotics [48]. Yet, FFF has mostly been limited to non-structural or low performance applications in multiprocess AM builds, such as the use of PLA, as reported by Rafiee et al. [47]. Structural performance of 3D-printed parts can be improved by using materials enhanced with structural additives (*e.g.*, short fiber fillers). High-temperature reinforced polymers (HTRP),

such as carbon fiber-reinforced polyether ether ketone (PEEK), has shown high potential for manufacturing high-performance functional parts [49]–[51]. In addition, it is possible to complement the structural reinforcement of a multifunctional part by combining the use of thermosetting materials. It has been shown that thermosetting polymers can be tailored for flame retardancy by adding phosphorus-based additives [52], for electrostatic discharge by reinforcing epoxy resin with graphene [53], and for sound absorption by printing specific stacking patterns of orthogonal filaments, also known as microscaffold [10].

2.1.4 Toolpath generation

AM allows the production of objects by having the printhead follow a toolpath generated from the decomposition of the geometry of a CAD model. Figure 2.4a shows the typical AM toolpath generation workflow. The CAD model is first tessellated into a triangular mesh and then decomposed by intersecting several horizontal slicing planes (hence the popular term "slicing") perpendicular to the *Z* axis direction of the printing bed. The slices are used to generate an AM toolpath compiled as sequential instructions in a machine language (*e.g.*, G-code), which is then interpreted by the 3D printer's firmware to control the hardware and manufacture the part [54], [55]. Based on the printing parameters (*e.g.*, layer thickness, extrusion width, nozzle diameter), traditional planar toolpath generation algorithms approximate the shape of the part. As a result, the inclined and curved surfaces of the part are discretized by the layer parameters, resulting in a stair stepping effect (Figure 2.4b) that increases the local surface roughness [56].

To overcome the stair stepping effect, smooth surfaces can be obtained via non-planar slicing. Non-planar AM toolpaths, achieved by non-planar slicing methods, have become increasingly popular in recent years in both the academic community and industry [57]–[63]. Non-planar AM allows for overhanging features to be printed without support (*i.e.*, excess support material removed after printing), for smooth surface finish and for better mechanical properties of printed parts when compared to traditional planar AM [58], [60], [64]. Several methods have been developed over the years, such as cylindrical projection [65], subdivision of the CAD model into sub-volumes for multi-directional slicing [66], and G-code generation using parameterized curves [67], [68]. Most non-planar slicing methods have been developed for extrusion-based methods and are notably popular for FFF. Figure 2.4c shows one of the main problems of non-planar AM using Cartesian

(*i.e.*, 3-axis) 3D printers. The extrusion nozzle is always oriented vertically along the *Z* axis, which can cause the nozzle to collide with already printed layers. To solve this problem, the use of a printer allowing more than 3 degrees of freedom (DOF) (Figure 2.4d) is necessary in order to orient the nozzle perpendicular to the underlying curved layers [69], [70].

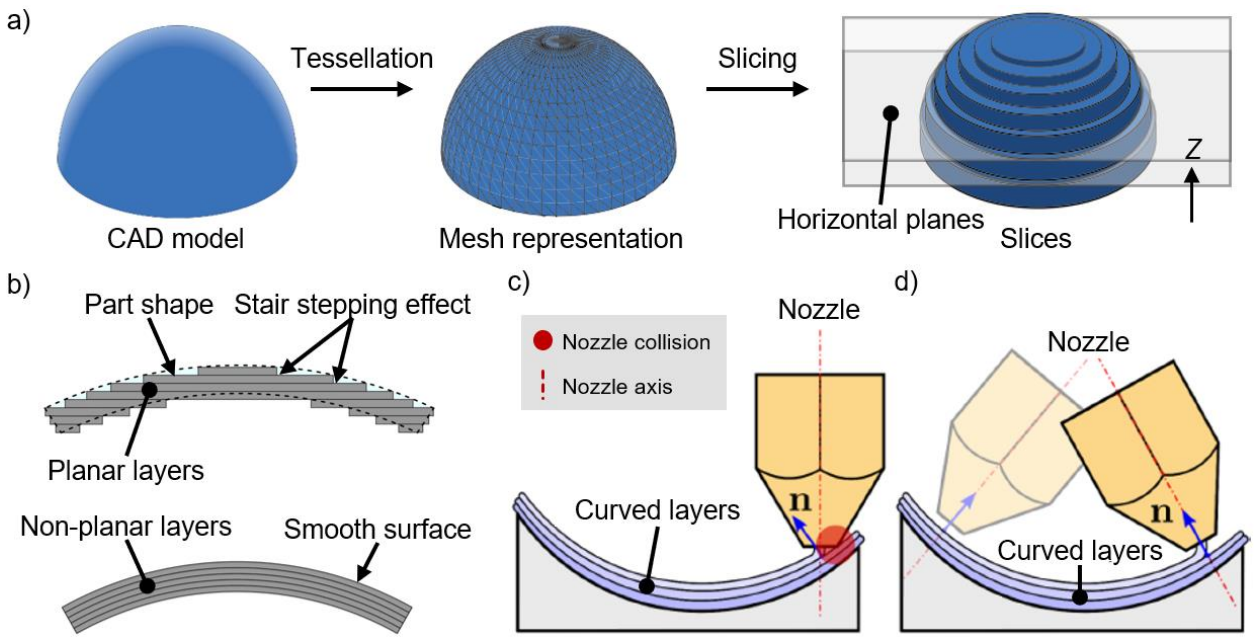

Figure 2.4. a) Typical AM toolpath generation (i.e., slicing) workflow. Adapted from [56]. b) Comparison between planar and non-planar slicing. Stair stepping effect resulting from planar slicing and smooth surface counterpart resulting from non-planar slicing. Adapted from [56]. c) Non-planar AM using 3-axis and nozzle collision. d) Non-planar AM using more than 3-axis (with nozzle orientation). Adapted from [57].

2.2 Industrial 6-axis robot arms

2.2.1 Basic concepts and motion principles

Industrial robot arms with multiple DOF are a type of articulated robot and have been the subject of several studies to improve their efficiency since the advent of automation in the 1960s [71]–[75]. Their operation is based on $k + 1$ body kinematics, comprising two particular bodies (the base and the terminal) as well as actuators; k being the number of DOF of the robot. Figure 2.5a shows the schematic of a 6-axis robot. Actuators are rigid bodies connected by pivot links. For a 6-axis robot, the robot is composed of six pivotal links named J1 to J6 (usually referred as joints) [76].

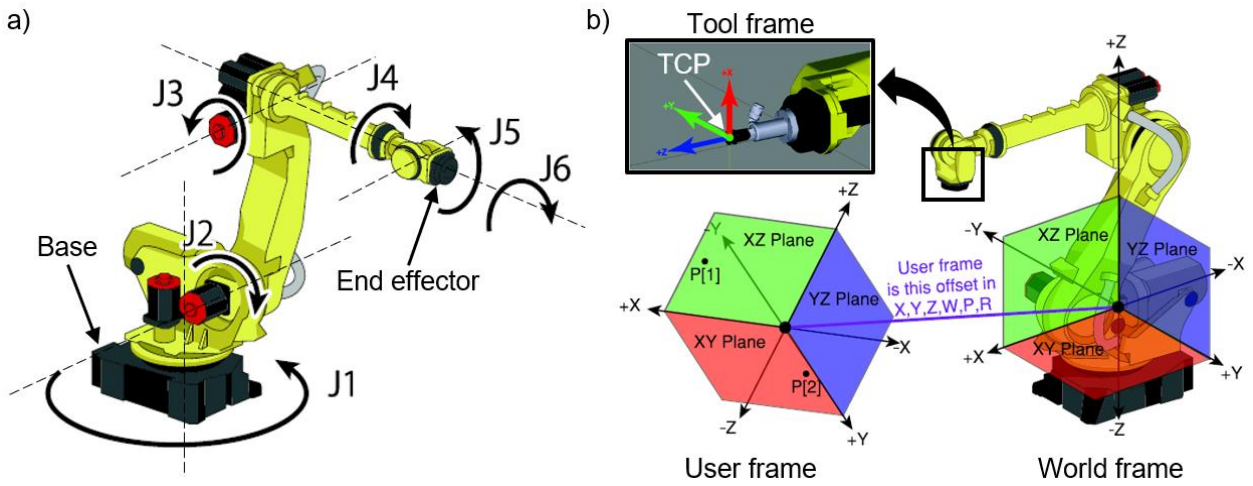

Figure 2.5. a) Schematic of a 6-axis robot arm. Each actuator is connected by a pivot link. b) Reference frames involved in the motion of an industrial robot arm. Adapted from [77].

The robot solves a kinematics problem involving Cartesian reference points (Figure 2.5b). Solving the kinematics equations allows the robot to move the reference frame connected to the end effector (*i.e.*, tool frame) inside the reference frame connected to an object or a part (*i.e.*, user frame), which is itself positioned in relation to the robot base frame (*i.e.*, world frame). The tool frame is obtained by calibrating the tool tip that is equipped on the robot's end effector. The origin of the tool frame, called the Tool Center Point (TCP), is moved by user-programmed positioning instructions, thus following a toolpath. Robot toolpaths can be generated using a robot simulation software and are processed by the robot controller using a path planning algorithm [78]. In automation applications, the goal is usually to operate the robot at a high speed in order to obtain a short production time [79]. Therefore, the path planning algorithm can allow the user to approximate linear tool movements with smoother curved paths, allowing the robot to bypass a given coordinate in favor of a smoother and faster movement. Figure 2.6 shows an example of an approximated linear tool movement. The TCP must move from point P[1] to P[3], passing through P[2], while trying to reach the speed of 100 mm/s at a FINE accuracy. The accuracy can be changed by the CNT continuous motion option. While a FINE accuracy (equivalent to CNT0) forces the robot to decelerate and stop at point P[2] before accelerating again, the opposite value of CNT100 will force the robot to maintain 100% of its maximum programmed TCP speed (or maximum allowed by the path planning algorithm) at the expense of the path accuracy.

Finally, the mathematical problems related to robot dynamics are the "direct" and "inverse" kinematic problems. The direct kinematic problem is simple and involves solving the TCP coordinates along the toolpath by knowing the robot's joint angles. Conversely, the inverse kinematic problem is more difficult and aims at calculating all possible joint angles by knowing the position, velocity, and inertial parameters of the TCP at a given time [80]. Several simulation software on the market deal with solving these problems and are able to generate robot trajectories which can be used as toolpaths for large-scale or non-planar AM applications.

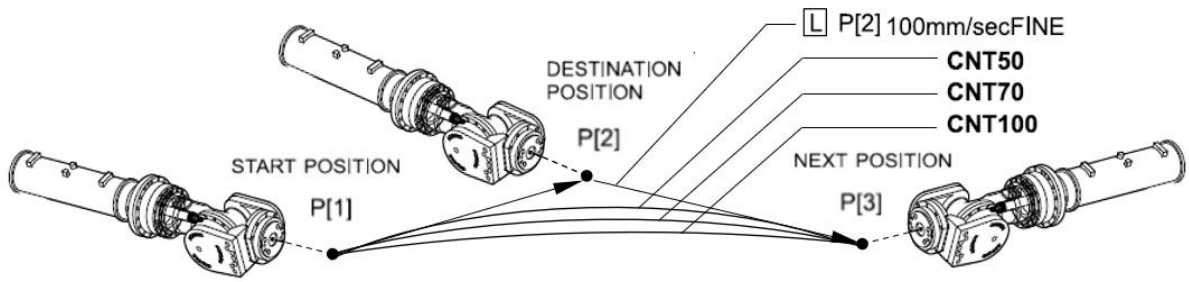

Figure 2.6. Approximated linear tool movement by several continuous robot motion (CNT) at 0 (FINE), 50, 70 and 100%. Adapted from [77].

2.2.2 Non-planar additive manufacturing using 6-axis robots

Commonly used for automation of repetitive tasks such as welding, palletizing, painting and pick-and-place operations, industrial 6-axis robot arms are increasingly being used as motion systems for AM, offering the ability to print in more complex ways with the freedom of multi-directional printing [81], [82]. The potential of using industrial robot arms for large-scale AM builds has been demonstrated for the manufacturing of large, structural parts made of concrete [83], [84], mainly for the construction of buildings [85], but also for research on autonomous habitat construction designed for future use on the planet Mars [86]. In 2018, the Californian-based company Relativity Space reported the 3D printing of a 11-foot-tall rocket fuel tank using robotic arms and a direct metal deposition technique [87]. However, three robotic arms were required, and the part was printed over three weeks. AM using 6-axis robots often take advantage of high flow rate extruders. Companies such as Dyze Design [88] and CEAD Group [89] now offer commercial solutions of pellet extruders which can be mounted on 6-axis robots to extrude thermoplastic materials at very high flow rate (*e.g.*, 500 mm^3/s). Yet, the use of pellet extruders is usually accompanied by

problems such as low resolution (*i.e.*, nozzle inner diameter of a few mm) and lack of retraction [90]. Currently, one of the most advanced and readily available 6-axis robotic AM solution is a line of automated production cells, born from a partnership between software firm Ai Build and robotic manufacturer Kuka [91]. The method involves artificial intelligence to automate, monitor and control the non-planar AM of polymer parts [92].

In the academic sector, there has been an increasing number of studies to develop new large-scale non-planar AM methods using 6-axis robot arms. In 2015, Zhang et al. reported the FFF printing of curved shapes on a flat surface using a 6-axis industrial robot [93]. While the method required support material, this work was one of the first to pioneer non-planar AM using 6-axis robot. Another early study was reported by Zhao et al., in which 6-axis non-planar AM of PLA was demonstrated using a Kuka robot at a printing speed of 30 mm/s (Figure 2.7a) [65]. The method used a cylindrical projection on a planar-generated toolpath to conform to a curved printing bed. Bhatt et al. developed a robotic cell for the non-planar FFF of parts composed of multi-resolution layers and the generation of collision-free trajectories for the printhead (Figure 2.7b) [94]. Other interesting work include the development of a robotic AM system for dynamic build orientation [95], in which it was demonstrated that gravity had no effect on the FFF print quality, and a non-planar toolpath generation method for 6-axis robots using surface parameterization on regular surfaces [96].

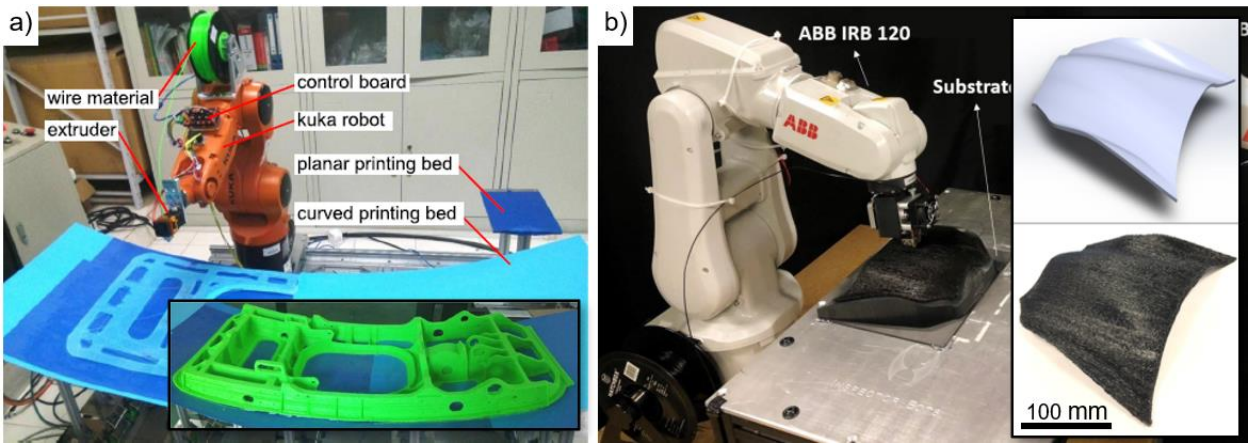

Figure 2.7. Non-planar AM research work using 6-axis robot arm. a) Cylindrical projection method. Adapted from [65]. b) Multi-resolution non-planar AM. Adapted from [94].

AM of large-scale parts composed of small features using 6-axis robot generally involve enormous printing time, depending on the part dimensions, flow rate and nozzle inner diameter [20], [21]. Industrial robot arms are also known to have a better repeatably than accuracy, which can be a problem when the robot trajectory is generated with respect to an absolute coordinate system, as is the case for AM toolpaths [97]. Another challenge is the synchronization between the robot motion and the material extrusion speed. For Cartesian 3D printers, it is allowed to assume that the printhead speed is constant during the movements. Therefore, when an extrusion instruction is processed, the nozzle is fed at a more or less constant speed, thus synchronizing the extrusion speed and the nozzle movement speed. For a 6-axis robot, the assumption of constant speed usually does not hold anymore. The high inertia of the system and the complexity of the kinematic model usually cause significant accelerations and decelerations of the TCP, often resulting in over-extrusion and lower part quality. Some possible solutions to solve this problem include the prediction of the TCP velocity based on an experimental collection of data [98], the jerk optimization (time derivative of the acceleration) [99] or the closed loop control of the TCP velocity for on-the-fly readjustment of the extrusion rate [100].

2.3 Multinozzle printheads for additive manufacturing

2.3.1 Principle, advantages, and disadvantages

Multinozzle printheads are a type of additive manufacturing device composed of two or more extrusion nozzles arranged in a specific configuration [101]. Multinozzle AM can allow simultaneous material extrusion and the resulting deposition is dependent on the arrangement and orientation of the nozzles (*e.g.*, arranged in a row or in other specific patterns). Such devices can allow, among other things, to reduce printing time [12], to print with several different materials at the same time [101] or to print a part with several nozzles of different inner diameters for on-the-fly variable resolutions [102]. However, the use of multinozzle printheads can lead to some disadvantages, including the requirement of special calibration and the limitation of design freedom to the printing of periodic structures (*i.e.*, according to the nozzle arrangement). In addition, the probability of nozzle clogging [103], [104] is increased by the number of nozzles the printhead has, making it more time consuming to unclog the nozzles if necessary. Multinozzle printheads have been previously used in inkjet printer technologies [105]–[108] and for the fabrication of porous

microscaffolds [109]–[111]. Microscaffolds are 3D-printed periodic structure of orderly stacked filaments and are mainly targeted for tissue engineering applications [112]. The AM of microscaffolds composed of parallel lines can be facilitated by using multinozzle printheads.

2.3.2 Current multinozzle additive manufacturing printhead technologies

Multinozzle technologies were initially used in commercial inkjet printheads, such as the Lexmark 7000, for 2D micro-scale deposition of droplets at a precision of ~ 12 µm and could be composed of up to 400 micro-channels with the goal of increasing ejection rate [113]. With the advent of 3D printing, similar AM devices were developed for printing time reduction and multi-material printing. One of the early prototype of multinozzle printhead was developed by Khalil et al. for the multi-material biopolymer DIW of hydrogel tissues [111], [114]. The device was composed of four individual nozzles (Figure 2.8a), controlled separately with their own material reservoir and could provide a flow rate of 0.51 µL/s (*i.e.*, equivalent to a linear extrusion velocity of 15 mm/s). Hansen et al. later fabricated a microvascular multinozzle array out of a block of Poly(methyl methacrylate) (PMMA), for DIW of microcrystalline wax [12], [115]. The device, composed of 64 square-shaped nozzles of 200 µm wide (Figure 2.8b), was later improved by Kranz and was used to 3D print microscaffolds at a printing speed of 40 mm/s (Figure 2.8c) [13]. A 0.38 m² microscaffold of 4 layers was printed in 25 min, which would have taken up to 24 h with a single nozzle at 50 mm/s.

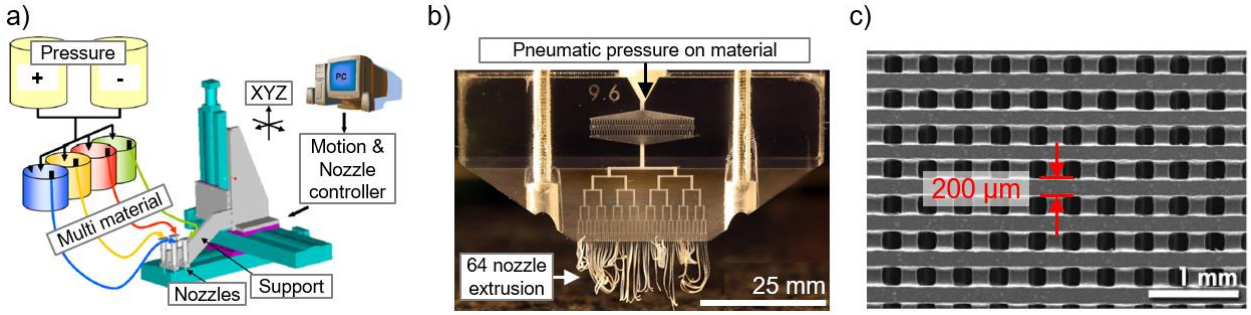

Figure 2.8. Early concepts of multinozzle AM printhead devices. a) Multi-material DIW of hydrogel tissue using four individual nozzles. Adapted from [114]. b) Microvascular multinozzle array fabricated using PMMA, composed of 64 square-shaped nozzles. Adapted from [13]. c) Fabricated microscaffold made of microcrystalline wax. Adapted from [13].

Skylar-Scott et al. developed a multi-material multinozzle AM printhead device by fabricating a series of converging bifurcating channels fitted with pneumatic solenoids (Figure 2.9a) [101]. By

exploiting a diode-like behavior occurring at the junction of converging channels at the outlet of nozzles, the authors were able to seamlessly switch between up to eight different material inside the same nozzle at high frequency (*i.e.*, up to 50 Hz). Their approach allowed the DIW fabrication at 40 mm/s of 3D voxelated patterns by co-printing microcrystalline waxes of four different colors through a 4 × 4 arrangement of 16 nozzles (Figure 2.9b). To highlight the capacity of the multinozzle device, the authors also designed and fabricated a soft robot composed of stiff and flexible silicone inks (Figure 2.9c). Using pneumatic pressure, flexible silicon (blue ink) is able to deform and bend stiff silicon (grey ink), therefore alternatively activating different rows of actuators to achieve forward locomotion at 10 mm/s while carrying a load of 200 g (equivalent to eight times the mass of the soft robot alone).

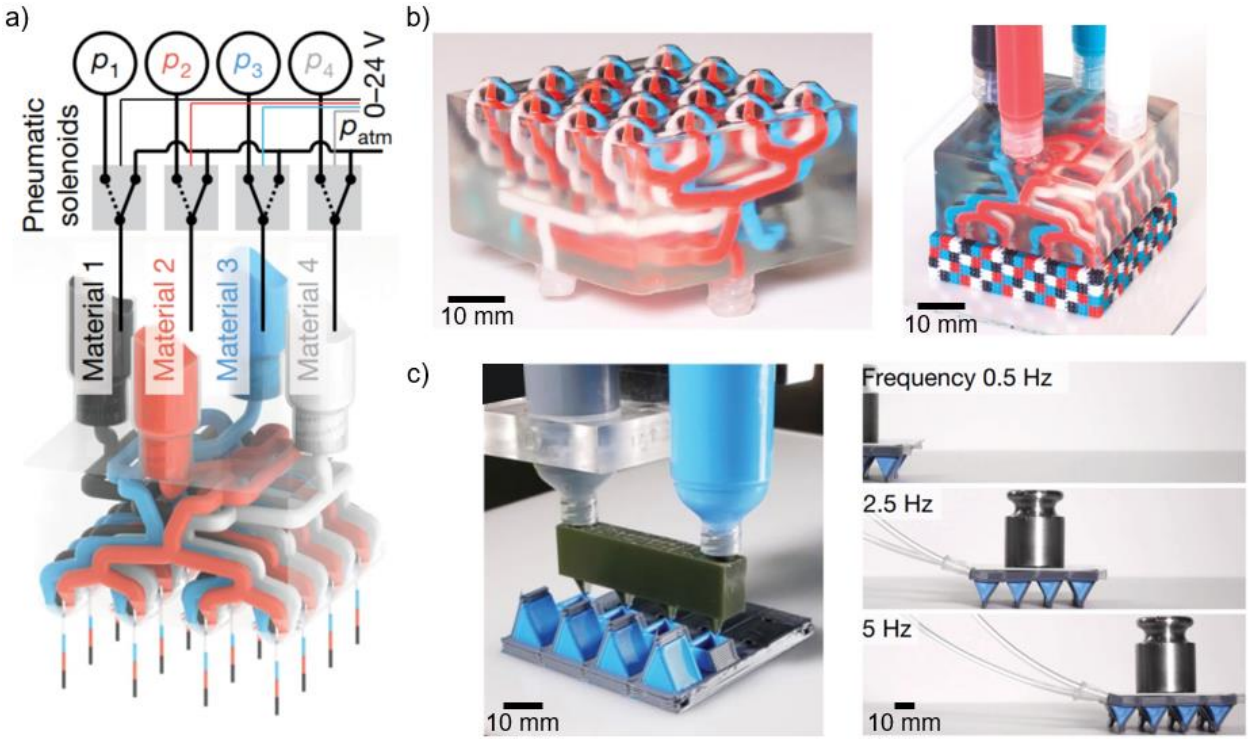

Figure 2.9. Multi-material multinozzle 3D printing device. a) Pneumatic solenoids concept for seamless switching of multi-material at high-frequency. b) Fabrication of 3D voxelated pattern using a multinozzle printhead composed of 16 nozzles in a 4 × 4 arrangement. c) 3D printing of a soft robot made of flexible (blue) and stiff (grey) silicone inks. Adapted from [101].

While multinozzle printheads are mainly used with a DIW approach, some printheads composed of more than one nozzle have been developed for the FFF technique. Yoon et al. designed and built

a three-nozzle system and installed it on a 6-axis robot for the non-planar multi-material AM of multi-resolution thermoplastic parts [102]. Figure 2.10a shows a 3D model of their prototype. The three independent nozzles (E3D Volcano hot end) can be actuated during the print to change the part's resolution on the fly. Although the device does not allow for simultaneous extrusion of the nozzles, some multi-material non-planar parts were fabricated in PLA at different resolution using this technique [116]. The company E3D developed the Kraken, an FFF printhead which holds four nozzles in a 2 × 2 arrangement (Figure 2.10b) [117]. The device can hold up to four heat blocks to heat all nozzles and requires water cooling to function. Baca and Ahmad demonstrated the use of the Kraken for multi-resolution AM [118]. Using each individual nozzle sequentially, they fabricated standard tensile test specimens and compared their mechanical performance with that of specimens fabricated using a single nozzle. They concluded that although the printing time was reduced using the Kraken, mechanical properties did not change significantly.

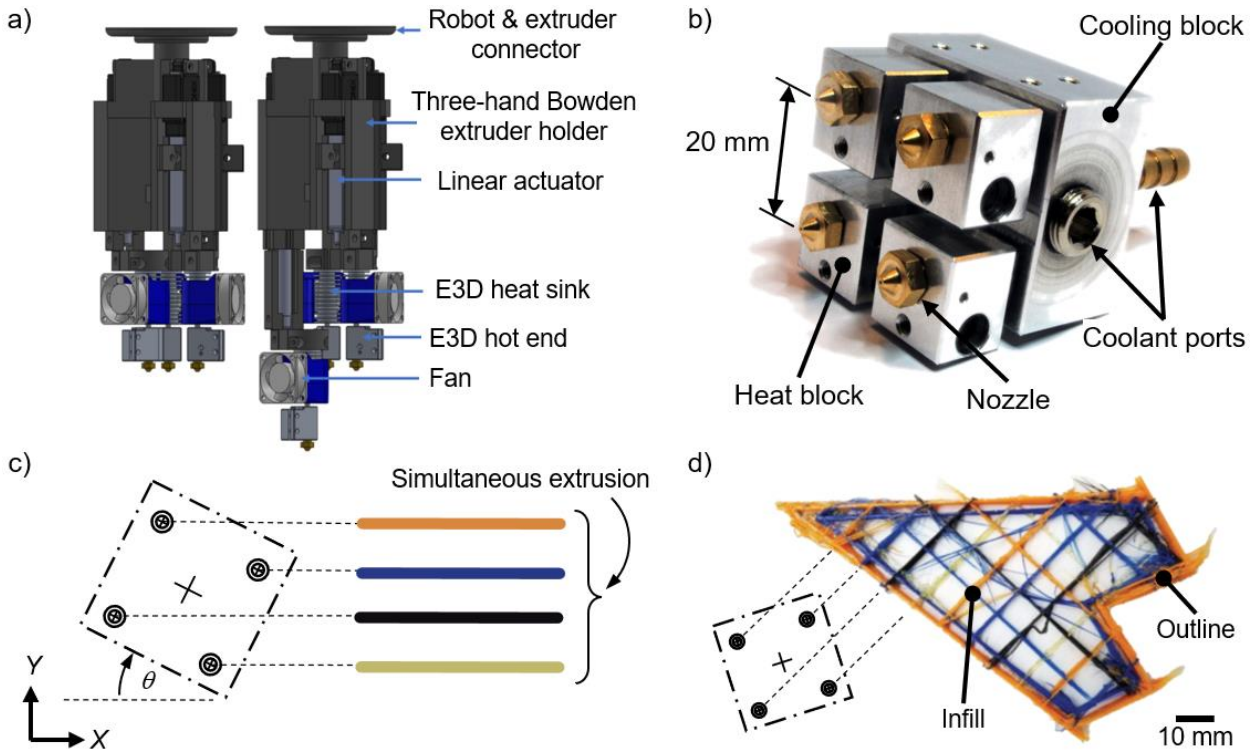

Figure 2.10. FFF technique using more than one extrusion nozzle. a) Three-nozzle system for multi-resolution FFF on 6-axis robot. Adapted from [102]. b) E3D Kraken printhead for extrusion of up to four thermoplastic filaments. Adapted from [117]. c) Printhead rotation around the *Z* axis

to simultaneously extrude four side-by-side filaments. d) Multinozzle 3D printing of a polygon shape using four different thermoplastic filaments. Adapted from [119].

As part of a master's thesis, Mhatre developed a path planning algorithm for the simultaneous FFF of thermoplastic filaments using the Kraken [119]. The open-source software Slic3r was modified to create a 4-axis multinozzle toolpath generator, which basically allows the addition of a degree of rotation around the *Z* axis, so that the extruded filaments would be printed side-by-side, regardless of the printing direction (Figure 2.10c). Figure 2.10d shows a polygon-shaped part manufactured using the method. By switching between simultaneous and selective extrusion, Mhatre managed to print the outline and infill of the parts at ~ 17 mm/s in a single AM step. The quality of the print is however not quantified, and the method is limited to planar prints. Non-planar multinozzle AM involving simultaneous extrusion was investigated by Uzel et al. [120]. Figure 2.11 shows the developed prototype in operation. A multinozzle printhead was fabricated using 16 nozzles of 1.37 mm inner diameter, each mounted on a vertical linear actuator (Figure 2.11a). A non-planar substrate was scanned to compute the individual print path of each nozzle (Figure 2.11b). The relative height variation of the nozzles with respect to the substrate topography is then programmed to follow the curvature of the substrate and achieve the deposition of 10 conformal layers of soft material (Figure 2.11c). The dimensions of printed parts are relatively small (*i.e.*, few cm wide) and the printhead is mounted on a 3-axis gantry, which produces a printing speed of 5 mm/s, only following one direction. The method is also limited by the deposition angle between the substrate and the nozzles (which are always kept in a vertical position). Table 2.1 presents a summary of select developed multinozzle AM printhead technologies. Multinozzle printheads could be potentially used in the next few years for the rapid production of functional parts such as the 3D printing of soft sensors found in wearable electronics [121].

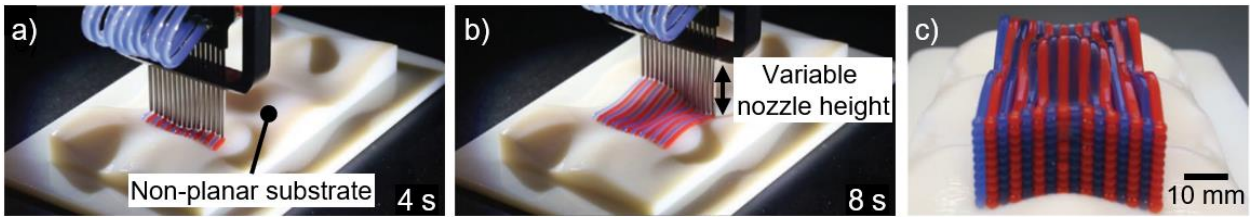

Figure 2.11. Multi-material multinozzle adaptive 3D printing of soft materials at 5 mm/s. a) 4 s into printing. b) 8 s into printing. The nozzles height varies with the substrate topography. c) Resulting 10 conformal layers. Adapted from [120].

Table 2.1. Summary of select multinozzle AM printhead technologies

Authors	Highlights	Image	Reference
Khalil et al. (2005) Khalil and Sun (2007)	• 4 independent nozzles, different materials • Flow rate of 0.51 µL/s • Printing speed of 15 mm/s	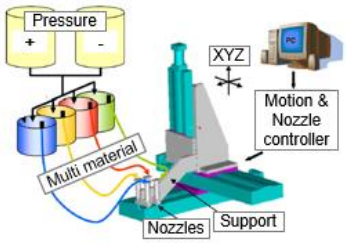	[111], [114]
Hansen et al. (2013) Kranz (2013)	• 64 nozzles of 200 µm wide • Machined in PMMA block • Printing of 0.38 m² 4-layer microscaffold in 25 min at printing speed of 40 mm/s	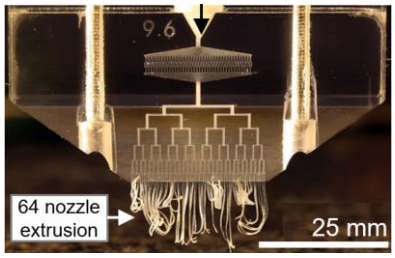	[12], [13]
Skylar-Scott et al. (2019)	• 16 nozzles of 250 µm inner diameter • Printing speed of 40 mm/s • Multimaterial shifting frequency of 50 Hz	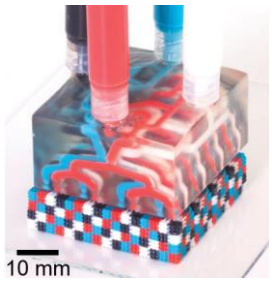	[101]
Yoon et al. (2019)	• 3 FFF extruders for **independent extrusion** (E3D volcano) • Mounted on 6-axis robot • Variable resolution (0.15 – 0.8 mm)	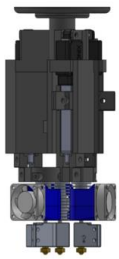	[102], [116]
Baca and Ahmad (2020) Mhatre (2019)	• 4 FFF extruders for **simultaneous extrusion** (E3D Kraken) • Printing speed of 17 mm/s • Variable resolution (0.15 – 0.8 mm)		[118], [119]
Uzel et al. (2022)	• Non-planar multinozzle AM • Variable nozzle height • Printing speed of 5 mm/s • Printing in one direction, adaptable to the substrate scanned topography	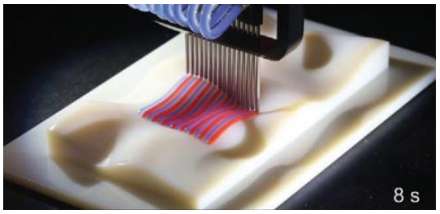	[120]

2.4 Abradable seal coatings in aerospace industry

Abradable coatings have been used in the aerospace industry as seals in turbine engines since the late 1960s. Applied primarily at the compressor and turbine, they allow for very small clearances at the interface between the rotor blade tip and the rotor blade casing [122]–[124]. Figure 2.12a illustrates the principle of material removal from an abradable coating inside a casing. These tight clearances, whose tolerance level would be difficult to achieve by mechanical means, are obtained by the abrasion of the coating due to the elongation of the rotor blades during rotation [9], [122], [125]. Good abradability of such coatings is crucial to avoid damaging the blades [126], [127] as blade wear or material adhesive transfer from the abradable coatings to the blades can lead to friction induced overheating and possible catastrophic accidents [128], [129].These coatings also represent an opportunity to save on aircraft fuel consumption [130] and reduce their environmental impact. As an example, a 0.0254 mm gain in the clearance of a high-pressure turbine abradable seal represents a 0.1 % decrease in specific fuel consumption. This equates to 0.02 billion gallons in annual fuel savings for the U.S. commercial aircraft fleet [9].

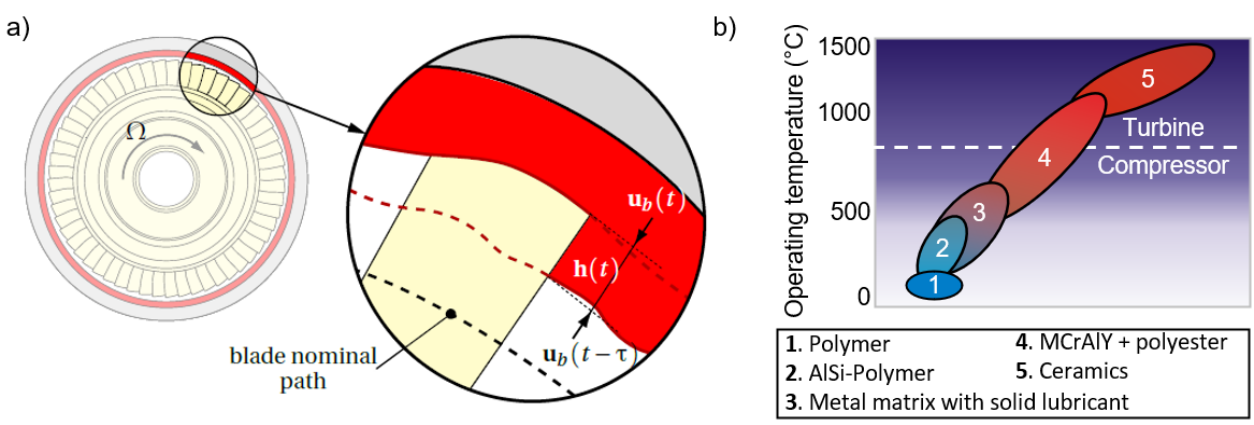

Figure 2.12. a) Schematic of the abrasion of an abradable layer (red). Due to the rotation of the fan, the blade is elongated from its nominal path to remove a layer of abradable material. Adapted from [131]. b) Types of abradable materials (1-5) according to their operating temperature (0 – 1500 °C). Adapted from [132].

2.4.1 Types of abradable materials

Since abradable coatings are used in many areas of the engine, five different types of abradable materials, as shown in Figure 2.12b, are used in the industry for different operating temperatures

[122], [129], [132]. In the low temperature zone (i.e., < 500 °C) are the upstream regions of the engine such as the fan and the low pressure compressor. Material types 1, 2 and 3, composed respectively of polymer, AlSi and a metal matrix comprising a solid lubricant, are generally used in this region [128], [129]. A polymer-based mixture (*i.e.*, epoxy resin and various additives such as Teflon or alumina-silica microspheres) is typically used to avoid galvanic corrosion problems [128], [133]. A commercial epoxy-based void-filling material (Scotch-Weld EC-3524 B/A Black) developed by 3M has been used as the abradable coating material on aircraft engine fan casings in the industry [134]. This abradable material is composed of ~ 22.5 wt% of hollow glass microspheres (GM), which provides multiple functionalities such as weight reduction and porosity control. The porosity of abradable material mainly reduces its hardness and enhance the abradability of the coating [128]. For medium temperature areas (*i.e.*, up to ~ 760 °C) such as the high pressure compressor and the low pressure turbine, the material type 4 is used and consists of MCrAlY alloys or metals based on Ni or Co powder. At high temperatures (*i.e.*, up to 1500 °C), the material type 5 is used in the high-pressure turbine area and is composed of porous ceramics made from YSZ (Yttria-Stabilized Zirconia) [9].

2.4.2 Current application methods

Different abradable material application methods exist depending on the type of material used, as presented in Section 2.4.1. Table 2.2 provides a summary of the types of abradable materials and their respective application methods. Molding, spatula and pneumatic gun processes are used for abradable materials used in the low temperature area. With this method, a porosity of 35 – 40 % is achievable and final dimensions of the coating are generally obtained by a second machining operation [133]. Similarly, MCrAlY-based abradable materials, deposited by brazing or diffusion bonding, require a post-deposition curing treatment to remove a sacrificial amount (*i.e.*, ~ 15 wt%) of polyester that serves to control porosity (*i.e.*, 35 – 40 %) [135]. In the case of thermal spraying, porosities are usually in the range of 20 – 25 %. The reproducibility of the thermal spraying is highly dependent on the process parameters. Moreover, Batra has shown that this process is not very efficient (deposition efficiency of less than 40 %) for thermal spraying of Ni [136]. Generally, most processes allow coatings up to 2 mm thick.

Table 2.2. Summary of abradable material types and their application process

Material type	Location	Component	Application method
Type 1, 2, 3 Low temperature (0 – 500 °C)	Fan, low pressure compressor	Polymer (epoxy), AlSi, metal matrix with solid lubricant	Molding, spatula, pneumatic gun
Type 4 Medium temperature (500 – 760 °C)	High pressure compressor, low pressure turbine	Alloys of MCrAlY + polyester, Ni or Co powder	Brazing and diffusion bonding
Type 5 High temperature (760 – 1500 °C)	High pressure turbine	YSZ ceramic	Thermal spraying

2.4.3 Additive manufacturing of abradable acoustic coating for aircraft

In 2015, Dubourg-Cassagne was interested in the proof of concept of manufacturing an abradable coating intended for the low temperature zone with the goal of reducing the noise generated by this part of the engine [10]. This master's project, carried out at the Laboratory for Multiscale Mechanics (LM^2) and the Laboratory for Acoustics and Vibration Analysis (LAVA) at Polytechnique Montreal in collaboration with Safran (France), studied the use of AM (specifically DIW, see Section 2.1.2) to produce acoustic structures made of an aerospace-grade abradable epoxy material with controlled porosity of up to 70 %. The research demonstrated that DIW can be used to produce samples in the shape of planar abradable microscaffolds, which are known to be efficient for sound absorption of specific targeted frequencies [137]. A microscaffold coating with dimensions of 100 × 40 × 12.7 mm was printed over a 10-hour period using a single conical nozzle (outlet inner diameter of 250 µm) controlled by a 4-axis robot (I&J Fisnar) at a printing speed of 25 mm/s. The method required 12 syringes of 3 cm^3 to complete the fabrication of the sample. In order to extrude the material, Dubourg-Cassagne reduced the viscosity of the abradable material by adding ~ 8 wt% of petroleum jelly, which however reduced its mechanical properties. The abradability of the manufactured porous microscaffold structures was not tested.

The AM of aerospace-grade abradable thermosetting material was then pursued by Brzeski et al. within the context of the FACMO Chair at Polytechnique Montreal, in the Laboratory for Multiscale Mechanics [11]. The researchers developed a series of 3D-printable thermosetting abradable material blends, based on the commercial epoxy-based abradable material used in the

industry (*i.e.*, EC-3524 [134]). Figure 2.13a shows the fabrication of a disc-shaped specimen (30 mm diameter, 5 mm thick), composed of an internal microscaffold geometry (Figure 2.13b), using the DIW technique. A conical nozzle of outlet inner diameter of 250 µm was used to print a microscaffold at 50 mm/s, requiring a pressure of 2.8 MPa using pneumatic dispensing system. Three promising blends, composed of 0 – 10 wt% of hollow GM and 0 – 12 wt% hydrophilic fumed silica (FS), were developed to achieve printability of the abradable material with proper post-printing shape retention. The printed samples' acoustic absorption coefficient was measured using an impedance tube (Figure 2.13c) and compared to an acoustic simulation obtained using the JCAL model (Figure 2.13d) [138]–[140]. Although the reported acoustic absorption curves (colored symbols) agreed relatively well with the simulation (dashed line), the fabrication of the abradable microscaffold was conducted at a small scale, which is not conceivable for the AM of a large abradable coating aimed for the interior of an aircraft engine. The study also did not report any results on the abradability of the coatings. The typically long printing times encountered with the DIW technique would not allow the fabrication of a full size abradable coating without reaching the curing time of the thermosetting material, in which case the material would solidify, preventing its extrusion.

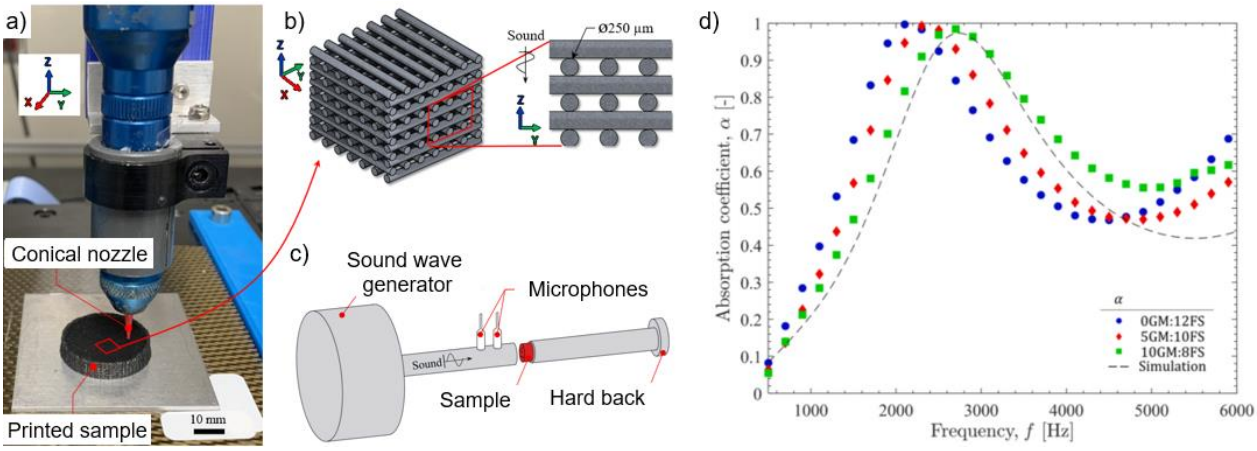

Figure 2.13. a) Fabrication of a microscaffold sample in the shape of a disc. The filaments are printed using a 250 µm conical nozzle using a pneumatic dispensing system at 2.8 MPa. b) Internal microscaffold structure composed of orthogonal filaments. c) Impedance tube for acoustic absorption characterization. d) Acoustic absorption coefficient of the three promising abradable material blends compared with the JCAL simulation. Adapted from [11].

2.5 Summary of literature review

FFF and DIW techniques have been extensively used for AM over the past decade and have been more recently combined to manufacture multifunctional components. As 3D printing is being used increasingly in the manufacturing industry, multifunctional parts are of interest to be used in planes, rockets and automobiles. Yet, one of the main disadvantages of printing large parts is the long printing time, sometimes reaching days for very large builds. Non-planar slicing methods aim at generating a modified machine language (G-code) for 3D printers to avoid using support material (among other things), which can be very beneficial to save time in the production of large complex parts composed of overhanging features. However, non-planar slicing techniques have mainly shown development interest for material extrusion using a single nozzle, and their use with traditional Cartesian 3D printers (*i.e.*, with 3-axis) have limitations due to potential collision of the vertically-oriented nozzle with the curved printed part.

Over the past few years, industrial 6-axis robot arms have been used as efficient motion systems for non-planar AM and have shown high potential for large-scale AM. With access to more than three DOF, 6-axis robots can freely rotate and orient the printhead's nozzle to perpendicularly follow the curvature of almost any substrates. However, the use of 6-axis robots for non-planar AM does not solve the problem of long printing times in the case of manufacturing large-scale parts composed of micro-scale deposited filaments.

Multinozzle printheads for AM have been shown to reduce the printing time of fine periodic ordered structures such as microscaffolds, by simultaneously extruding more than one filament. To date, the only non-planar AM method that involves a multinozzle printhead is able to print in only one direction and the demonstrated printing speed is very slow (*i.e.*, 5 mm/s) [120]. The method does not allow full freedom of the printhead orientation either.

The AM of abradable thermosetting materials using DIW with single nozzle has shown the potential of manufacturing abradable seal coatings for aircraft with controlled porosity by printing small-scale microscaffolds. Although printed abradable thermosetting laboratory-scale microscaffolds have shown potential for sound absorption capability, the manufacturing of an actual large-scale non-planar abradable seal component for aircraft with added functionalities is not possible with current developed AM methods.

CHAPTER 3 RESEARCH OBJECTIVES AND COHERENCE OF ARTICLES

3.1 Problem identification

Large-scale non-planar multinozzle AM using a 6-axis robot could show great potential for manufacturing large non-planar thermosetting microscaffolds. Such AM method could be used to manufacture actual abradable coatings destined for aircraft casings with the added functionality of sound absorption. However, the following issues regarding this approach need to be addressed:

- Current multinozzle printhead technologies are limited to relatively low flow rates and low viscosity materials.
- Non-planar slicing algorithms are mainly focused on FFF and non-planar multinozzle AM with complete freedom of printhead orientation has never been demonstrated.
- DIW of thermosetting composites is often limited to small-scale applications and its integration into multiprocess AM of large-scale, high-resolution multifunctional components remains to be proven.

3.2 Research objectives

The main objective of this research is to develop a non-planar multinozzle AM approach using a 6-axis robot to achieve the large-scale manufacturing of thermosetting-based high-resolution multifunctional periodic structures that are inspired by sound absorption patterns. The specific objectives are presented as the following:

I. **Expand the development of multinozzle printheads in support of high-speed AM of relatively large periodic structures**. The objective is to develop a 6-DOF robotic AM infrastructure to characterize and improve the performance of a custom multinozzle printhead. The development of a model is required to predict the required extrusion pressure and volumetric flow rate of multinozzle printheads and to investigate the effect of different parameters on the predicted performance of several multinozzle printhead configurations.

II. **Develop a non-planar multinozzle toolpath generator compatible with 6-axis robots**. The objective is to develop a code to design and generate non-planar multinozzle toolpaths

with complete freedom of printhead orientation. The non-planar AM approach requires obtaining the topography of non-planar substrates using a 3D scanner, verifying possible nozzle collision with curved substrates, and solving the inverse kinematic problem for 6-axis robot motion planning.

III. **Implement the non-planar multinozzle AM method to integrate an abradable composite material into the multiprocess AM of a large multifunctional component**. The objective is to demonstrate the large-scale non-planar multinozzle AM of multifunctional thermosetting composites. The objective includes fabricating a large non-planar aircraft component demonstrator featuring a functional sandwich panel coated with an abradable thermosetting microscaffold network with controlled porosity levels inspired by sound absorption.

3.3 Coherence of articles

The main results of this research are presented in the form of accepted and submitted peer-reviewed journal articles in Chapter 4, 5 and 6, which address specific objectives I, II, and III, respectively.

Chapter 4 presents the article entitled "*High-speed multinozzle additive manufacturing and extrusion modeling of large-scale microscaffold networks*". In this work, a custom multinozzle printhead was fitted to a 6-axis industrial robot arm for the high-speed AM of large planar microscaffold networks. High printing speed was demonstrated while preserving fine printed features. A Multinozzle Extrusion Prediction Model (MEPM) was also developed and validated. Prints were analyzed to characterize the simultaneous extrusion quality. This article was published in the journal Additive Manufacturing (https://doi.org/10.1016/j.addma.2021.102294) on September 11, 2021. The mission of the selected journal is to acknowledge and highlight the innovative progress of additive manufacturing. This journal was selected because its field of work is perfectly suited to the results and innovative nature of our developed method. Mr. Chauvette designed and performed the experiments, analyzed the data, and wrote the article under the supervision of Prof. Daniel Therriault with revisions by Dr. Farahani. Mr. Chauvette programmed the MEPM with the help of Mr. David Brzeski. Dr. Farahani and Dr. Hia helped with the experiments. Dr. Piccirelli, our industrial partner, provided technical advice.

Chapter 5 presents the article entitled "*Non-planar multinozzle additive manufacturing of thermoset composite microscaffold networks*". In this work, a custom Multinozzle Toolpath Generator (MTG) was programmed to generate non-planar multinozzle toolpaths and obtain 6-axis robot trajectories that follow the curvature of 3D-scanned substrates. A tailored epoxy composite was printed to demonstrate the non-planar multinozzle AM of large microscaffold networks, which were predicted and analyzed for single curvature and a double curvature surfaces, with a toolpath error of 15 µm. This article was published in the journal Composites Part B: Engineering (https://doi.org/10.1016/j.compositesb.2023.110627) on February 25, 2023. This journal covers novel composite integration in aerospace, with emphasis on engineering validation and manufacturing. This journal was selected because of his focus on new composite manufacturing applications, which is at the core of this work. Mr. Chauvette programmed the MTG, designed and performed the experiments, analyzed the data, and wrote the article under the supervision of Prof. Daniel Therriault with revisions by Dr. Farahani. Dr. Hia and Mr. Plante helped with the experiments. Dr. Hia developed the epoxy material. Dr. Piccirelli, our industrial partner, provided technical advice.

Chapter 6 presents the article entitled "*Non-planar multiprocess additive manufacturing of multifunctional composites*". In this work, a multiprocess non-planar AM approach was demonstrated to fabricate a large multifunctional aircraft component demonstrator, using a multinozzle to rapidly print a custom abradable thermosetting composite on top of an HTRP sandwich panel structure. The multifunctionality of the demonstrator was obtained by controlling the porosity of the non-planar printed microscaffold, inspired by sound absorption patterns, and by comparing its abradability with a commercial abradable material used in the aerospace industry. This article was submitted to the journal Advanced Materials Technologies on March 13, 2023. This journal covers research on material science, processing, structure, properties, and advanced functional materials. This journal was selected because it deals with innovations in the field of multifunctional materials and processing, which the article tries to demonstrate. Mr. Chauvette, Dr. Hia, Ms. Pierre and Mr. Chenier designed and performed the experiments. Mr. Chauvette implemented the MTG, analyzed the data and wrote the article with the help of Dr. Hia under the supervision of Prof. Daniel Therriault with revisions by Dr. Farahani. Dr. Hia adapted the abradable material for multinozzle AM. Dr. Piccirelli, our industrial partner, provided technical advice.

CHAPTER 4 ARTICLE 1: HIGH-SPEED MULTINOZZLE ADDITIVE MANUFACTURING AND EXTRUSION MODELING OF LARGE-SCALE MICROSCAFFOLD NETWORKS

Jean-François Chauvette[1], David Brzeski[1], Iee Lee Hia[1], Rouhollah D. Farahani[1], Nicola Piccirelli[2], Daniel Therriault[1]

[1]Laboratory for Multiscale Mechanics (LM[2]), Mechanical engineering department, Polytechnique Montréal, Montréal, Québec H3T 1J4, Canada

[2]Safran Composites, 33 Avenue de la Gare, Itteville, 91760, France

Published in Additive Manufacturing on September 11, 2021

Abstract

In this work, a six-degree-of-freedom (6-DOF) robotic infrastructure is used for the high-speed additive manufacturing (AM) of large-scale networks of high-resolution scaffolds made of microfilaments, referred as microscaffold networks. The use of a multinozzle printhead, featuring an extrusion nozzle array of 26 cylindrical nozzles of 250 µm inner diameter, enabled the AM of microscaffolds with very high flow rate (*i.e.*, > 300 mm³/s) and printing speed (*i.e.*, up to 250 mm/s) while preserving fine features. A Multinozzle Extrusion Prediction Model (MEPM), based on capillary rheometry, was developed to predict the extrusion pressure gradient and the overall total volumetric flow rate of the printing process. The MEPM predictions are made as a function of the material used, printing speed and multinozzle printhead configuration (*i.e.*, nozzles inner diameter and number of nozzles). Experimental pressures and flow rates strongly match the MEPM predictions for a printing speed range of 0 to 250 mm/s. The MEPM is also used to explore the design of other multinozzle configurations. The advantages of the high-speed multinozzle AM infrastructure is demonstrated through four case studies. The high-speed printing of microscaffold network demonstrated a printing speed of up to 250 mm/s, with flow rate of ~ 319.4 mm³/s. The 6-DOF of the robot are used to manufacture a variable pore size microscaffold network, which shows an achievable inter-filaments spacing of 0 to 750 µm. The printing of a large-scale partitioned microscaffold network spans over an area of ~ 9×10^4 mm². Finally, a relatively thick partitioned microscaffold network is manufactured up to 50 layers (~ 10 mm thick). Findings of this work contribute to the development of multinozzle printheads, high-speed 3D printing and high-

resolution microscaffold manufacturing, which could be targeted for a wide range of applications including sound absorption, smart materials, and tissue engineering.

4.1 Introduction

Additive Manufacturing (AM), or three-dimensional (3D) printing, is a group of manufacturing methods that allow the realization of complex objects based on the principle of the superposition of layers of material according to the decomposition of a computer-assisted design model [22]. Expanding since the early 1980s [15], AM now offers a broad range of benefits such as low cost, mass optimization, reduction of material losses, a high design freedom and a large diversity of compatible materials [18]. Most common techniques rely on material extrusion (*e.g.*, Fused Filament Fabrication, Direct-Ink-Writing (DIW)). DIW is based on the concept of continuous extrusion of filamentary materials, called ink, through a fine nozzle. Pressure is increased at the inlet of a reservoir by pneumatics, hydraulics, or an endless screw to extrude the material. When using a non-Newtonian shear-thinning ink, the extrusion occurs when the fluid is subjected to a shear stress through the nozzle. The viscosity of a shear-thinning ink decreases with increasing shear rate, generally following a power law, causing the ink to exit the nozzle and solidify on the printing surface to achieve the desired geometry [18], [25], [28].

DIW is often used with soft polymers, hydrogels, or other paste-like materials to manufacture compact high resolution scaffolds involving micro-scale features, referred as microscaffold [6], [141], small complex metallic structures [142] or microfluidic devices [143]. DIW is highly flexible, but is generally limited by a slow to moderate printing speed (~ 1 up to 100 mm/s) which could lead to long printing time, especially for the AM of parts where the printed volume is significantly larger than the nozzle diameter. Bey-Oueslati et al. [29] investigated high-speed DIW using a cylindrical nozzle of 200 µm inner diameter and a low viscosity paste-like organic ink (*i.e.*, mix of wax and petroleum jelly developed in [115]). The authors reported a maximum printing speed of 88 mm/s for the AM of a compact 54-layer microscaffold (~ 19 mm × 19 mm wide × ~ 7 mm thick). The printing process required a toolpath approximation using B-splines to reach 88 mm/s, which led to some discrepancies with the expected geometry. Printing speed in DIW is usually constrained by the applied pressure, nozzle tip inner diameter and material used [28], [144]. Slightly larger scale DIW was explored by Dubourg-Cassagne [10]. A panel-shaped microscaffold

(100 mm × 40 mm wide × 12.7 mm thick) was printed using a single nozzle (250 µm inner diameter) with a highly viscous epoxy-based thermosetting polymer. The AM required a period of 10 hours at printing speed of 25 mm/s and refilling the material reservoir (*i.e.*, a 3 cm^3 syringe) 12 times.

A multinozzle printhead is a device that allows the simultaneous material extrusion through a series of nozzles arranged in a specific configuration. Multinozzles were used to reduce printing times for structures made of parallel lines [12], print multi-material parts in a single step [101] and print parts at variable resolutions [102]. In general, multinozzle printheads deposit filaments according to the arrangement and orientation of their nozzle array, which limits their use to the production of periodic patterns. Skylar-Scott et al. [101] printed a periodic voxelated prism (~ 40 mm × 40 mm wide × 10 mm thick) made of an organic ink (using the same material developed in [115]) of four different colors using a multi-material multinozzle printing head. Their device allowed the AM at a moderate printing speed of 40 mm/s. The multinozzle AM of a large-scale microscaffold (using the same material developed in [115]) was demonstrated by Kranz [13] with a device composed of 64 nozzles of rectangular section of 200 µm × 200 µm. The printing process produced a 4-layer microscaffold (616 mm × 616 mm × ~ 800 µm thick) at a maximum printing speed of 40 mm/s in 25 minutes using an Aerotech gantry motion system. The use of gantries and 6-axis industrial robots allows the AM of large parts made of concrete [83], [84], metals [145]–[147] and polymers [94], [95], [98]. However, as for DIW, the AM of large parts is usually time-consuming, especially to obtain a smooth surface finish [94].

In this work, a custom six-degree-of-freedom (6-DOF) robotic AM infrastructure is combined to a custom-made multinozzle printhead for the high-speed fabrication of relatively large-scale microscaffold networks. While this paper focuses on the proposed multinozzle AM method, it is planned to exploit the 6-DOF of the robot to print non-planar microscaffold networks. The main objectives of the current work are: (1) to demonstrate the high-speed multinozzle AM by creating large multifunctional periodic structures and reducing the printing time while maintaining high-resolution features, and (2) to develop a multinozzle extrusion prediction model.

4.2 Experimental methods

4.2.1 6-DOF robotic AM infrastructure

A 6-axis industrial robot (Fanuc M-20iB/25, Fanuc Canada Ltd., Canada) equipped with a custom-made multinozzle extrusion printhead (Mëkanic – FACMO Chair collaboration, Montreal, Canada) is used for the large-scale AM of microscaffold networks. Figure 4.1a presents the 6-DOF robotic AM infrastructure. The 6-axis robot has a maximum reach of 1.8 m and a maximum tool movement speed of 2 m/s, which are exploited for large-scale and high speed AM. The robot can move the printhead mounted on its arm in any required orientation. The robot is a flexible motion system on which various tools up to a maximum weight of 25 kg can be mounted, such as the custom-made multinozzle printhead of 18 kg. The multinozzle printhead is connected to a custom-made hydraulic pressure controller that can produce an extrusion pressure of up to 65 MPa. The printhead is programmed to operate the desired printing speed v. The current printhead is composed of 26 parallel cylindrical nozzles with nominal inner diameter D = 250 µm and nominal length L = 6.5 mm, equally distributed side-by-side by a center-to-center spacing s = 1 mm. The printing speed v is determined by the user input of a desired linear extrusion velocity at the nozzle exit. Pressure is increased in a hydraulic oil, which displaces a piston that pushes the material through the array of nozzles from a 50 cm³ reservoir, at room temperature. To meet the target printing speed v, the piston's displacement is controlled by a position sensor (Temposonics R-series RH, MTS, NC, USA). Figure 4.1b shows a close-up view of the multinozzle printhead extrusion. The material is extruded through all 26 nozzles simultaneously, creating a strip of ~ 25 mm wide of individual filaments that are deposited on a printing surface in a layer-by-layer fashion. By synchronizing the extrusion printing speed with the movement of the robot tool center point (TCP), located in the center of the nozzle array, the printed filaments diameter d is theoretically equal to D.

At the end of extrusion, a back pressure is applied in order to stop the flow rate, which slightly retracts the piston backward, with the help of a compressed spring installed in an upper part of the piston (not shown in Figure 4.1). To record the applied pressure gradient required for material extrusion during the print, the back pressure generated by the spring is recorded alone and is then subtracted from the recorded hydraulic pressure data (see additional explanations in supplementary Figure 4.9).

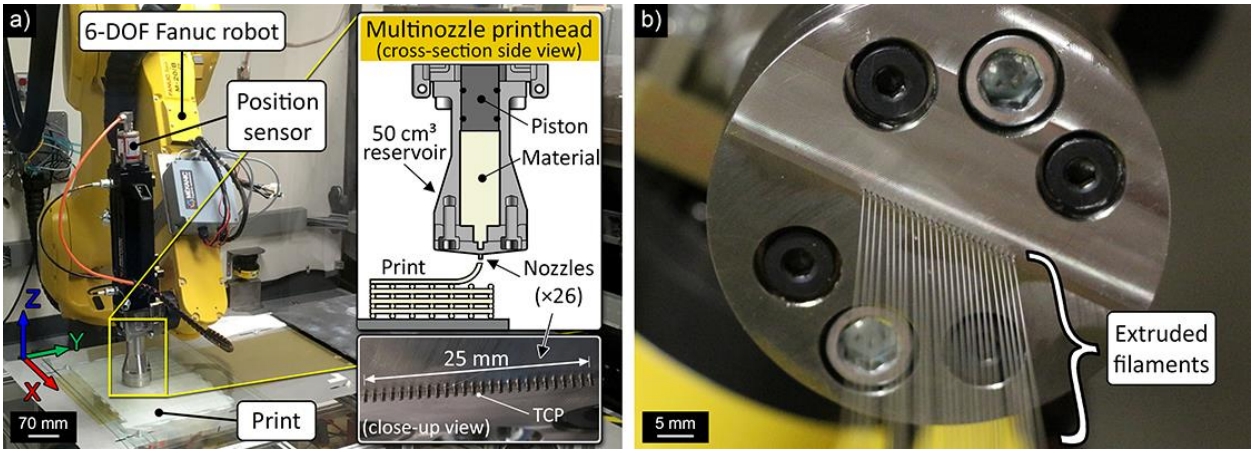

Figure 4.1. 6-DOF robotic AM infrastructure. a) The material contained in the 50 cm³ reservoir is pushed by a piston at required pressure through an array of 26 cylindrical nozzles (D = 250 µm, L = 6.5 mm). The piston's course is monitored via a position sensor, which allows accurate pressure setting in order to keep the extrusion flow rate constant. The tool center point (TCP) is located at the center of the nozzle array. b) Close-up view of the multinozzle printhead showing the vertical extrusion of the material through the nozzle array.

4.2.2 Material preparation

An organic paste-like material (referred as organic ink) developed in [115] was selected because of its low viscosity, shear-thinning behavior, and shape retention at room temperature. The organic ink was prepared according to the method found in [115] using a ratio of 40 wt.% microcrystalline wax (SP-18, Strahl & Pitsch, West Babylon, NY, USA) and 60 wt.% petroleum jelly (Vaseline, Unilever, Canada). The mixture was melted (at ~ 80 °C) and mixed by magnetic stirring for 20 min. The hot ink was then poured directly from a beaker into the 50 cm³ reservoir of the multinozzle printhead and cooled at room temperature after 90 min. The reservoir was closed by inserting the piston in the reservoir chamber inlet using a perforated screw on the piston to let the air escape. The perforated screw was then replaced by an airtight screw to seal the piston-reservoir assembly. Finally, the ink-filled piston-reservoir assembly was mounted on the upper part of the printhead, already fixed on the robot.

4.2.3 Design and multinozzle AM of microscaffold networks

The proposed multinozzle AM technique is used for the manufacturing of large networks of interconnected microscaffolds. The method is demonstrated using four different multinozzle AM case studies: High-speed printing of microscaffold network, variable pore size microscaffold network, large-scale partitioned microscaffold network, and thick partitioned microscaffold network. Figure 4.2 schematically presents an isometric view of a typical partitioned microscaffold network of N layers. Microscaffolds (in blue) are as wide as the width of the printhead nozzle array (~ 25 mm) and are printed in an ordered configuration of i rows × j columns over several layers, in order to generate a periodic structure of interconnected microscaffolds, referred as the network. Detail A shows that each microscaffold can be partitioned by a separation wall obtained by offsetting the 3D printing toolpath. The separation wall width is expected to be equal to the diameter of a filament d. However, filaments of the wall appear to have an imperfect non-circular shape as presented in the case study (see Section 4.4.3.3). These walls are intended to separate the volume of air occupied inside each of the microscaffolds, which could be useful for some applications. In Detail B, the top view of a microscaffold presents the resulting pore size p (defined as the air gap between filaments from the top view) equal to 750 µm when d = 250 µm (shown in Detail C). As seen in Detail C, p depends on the center-to-center spacing s (1 mm), between each nozzle, but also the printhead orientation around its axis with respect to the printing direction (see Section 4.4.3.2). Thus, as shown in Detail D, the toolpath offset must be equal to s to perfectly align the filaments of each microscaffold and each wall (in red). This pattern leads to each microscaffold being a square shape of ~ 26 mm × 26 mm wide, which corresponds to the total printing width for all 26 filaments (~ 25 mm) in addition to a 1 mm offset to generate the partition walls.

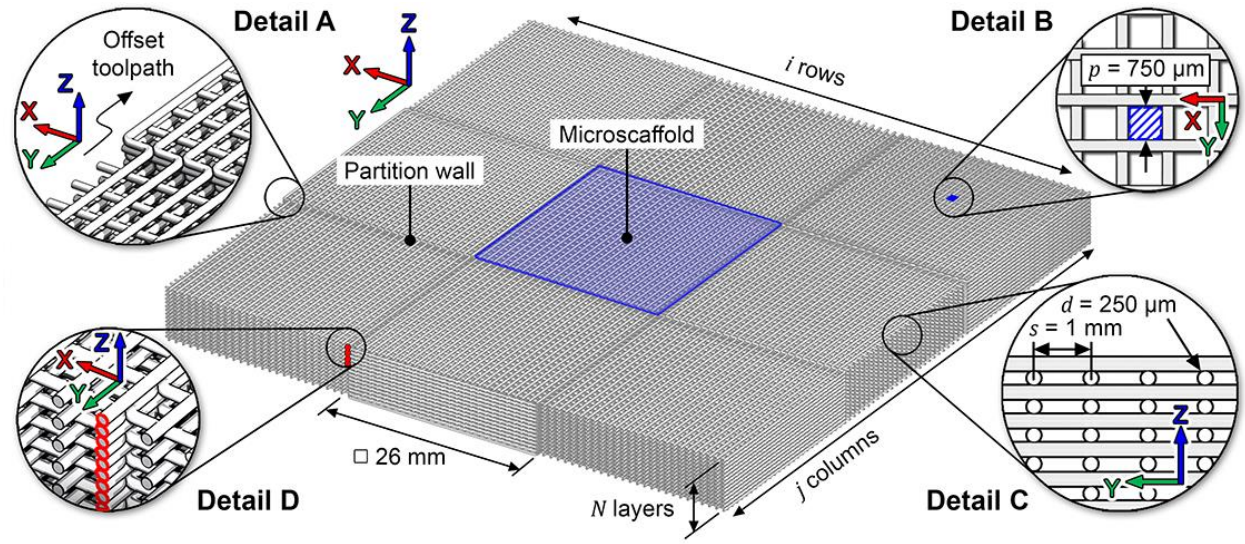

Figure 4.2. Isometric view of a typical partitioned microscaffold network ($i \times j$ configuration, N number of layers). Detail A: view of a partition wall made by an offset toolpath. Detail B: top view of the pore size p = 750 µm (in blue). Detail C: side view of the filaments center-to-center spacing s = 1 mm and nominal filament diameter d = 250 µm. Detail D: Cross-sectional view of the filaments stacking in a wall (in red).

The first step in the AM of a typical microscaffold network consists of generating the toolpath using a custom Python script. The printing speed is programmed from 50 to 250 mm/s and the flow rate is maintained constant via the hydraulic pressure system of the robotic AM infrastructure. The flow rate is continuous from the start up to the end of the deposition. A simple $i \times j$ configuration network of straight parallel filaments is generated following the X axis direction in order to realize the first layer of the microscaffold network. Then, the printhead rotates at 90° on its Z axis, moves at the beginning of the next layer and is offset in the $+Z$ axis direction of the planar printing surface before printing a second filament network to obtain an $i \times j$ partitioned microscaffold network of 2 layers with perpendicular filaments on top of each other. When changing layers or positioning for the next row or column, the toolpath is slightly cleared of the part to prevent any overlapping of filaments on the manufactured part. The $+Z$ offset is set to 85 % of d, as mentioned in [148], to facilitate the contact between the filaments of the stacked layers. At the end of the second layer, a rotation in the opposite direction to the one of the previous layer is performed on the printhead's Z axis, and the remaining layers are printed in the same fashion as the previous layers. The second step is to convert the toolpath to a proprietary file for Fanuc robots using the software RoboDK's

built-in post-processor and then export it into the robot controller. The multinozzle TCP's and the printing surface's reference frame were calibrated using the 3-point method [77]. Finally, the program is launched via the 6-DOF robotic AM infrastructure to allow the fabrication of a microscaffold network.

4.2.4 Characterization of printed microscaffold networks

The printed microscaffold networks are characterized and analyzed using a stereo microscope (Olympus SZX12, Olympus Corporation, Japan) with software Image Pro Plus (version 7.1) to measure the resulting printed filament diameter and pore size. The robot TCP position, motion speed and printing time are recorded using Labview (2018, National Instrument) with the DigiMetrix Robotics Library for Fanuc (DigiMetrix GmbH, Germany). Since the organic ink is soft and will not harden, an epoxy encapsulation step is necessary for optical observation of the cross-section and X-ray scan of the network. Using a 10 cm^3 syringe and a 500 µm inner diameter dispensing nozzle (Nordson EFD, USA), an uncured mix of epoxy resin (Epon 862, Miller-Stephenson, USA) and curing agent (Epikure 3274, Miller-Stephenson, USA) is slowly infiltrated in the network of Case study #4 and cured at room temperature for 48 h in a plastic mold. The encapsulated network is scanned with an X-ray micro computer tomography scanner (Xradia 520 versa, Zeiss Canada, Canada) at an acceleration voltage of 50 kV (power of 4 W), an objective of 0.4× (field of view of 35 mm) and a voxel size of 34 µm. A total of 4500 projections were recorded at an exposure time of 14 s per scan over a measurement duration of 15 h. The 3D scans are analyzed using the software Paraview (version 5.9.0-RC1).

4.3 Multinozzle Extrusion Prediction Model (MEPM)

4.3.1 Model development

An analytical Multinozzle Extrusion Prediction Model (MEPM) was developed and programmed using Matlab to predict the required applied pressure gradient for the multinozzle extrusion process and its resulting total flow rate as a function of the printhead's geometry, material used and desired printing speed v. The material is assumed to be incompressible, to be extruded at steady-state and fully developed flow, and the effects of time and temperature on the material's viscosity are not considered. Swelling and nozzle wall slip are also not considered. The nozzles are considered

perfectly cylindrical and their length L is considered identical. The pressure gradient is first calculated with an average nozzle diameter to match the programming of the printing-speed-driven pressure controller. Then, using the pressure gradient, volumetric flow rates are recalculated iteratively at each nozzle to reflect geometrical discrepancies between nozzles.

4.3.1.1 Pressure gradient calculation

The MEPM is based on a similar method proposed by Bruneaux et al. [40] for the applied pressure gradient calculation. The printing speed is considered to be an average velocity at the outlet of all α nozzles, where α is the number of nozzles of the multinozzle printhead. The multinozzle printhead geometry is first defined by measuring the nozzles inner diameter D_{i} with a stereo microscope (Olympus SZX12, Olympus Corporation, Tokyo, Japan) and software Image Pro Plus (version 7.1). The average nozzle inner diameter D_{avg} is then calculated using D_{i}. The nozzles geometry is then used with v to estimate the average volumetric flow rate for each nozzle, Q_{i}, using:

$$Q_{\mathrm{i}} = vA_{\mathrm{avg}} \tag{4.1}$$

where A_{avg} is the average area of the nozzles calculated with D_{avg}. Using Q_{i} and D_{avg}, the apparent shear rate inside each nozzle for non-Newtonian fluids, $\dot{\gamma}_{\mathrm{i}}$, is given as:

$$\dot{\gamma}_{\mathrm{i}} = \frac{32Q_{\mathrm{i}}}{\pi D_{\mathrm{avg}}^{3}}\left(\frac{3+1/n}{4}\right) \text{ [38]} \tag{4.2}$$

where the term in parenthesis is the Weissenberg–Rabinowitsch correction and n is the material's flow behavior index for a fluid whose viscosity behavior follows a power law model. With $\dot{\gamma}_{\mathrm{i}}$, the non-Newtonian viscosity η_{i} is calculated for each nozzle using a power law model, given by:

$$\eta_{\mathrm{i}} = K\dot{\gamma}_{\mathrm{i}}^{\,n-1} \text{ [38]} \tag{4.3}$$

where K is the material's flow consistency index. Each parallel nozzle's flow resistance R_{i} can now be calculated from Hagen-Poiseuille's law for a flow in a pipe and the multinozzle printhead's total equivalent flow resistance R_{eq} is obtained, such as:

$$R_{\mathrm{i}} = \frac{128 L \eta_{\mathrm{i}}}{\pi D_{\mathrm{avg}}^4}\left(\frac{3 + 1/n}{4}\right) \text{ [38]}, \tag{4.4}$$

$$R_{\mathrm{eq}} = \frac{1}{\sum_{\mathrm{i}=1}^{\alpha} \frac{1}{R_{\mathrm{i}}}}. \tag{4.5}$$

Finally, the required applied pressure gradient ΔP is calculated by first summing all Q_{i} to obtain the total volumetric flow rate Q_{tot} and then multiplying to R_{eq} so that:

$$\Delta P = \sum_{\mathrm{i}=1}^{\alpha} Q_{\mathrm{i}} \cdot R_{\mathrm{eq}} = Q_{\mathrm{tot}} R_{\mathrm{eq}} \text{ [38]}. \tag{4.6}$$

When all nozzles have the same geometry, the total equivalent flow resistance, given by Equation (4.5), equals to R_{i} divided by α, and Q_{tot}, used in Equation (4.6), is equal to Q_{i} multiplied by α. Thus, when ΔP is calculated in Equation (4.6), the terms α cancel each other out (*i.e.*, $\Delta P = Q_{\mathrm{i}} R_{\mathrm{i}}$). Therefore, the calculated pressure for a multinozzle printhead is mathematically the same as for a single nozzle when all nozzles are in a parallel configuration and feature the same geometry. In reality, diametrical variability inherent to the manufacturing of a multinozzle printhead will result in a unique resistance R_{i} and a different flow rate Q_{i} for each nozzle in Equation (4.4). Hence, the flow rates Q_{i} must be recalculated for each nozzle according to the applied pressure calculated in Equation (4.6) and then summed together to obtain the actual Q_{tot}.

4.3.1.2 Total volumetric flow rate calculation

For the total flow rate calculation, the MEPM uses a similar method proposed by Kranz [13]. Since ΔP is uniform at the inlet of each nozzle but the nozzles real inner diameter D_{i} vary from its theoretical value, v cannot be assumed to be the same at the outlet of each nozzle. Every nozzle's volumetric flow rate Q_{i} is no longer an average and is recalculated. Q_{i} depends on ΔP and ΔP depends on η_{i}. Every Q_{i} has to be recalculated iteratively, because η_{i} depends on $\dot{\gamma}_{\mathrm{i}}$ (and therefore Q_{i}). For each nozzle, Q_{i} is used as a first guess $Q_{\mathrm{i,guess}}$. Then, using $Q_{\mathrm{i,guess}}$ and the experimentally measured D_{i} in Equation (4.2), a new $\dot{\gamma}_{\mathrm{i}}$ is calculated and reinserted into Equation (4.3) to obtain η_{i}. Each nozzle's flow resistance R_{i} is recalculated using D_{i} in Equation (4.4). R_{i} is used directly with the previously calculated ΔP to obtain a new flow rate for each nozzle, given by:

$$Q_{\mathrm{i,new}} = \Delta P / R_{\mathrm{i}} \,. \tag{4.7}$$

Convergence is verified between the new flow rate $Q_{\mathrm{i,new}}$ and the first $Q_{\mathrm{i,guess}}$, using:

$$\Delta Q_{\mathrm{i}} = \frac{\left| Q_{\mathrm{i,new}} - Q_{\mathrm{i,guess}} \right|}{Q_{\mathrm{i,guess}}} < 10^{-4}. \tag{4.8}$$

If the variation ΔQ_{i} does not meet the convergence condition (reported in [13]), the new flow rate $Q_{\mathrm{i,new}}$ becomes the new $Q_{\mathrm{i,guess}}$ and is reinserted into Equation (4.2) for another cycle until ΔQ_{i} becomes smaller than the convergence condition. Once the iterative process converges for all nozzles, each $Q_{\mathrm{i,new}}$ is summed to obtain the new total volumetric flow rate Q_{tot} (see individual flow rates comparison in supplementary Figure 4.10).

4.3.2 Model comparison with results from the literature

Extrusion pressures as a function of the printing speed are extracted for two materials taken from the literature to compare with the MEPM predictions. Using the extracted viscosity data (n and K parameters) from [40], the MEPM is used with the reported single nozzle geometry (α = 1, D = 510 µm, L = 18.87 mm) for the organic ink developed in [115] using the reported printing speed range of 0 to ~ 45 mm/s. Using the viscosity data (n and K parameters) from [26], the MEPM is used with the reported single nozzle geometry (α = 1, D = 200 µm, L = 12.24 mm) for dissolved polylactide acid (PLA) ink used in Solvent-Cast 3D printing using the reported printing speed range of 0 to ~ 26 mm/s.

4.3.3 Multinozzle data acquisition and extrusion prediction

Using a custom data-acquisition interface programmed in Labview (2018, National Instrument), the multinozzle printhead applied pressure gradient is recorded for printing speed setpoints of v = 50, 100, 150, 200 and 250 mm/s using the organic ink. The maximum reachable printing speed is 250 mm/s due to the maximum displacement speed of the piston pushing the ink. The recorded pressure gradients are compared to the pressure predicted by the MEPM using a power law viscosity model with n = 0.468 and K = 604 Pa·s^{n} (see viscosity profile in supplementary Figure 4.11), a multinozzle configuration of α = 26, L = 6.5 mm, and the measured nozzles inner diameter

D_{i}. For experiments at printing speed of 50 and 250 mm/s, the total mass of the microscaffold networks is weighed using a precision scale (EP6501 Explorer Pro, Ohaus Corporation, USA). For experiments at printing speed of 100, 150 and 200 mm/s, the organic ink is extruded in a beaker. No specific geometries were printed, and the extruded ink collected in the beaker was weighed using the same precision scale. The overall mass flow rate is calculated by dividing the total mass of extruded material over the printing time and then converted to the overall volumetric flow rate Q_{exp} by dividing the estimated organic ink density (estimated using the material components datasheet and ink composition, see Q_{exp} calculation steps in supplementary Table 4.2). The overall volumetric flow rate Q_{exp} is then compared to Q_{tot}, predicted by the MEPM using the organic ink's rheological properties and the nozzles geometry.

4.4 Results and discussion

4.4.1 Design exploration of multinozzle configurations

The MEPM could be used to explore different multinozzle configurations. Figure 4.3a shows a log-log chart of the applied pressure prediction as a function of the printing speed for four multinozzle configurations of α = 26 nozzles with different inner diameter (D = [100, 250, 500, 750] µm and L = 6.5 mm). Figure 4.3b shows a log-log chart of the total volumetric flow rate prediction for the same four multinozzle configurations as in Figure 4.3a as a function of the printing speed. Figure 4.3c shows a log-log chart of the total volumetric flow rate prediction as a function of the printing speed for five multinozzle configurations with different number of nozzles (α = [1, 4, 10, 26, 50], D = 250 µm, L = 6.5 mm). With the established maximum displacement speed of the piston, the maximum printing speed v_{max} is calculated for each configuration by assuming mass conservation through all nozzles and the MEPM is used to compute the applied pressure gradient ΔP and total volumetric flow rate Q_{tot} for v = 0 mm/s to v_{max} for each configuration.

4.4.1.1 Effect of nozzles inner diameter

Reducing the nozzles inner diameter increases the required applied pressure, which also increases the reachable v_{max}. Using the current hydraulic pressure controller with 26 nozzles of D = 100 µm, v_{max} would be reached at 1562 mm/s at a pressure of 42.9 MPa for the organic ink, which is under

the maximum allowable pressure $P_{\max}$ = 65 MPa. Larger nozzles diameter, such as D = 500 µm and D = 750 µm, require a lower ΔP but at the cost of smaller $v_{\max}$ (*i.e.*, < 100 mm/s) and printing precision. For every nozzle diameter scenario, a maximum Q_{tot} of 319 mm³/s can be achieved at different values of $v_{\max}$ with the current pressure controller. For a fixed Q_{tot}, reducing D increases $v_{\max}$. For a fixed printing speed, the use of larger nozzles increases the flow rate while smaller nozzles reduce it.

4.4.1.2 Effect of the number of nozzles in parallel

For any given printing speed, the flow rate is directly proportional to α, and the applied pressure is the same regardless of the number of nozzles (see Section 4.3.1.1). The flow rate is linearly dependent on the printing speed. Using a single nozzle (α = 1), the theoretical maximum printing speed is equal to 6500 mm/s for the maximum reachable Q_{tot} = 319 mm³/s (with ΔP = 21.8 MPa). The necessity to match the 6-axis robot tool movement speed in this work limits $v_{\max}$ to $v_{\max,\text{robot}}$ = 2000 mm/s. The number of nozzles with D = 250 µm that a multinozzle printhead must contain to tend toward this printing speed limit while reaching the maximum Q_{tot} = 319 mm³/s is α = 4 ($v_{\max}$ = 1625 mm/s, ΔP = 11.5 MPa). Such a high speed might be unattainable for short distance printing, as the 6-axis robot has to consider the weight of the multinozzle printhead during acceleration and deceleration [98]. On the opposite side of the chart, the use of 50 nozzles would reduce $v_{\max}$ down to 130 mm/s and ΔP to 3.6 MPa. The manufacturing of a multinozzle printhead containing a high number of nozzles is more likely to cause more geometrical disparities between them.

4.4.1.3 Current multinozzle configuration

The current multinozzle configuration is shown in red on Figure 4.3. A compromise of α = 26 nozzles at D = 250 µm was deemed appropriate for the AM of microscaffold networks presented in this work, allowing a Q_{tot} of 319 mm³/s at $v_{\max}$ = 250 mm/s, requiring a maximum ΔP = 4.8 MPa using organic ink. The current multinozzle configuration is suitable for manufacturing the small features (*i.e.*, filaments, pore size and wall) of the microscaffold structures in this work.

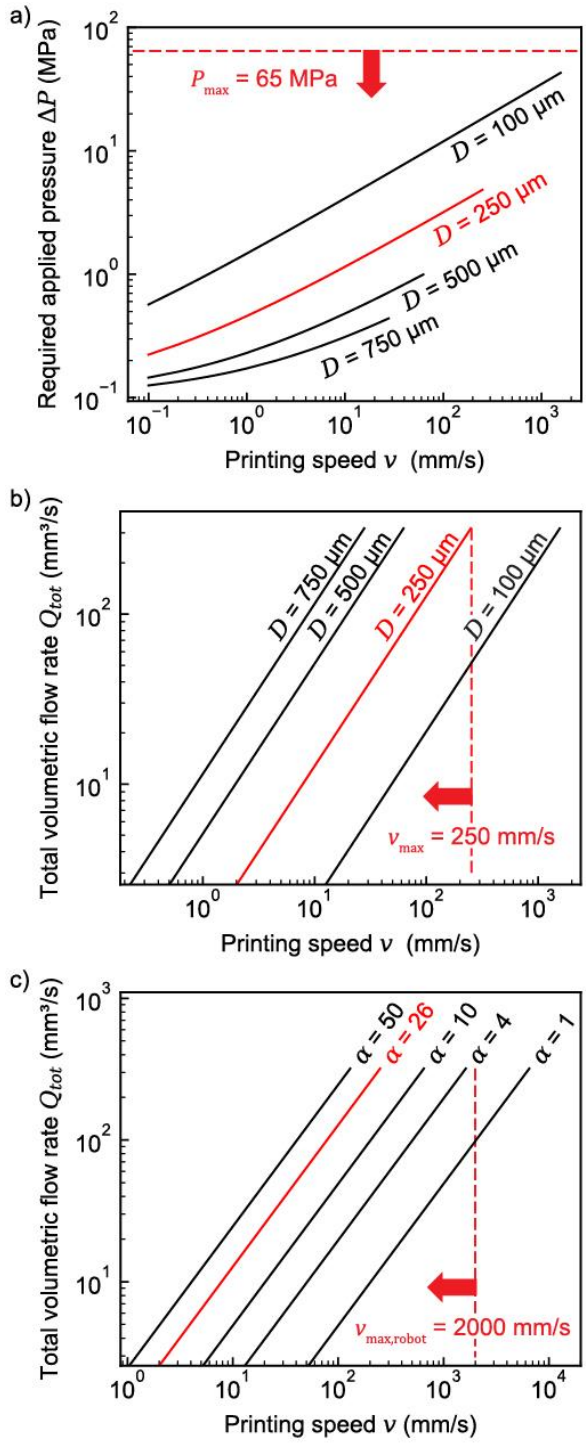

Figure 4.3. Multinozzle extrusion prediction modeling charts for organic ink. The current infrastructure parameters are shown in red. a) Applied pressure prediction for four multinozzle configurations with different nozzles inner diameter (α = 26, D = [100, 250, 500, 750] μm, L =

6.5 mm). The maximum extrusion pressure (65 MPa) is not reached with the use of organic ink (red dotted line). b) Total volumetric flow rate prediction for four multinozzle configurations with different nozzles inner diameter (α = 26, D = [100, 250, 500, 750] µm, L = 6.5 mm). The maximum reachable printing speed for the configuration used in this work (D = 250 µm) is 250 mm/s due to the printhead maximum piston displacement speed. c) Total volumetric flow rate prediction for five multinozzle configurations with different number of nozzles (α = [1, 4, 10, 26, 50], D = 250 µm, L = 6.5 mm). The 6-axis robot maximum tool movement speed limits the printing speed at 2000 mm/s.

4.4.2 Prediction of single and multinozzle extrusions

4.4.2.1 Model comparison using single nozzle configuration

Figure 4.4a presents the applied pressure gradient calculated using the MEPM as a function of the printing speeds, single nozzle geometries and rheological data reported in [26], [40]. Experimental values from [26], [40] were plotted on the same graph and compared with the predictions from the MEPM. Predictions for the organic ink used in [40] show a mean absolute error (MAE) of ~ 0.045 MPa (mean relative error (MRE) of 3.5 %) with the authors' results for all printing speeds. Similarly, the predictions for dissolved PLA ink [26] exhibit a slightly higher ΔP to allow extrusion at the given printing speeds, with a MAE ~ 0.075 MPa and MRE of 10.8 %. The printing speeds reported by the authors are estimated by measuring the extruded filaments diameter following the application of a known pressure gradient (following the method explained in [40]). Inversely, the printing speeds used in the MEPM are known, and the pressures are measured. Both calculation methods introduce different effect from the experimental errors, which could explain the errors between the predictions and the authors results. The MEPM works as intended for single nozzle geometries and is suitable to predict the applied pressure, at any printing speed, of a wide range of non-Newtonian fluids.

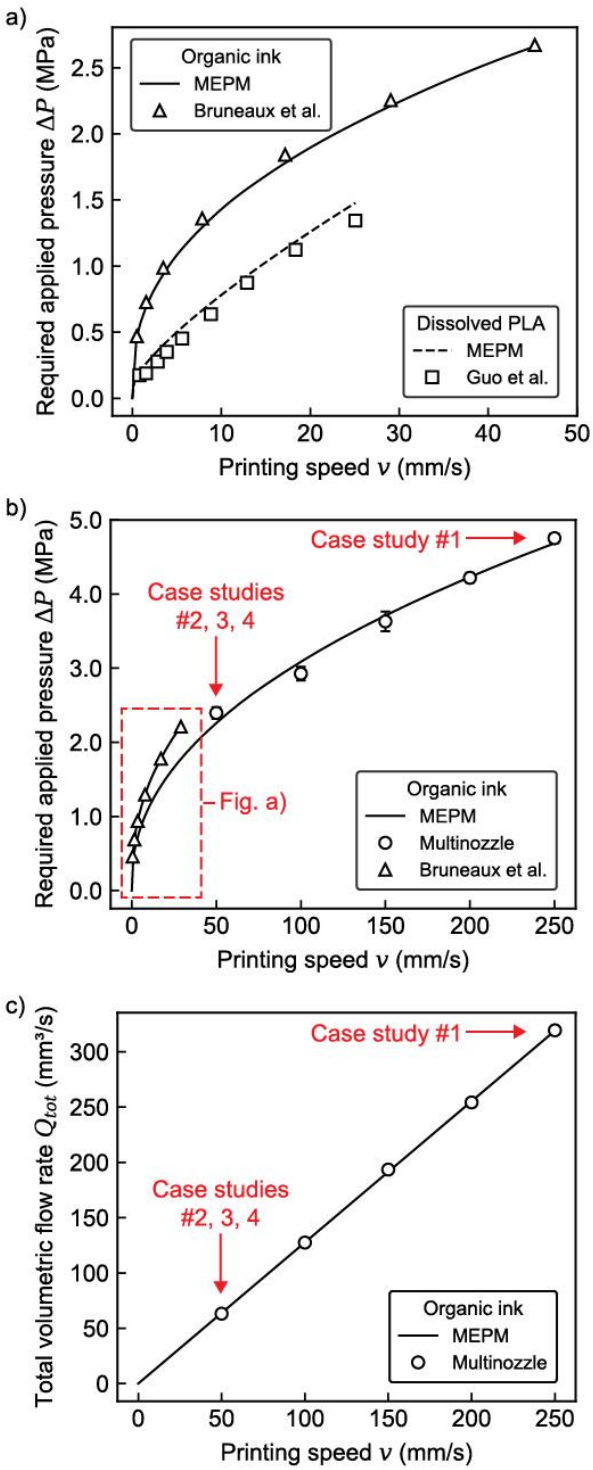

Figure 4.4. a) Comparison of the MEPM and experimental values from the literature for single cylindrical nozzle extrusion (α = 1, D = 510 µm, L = 18.87 mm) of organic ink (60/40 wt.%) [40] and single cylindrical nozzle extrusion (α = 1, D = 200 µm, L = 12.24 mm) of dissolved Polylactic

Acid (PLA, 20 wt.%) for solvent-cast 3D printing [26]. b) Applied pressure prediction and experimental results for multinozzle (cylindrical, α = 26, D = 250 µm, L = 6.5 mm) extrusion of organic ink at v = 50, 100, 150, 200 and 250 mm/s. Error bars represent the 95 % confidence interval. c) Total volumetric flow rate prediction and experimental results from the experiments in b).

4.4.2.2 Applied pressure prediction using multinozzle configuration

Figure 4.4b shows the MEPM predictions and experimental measurements of the applied pressure gradient as a function of the printing speed and multinozzle geometry (D_{avg} = 255 µm) for the extrusion of the organic ink. The maximum printing speed of 250 mm/s requires a constant applied pressure of 4.75 MPa (standard deviation σ = 0.05 MPa), at which Case study #1 was manufactured (see Section 4.4.3). The printing speed was reduced to 50 mm/s and Case study #2, #3 and #4 were manufactured with a constant applied pressure of 2.40 MPa (σ = 0.07 MPa). Printing speeds of 100 mm/s (2.93 MPa, σ = 0.08 MPa), 150 mm/s (3.63 MPa, σ = 0.12 MPa) and 200 mm/s (4.22 MPa, σ = 0.06 MPa) were also investigated. The reported values represent the average pressure recorded over several experiments and the error bars represent the 95 % confidence interval of each printing speed. Values of Figure 4.4a are superimposed on top of the plot for comparison between single nozzle and multinozzle. Pressures reported by Bruneaux et al. [40] and calculated using the MEPM are coherent with measured and predicted pressures of the multinozzle printhead. Pressures in the domain of Figure 4.4a (*i.e.*, 0 to ~ 50 mm/s) are slightly higher than the predicted pressures in the same domain of Figure 4.4b. The applied pressure for a single nozzle should mathematically be the same as the applied pressure for a multinozzle if all nozzles share the same inner diameter and length as the single nozzle. For the same material, the power law viscosity parameters n and K must be identical. Thus, the shift between the two organic ink curves could be explained by geometrical differences between the single nozzle and multinozzle, but mostly by the approximation of the authors' actual material viscosity estimated by n and K. These parameters are directly proportional to the pressure calculation and are different in both cases. The MEPM is therefore able to predict the required pressure to allow extrusion of organic ink for any given printing speed.

4.4.2.3 Total volumetric flow rate prediction using multinozzle configuration

Figure 4.4c shows the predictions and the experimental measurements of the total volumetric flow rate for the experiments presented in Figure 4.4b. At a printing speed of 250 mm/s, an overall total volumetric flow rate Q_{tot} ~ 319.4 mm³/s (σ = 2.3 mm³/s) is required to manufacture Case study #1. At a printing speed of 50 mm/s, Q_{tot} ~ 63.2 mm³/s (σ = 1.9 mm³/s) is required to manufacture Case study #2, #3 and #4. The experimental results are strongly aligned with the MEPM predictions for v = 0 to 250 mm/s. The MEPM is therefore able to accurately predict the total volumetric flow rate generated by the extrusion process of the multinozzle printhead.

4.4.3 Case studies: Multinozzle AM of periodic microscaffold networks

4.4.3.1 Case study #1: High-speed printing of microscaffold network

Figure 4.5 shows a 5-layer microscaffold network (9 × 15 configuration, without partition walls) made of the organic ink. The target printing speed v = 250 mm/s is set in order to print at maximum flow rate Q_{tot} ~ 319.4 mm³/s at an applied pressure of 4.75 MPa (see Sections 4.4.2.2 and 4.4.2.3). Figure 4.5a shows a top view of the entire printed microscaffold network. The scalebar represents the total printing width of a typical microscaffold (*i.e.*, 26 mm). The result is one large 225 mm × 375 mm × 1 mm microscaffold network composed of 234 × 390 filaments wide, that weighs approximately 27.7 g in total, and requires approximately 1 minute 36 seconds to manufacture (see supplementary Video 4.1). Assuming the same geometrical specifications, dimensions, and extruded mass, printing this microscaffold network using a single nozzle (with D = 250 µm and L = 6.5 mm) would take ~ 41 minutes (for α = 1, v_{max} = 250 mm/s and Q_{tot} ~ 12.3 mm³/s, see Figure 4.3c). Figure 4.5b presents a close-up top view of the overall network. The structure is composed of smooth parallel lines, which are perpendicularly overlapped and connected between layers. Figure 4.5c presents a ×25 magnification image, where the average measured filaments diameter $\bar{d}$ is 255 µm (σ = 15 µm, d_{theo} = 250 µm) and the average pore size $\bar{p}$ is 736 µm (σ = 21 µm, p_{theo} = 750 µm).

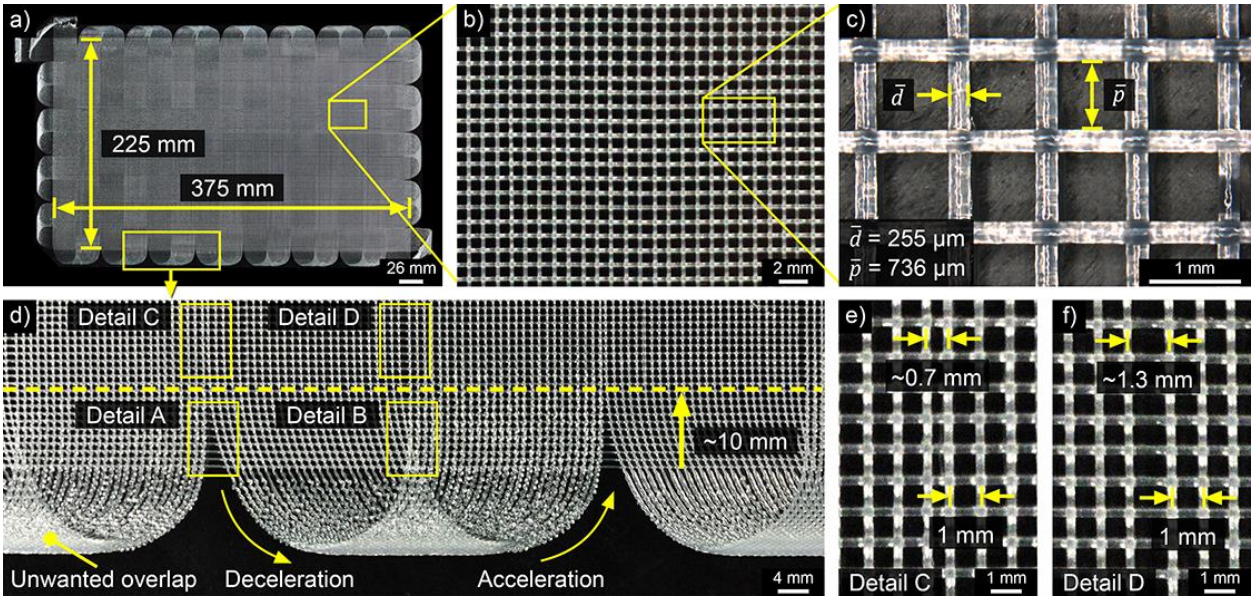

Figure 4.5. 5-layer microscaffold network (9 × 15 configuration) printed at 250 mm/s (~ 1 min 36 s) for a total of 234 × 390 filaments wide. a) Top view of the entire print. b) Close-up top view of the microscaffold network. c) ×25 magnification image of the microscaffold filament stacking showing the average filaments diameter $\bar{d}$ = 255 µm and average pore size $\bar{p}$ = 736 µm. d) Close-up view of the transition between two columns displaying a toolpath rounding, which reduces the microscaffold network size by 10 mm. Focus on details of print defects A, B, C and D. e-f) Close-up views of the spacing between printed columns (Details C, D).

Figure 4.5d shows a close-up view of a transition between columns, where the printhead's position must be laterally shifted for the next column deposition. Due to the incapacity of the printhead to momentarily stop the extrusion before printing the next row or column, a toolpath clearance is required to avoid overlapping filaments on the network. To perform the toolpath clearance, the robot must reach a point coordinate outside of the network. Then, to print the next row or column, the robot has to shift its position and go the opposite direction with respect to the last printed direction. Although the robot is programmed to reach the target motion speed of 250 mm/s, maintaining this speed is difficult when the printhead changes direction. For a sharp turn (≤ 90°), the kinematic model of the robot forces the printhead TCP to slow down and round the toolpath before accelerating again [149]. In the process, the printhead rotation does not change and some filaments overlap each others, creating unwanted overlap features around the network. Moreover, by rounding the toolpath when slowing down from v = 250 mm/s, the robot engages the curve too

early which jeopardizes the filament stacking of the microscaffold network (Details A and B). Ruining the perpendicularity of the filaments stacking reduces the overall network dimensions by approximately 10 mm on each side (see the dotted line). The pores size in Details A and B are also affected because of the changing angle between the multinozzle orientation with respect to its printing direction. Shifting the robot's position also causes a positioning error from one column to another (Detail C and D). Figure 4.5e shows a close-up on Detail C, where the spacing between two printed columns is ~ 0.7 mm and Figure 4.5f shows a close-up on Detail D, where the spacing is now ~ 1.3 mm. It appears that the position of the TCP is shifted by 0.3 mm between rows and columns. The shift of the TCP position seems to be repeated throughout the microscaffold network and is possibly due to the weight of the multinozzle (18 kg), which is closed to the maximum payload capacity (25 kg). A toolpath compensation could be programmed to adjust the TCP position.

Case study #1 demonstrates the possibility of high-speed AM ($v_{\max}$ = 250 mm/s) of a large, structured microscaffold network (225 mm × 375 mm ≈ 8.4 × 10^4 mm²) at a flow rate of Q_{tot} ~ 319.4 mm³/s, with an applied pressure of 4.75 MPa. In [13], a multinozzle with 64 smaller rectangular nozzles of 200 µm × 200 µm was used to manufacture a very similar, but larger 4-layer microscaffold (3.8 × 10^5 mm²) made of the same organic ink at a slower printing speed $v_{\max}$ = 40 mm/s and a lower flow rate Q_{tot} ~ 102 mm³/s (with a higher pressure of 5.17 MPa). The printed area is ~ 4.5 times larger, one layer less, required 25 minutes to print and was printed with smaller nozzles. By comparing with the maximum flow rate of the current multinozzle, a similar microscaffold could theoretically be printed in 8 minutes (~ 3 times faster) with the proposed method and custom infrastructure.

4.4.3.2 Case study #2: Variable pore size microscaffold network

Figure 4.6 shows a 2-layer microscaffold network (3 × 5 configuration) made of the organic ink with variable pore size on its second layer. The target printing speed is set to v = 50 mm/s (Q_{tot} ~ 63.2 mm³/s) at an applied pressure of 2.4 MPa. Figure 4.6a shows the printing of the entire microscaffold network (see supplementary Video 4.2). The pore size on the second layer is controlled by rotating the multinozzle printhead around its Z axis. The angle θ at which the printhead is rotated is the angle between the multinozzle array orientation and the X axis,

perpendicular to the printing direction (Y axis). The angle θ is gradually increased for each column of the second layer from 0° to 30°, 45°, 60° and 75.5°, respectively. Figure 4.6b shows four ×25 magnification images of the microscaffold at θ = 30°, 45°, 60° and 75.5°. The average experimental pore size $\bar{p}$ decreases while θ increases, until θ reaches 75.5°, at which point the filaments appear to be printed side by side with no spacing between them. The theoretical pore size p_{theo} can be calculated by:

$$p_{\text{theo}} = s \cdot \cos\theta - d. \tag{4.9}$$

With the current multinozzle configuration, angle θ = 75.5° is the theoretical maximum angle at which the printhead can be rotated to print the filaments side by side with p_{theo} = 0 µm. Table 4.1 presents a comparison between p_{theo} and experimentally measured $\bar{p}$ from Figure 4.6b. For each angle, p_{theo} is calculated using Equation (4.9) by assuming s = 1000 µm and d = 250 µm (the swelling of the material exiting the nozzle is neglected here, *i.e.*, d = D = 250 µm). The experimental values $\bar{p}$ represent an average of several pore measurements for each angle on three prints. The value $\bar{p}$ = 736 µm is taken directly from Case study #1 and validated with Case study #2 for θ = 0° (not shown on Figure 4.6b). For each angle, the MAE and MRE are reported. All values of $\bar{p}$ are smaller than p_{theo}, which could be explained by the small swelling of filaments at nozzle exit ($\bar{d}$ increases by ~ 4 % of the nozzle diameter D). The errors are relatively small (≤ 7 %), which is satisfactory for the variable pore size demonstration.

Table 4.1. Comparison between theoretical and experimentally measured pore size for θ = 0°, 30°, 45°, 60° and 75.5°.

θ (°)	p_{theo} (µm)	$\bar{p}$ (µm)	$\sigma_{\bar{p}}$ (µm)	$\lvert\bar{p} - p_{\text{theo}}\rvert$ (µm)	$\lvert\bar{p} - p_{\text{theo}}\rvert / p_{\text{theo}}$ (%)
0	750	736	21	14	2
30	616	606	9	10	2
45	457	436	10	21	5
60	250	233	10	17	7
75.5	0	0	-	-	-

The average printed filaments diameter $\bar{d}$ is 250 µm (with σ = 1.2 µm) at θ = 75.5° and was obtained by measuring the total printing width of several filaments and by dividing with the total number of measured filaments. Comparison with other measured $\bar{d}$ (for θ = 30°, 45° and 60°) confirms that the printed filaments are well deposited side by side and not on top of each other. Therefore, $\bar{p}$ ~ 0 µm at θ = 75.5°. The results from Case study #2 demonstrate the multinozzle AM of microscaffold networks with variable pore size, which has potential for large-scale microscaffold requiring porosity gradients.

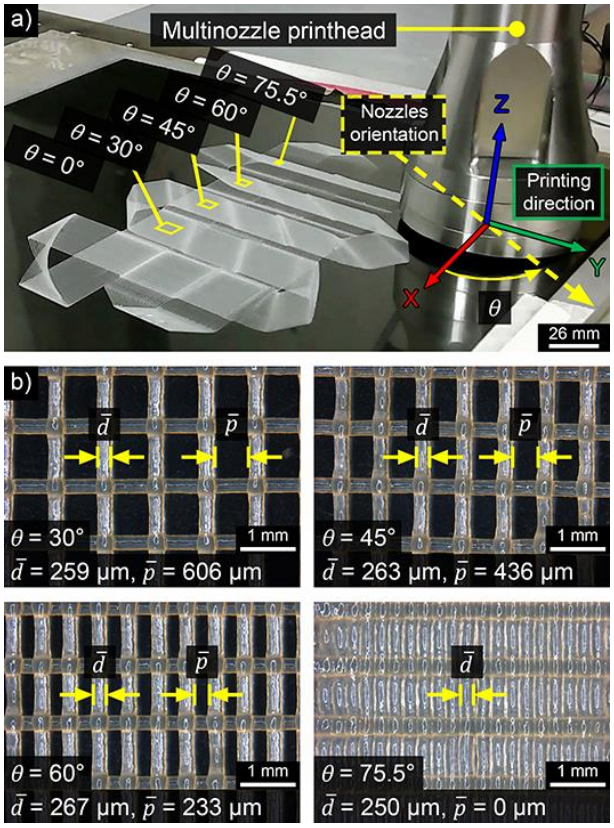

Figure 4.6. 2-layer microscaffold network (3 × 5 configuration) printed at 50 mm/s (~ 30 s) with variable pore size on the second layer. a) General view of the entire print. The nozzles orientation θ is given with respect to the X axis, which is perpendicular to the printing direction (Y axis). The first layer is printed at θ = 0°. The multinozzle is then rotated around its Z axis to increase θ (from 0° to 30°, 45°, 60° and 75.5°) for each column on the second layer. b) ×25 magnification images of the microscaffold filament stacking at θ = 30° ($\bar{d}$ = 259 µm, $\bar{p}$ = 606 µm), θ = 45° ($\bar{d}$ = 263 µm, $\bar{p}$ = 436 µm), θ = 60° ($\bar{d}$ = 267 µm, $\bar{p}$ = 233 µm) and θ = 75.5° ($\bar{d}$ = 250 µm, $\bar{p}$ = 0 µm).

4.4.3.3 Case study #3: Large-scale partitioned microscaffold network

Figure 4.7 shows a 5-layer partitioned microscaffold network (9 × 15 configuration) made of the organic ink. The target printing speed is set to v = 50 mm/s (Q_{tot} ~ 63.2 mm³/s, ΔP = 2.40 MPa) in order to reduce the deceleration required for slowing down at sharp turns. Figure 4.7a shows the entire printed partitioned microscaffold network. The result is a 233 mm × 389 mm × 1 mm network composed of 234 × 390 filaments wide and 135 separated microscaffold partitions, that weighs ~ 30 g in total, and requires approximately 8 minutes 45 seconds to manufacture. Figure 4.7b shows the close-up top view of one of the partitioned microscaffolds of the network. Each microscaffold is a square of 26 mm wide surrounded by walls generated by a programmed toolpath offset. Instead of executing a sharp 90° turn to follow the programmed toolpath offset, the robot slows down, slightly round the corners of the toolpath at the wall coordinates, and travels along a diagonal path while over-extruding at the same time. Partition walls are shared among the neighboring microscaffolds.

Figure 4.7c shows a ×25 magnification image of the top partition wall. Filaments composing the wall have an average width $\overline{w}$ = 847 µm. Over-extrusion leads to a filament with a non-circular cross-section and can be explained by a desynchronization between the robot motion speed and the printing speed. Over-extrusion of all 26 filaments results in an overall partition wall that is almost as wide as s ~ 1 mm. Case study #3 demonstrates the AM of a large interconnected partitioned microscaffold network (233 mm × 389 mm ≈ 9 × 10^4 mm²) in just a few minutes. The addition of partition walls shows that over-extrusion could be exploited to modify the printed filaments diameter, which could be useful for various features of large multi-functional partitioned microscaffold applications.

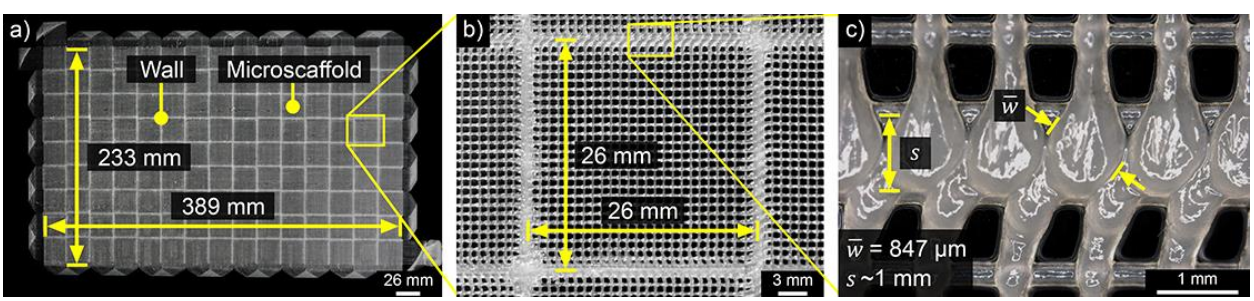

Figure 4.7. 5-layer partitioned microscaffold network (9 × 15 configuration) printed at 50 mm/s (~ 8 min 45 s) for a total of 234 × 390 filaments wide and 135 microscaffold partitions. a) Top view

of the entire print. b) Close-up top view of a partitioned microscaffold. Each microscaffold is a square of 26 mm wide surrounded by walls, made by the offset toolpath. c) ×25 magnification image of a wall. The toolpath offset leads to the robot slowing down, thus leading to over-extrusion and the printing of larger filaments ($\overline{w}$ = 847 µm).

4.4.3.4 Case study #4: Thick partitioned microscaffold network

Figure 4.8 shows a 50-layer partitioned microscaffold network (3 × 3 configuration) made of the organic ink printed at v = 50 mm/s (Q_{tot} ~ 63.2 mm³/s, ΔP = 2.40 MPa). Figure 4.8a shows a general view of the entire printed partitioned microscaffold network. The print is a 77 mm × 77 mm × ~ 10 mm network composed of 78 × 78 filaments wide, that weighs ~ 30 g in total, and requires approximately 8 minutes 45 seconds to manufacture. A total of 50 layers can be achieved with the current material reservoir capacity for this 3 × 3 configuration. Microscaffold cross-sections A-A, B-B and C-C were observed by micro computer tomography to assess the filament stacking quality in the various layers.

Figure 4.8b shows the scanned cross-section A-A. Cross-section A-A consists of the center slice of a microscaffold with partition walls on both sides. Layers of the walls appear to be well stacked on top of each other. All 50 layers of the microscaffold seem well connected to each other via the stacking of perpendicular filaments. Filaments located near walls appear to bend downward, which can be explained by the desynchronization between the robot motion speed and the printing speed, causing over-extrusion.

Figure 4.8c presents cross-sections B-B and C-C, which exhibit the filaments position across layers for a width of 7 filaments wide. Cross-section B-B shows that filaments are well aligned near the center of the microscaffold, with an average horizontal center-to-center filament spacing $\bar{s}$ = 1006 µm (with σ = 57 µm). The microscaffold also appears to slightly collapse on its own weight, as it may be observed by comparing the vertical center-to-center filament spacing z_1 (294 µm) and z_2 (422 µm). Viscoelastic properties of the ink and the large thickness of the microscaffold can explain this behavior, as mentioned in [115]. Cross-section C-C shows that over-extruded filaments near walls are not as well aligned as in the center (B-B). The minimum measured horizontal spacing between filaments is s_1 = 614 µm and the maximum is s_2 = 1449 µm. Despite the misalignment, the average center-to-center filament spacing $\bar{s}$ = 1008 µm (with σ = 150 µm), which is still in line

with the expected geometry. Those printing defects could be minimized by reducing the programmed printing speed, thus reducing the speed difference between the microscaffold center and the wall. It is therefore inevitable that a compromise must be achieved between the AM speed of the network and its quality. Results shown in Case study #4 exhibit the multinozzle AM of a thick periodic partitioned microscaffold network that could prove to be useful for the rapid large-scale manufacturing of any kind of functional structures that requires a high thickness, such as the infill of a 3D-printed part.

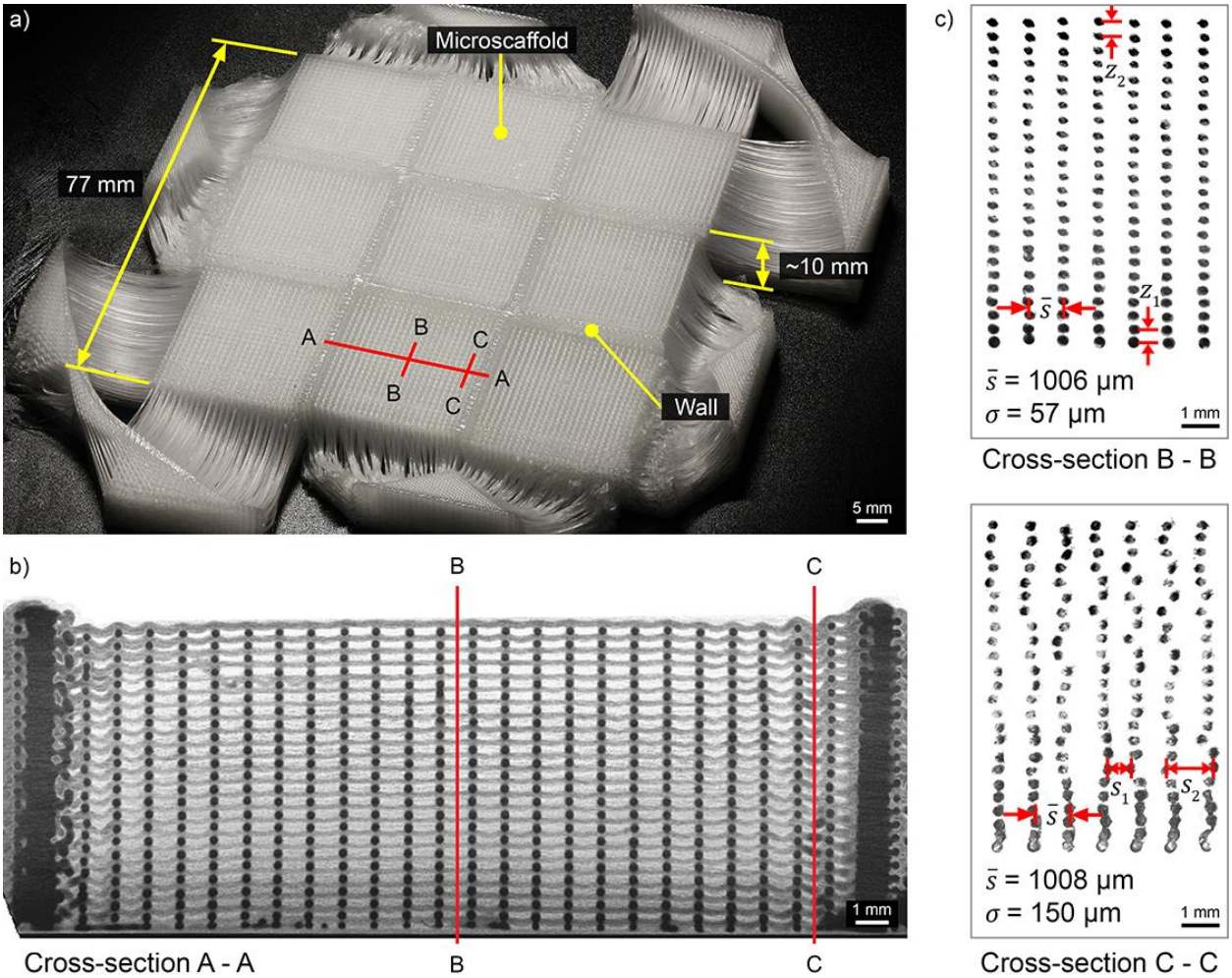

Figure 4.8. 50-layer partitioned microscaffold network (3 × 3 configuration) printed at 50 mm/s (~ 8 min 45s) for a total of 78 × 78 filaments wide and 9 microscaffolds. a) General view of the entire print. Sections A-A, B-B and C-C were observed using an X-ray micro computer tomography scanner. b) Cross-sectional image of the network showing a printed microscaffold between two partition walls (A-A). c) Cross-sectional images of filaments position across layers for a width of

7 in-plane filaments near the microscaffold center (B-B) where $\bar{s}$ = 1006 µm (with σ = 57 µm), and near one of the wall (C-C) where $\bar{s}$ = 1008 µm (with σ = 150 µm). s_1 = 614 µm is the minimum horizontal spacing between filaments and s_2 = 1449 µm is the maximum. Vertical spacing z_1 = 294 µm < z_2 = 422 µm shows the slight collapsing of the microscaffold. Images c) and d) were digitally post-processed to hide the background and improve clarity of the desired features.

4.5 Conclusion

The development of a 6-DOF robotic AM infrastructure equipped with a custom-made multinozzle printhead combined to a high pressure system allowed the high-speed multinozzle AM of relatively large microscaffold networks made of an organic paste-like ink. The multinozzle extrusion process is modeled by developing a Multinozzle Extrusion Prediction Model (MEPM) based on capillary rheometry. Extrusion pressure gradient and volumetric flow rate predictions were made for printing speeds of 50, 100, 150, 200 and 250 mm/s. The MEPM is also used to explore various design configurations of multinozzle printhead. The extrusion ΔP increases as nozzles diameter D decreases or when the number of nozzles α is reduced for a given total volumetric flow rate Q_{tot}, both of which also increase the maximum reachable printing speed v. A configuration of α = 26 nozzles, D = 250 µm and L = 6.5 mm was selected to reach a maximum Q_{tot} ~ 319.4 mm³/s at v_{max} = 250 mm/s. To better control the extrusion process, a prediction of the material's viscosity evolution over time should also be included in the MEPM to monitor the change in pressure required for long duration extrusion, *e.g.*, time dependent curing material systems, such as epoxies.

Four case studies demonstrate the advantages of the high-speed multinozzle AM for large-scale microscaffold networks. Case study #1 showcased the high-speed AM of a large microscaffold network at a printing speed of 250 mm/s, which results in a printing time of ~ 1 min 36 s (vs. ~ 41 minutes for a single nozzle). Case study #2 showed a microscaffold network with variable pore size, which could be beneficial for applications requiring a porosity gradient, *e.g.*, broadband sound absorption [150]. Case study #3 presented a large partitioned microscaffold network. A toolpath offset is sufficient to rapidly produce partition walls that separate all zones within the microscaffold network. These findings could be helpful to quickly print the infill pattern of a hollow 3D-printed part using a functional resin (*e.g.*, epoxy-based polymer) in just a few minutes. Case study #4 displayed a thick 50-layer partitioned microscaffold network, which demonstrated the high quality

of the filament stacking. An average center-to-center spacing of $\bar{s}$ = 1006 µm (σ = 57 µm) at the microscaffold center and $\bar{s}$ = 1008 µm (σ = 150 µm) near walls indicate an excellent filament alignment through the layers. Yet, some extrusion control would be required to limit over-extrusion as much as possible in the transition between the printing of microscaffolds and surrounding walls. The impacts of the current article could also benefit other fields, such as the large-scale multinozzle AM of microvascular networks [151], [152], the high-speed infill of hollow 3D printed parts combined with the Fused Filament Fabrication technique [153] or even the large-scale AM of piezoelectric actuator meshes, similar to microscaffolds networks, for smart materials and structures [154], [155]. The previously mentioned fields could all benefit from the proposed MEPM and multinozzle additive manufacturing workflow by reducing the production time of their additively manufactured parts, potentially allowing cost reduction at the same time. Future work will focus on the non-planar AM of thermosetting-based polymer with the objective of reducing the sound produced by aircraft components [11].

Acknowledgements

The authors acknowledge the collaboration of the company Mëkanic for manufacturing the multinozzle printhead and integration of the robotic cell, the technical assistance of Mr. Benedict Besner for programming the robotic cell data acquisition, of Mr. Benoit Bazin (Safran Composites) for his advice on the industrial robot and Ms. Marie-Hélène Bernier for the X-ray micro computer tomography scans. We also acknowledge the financial support from the FACMO Chair supported by the Natural Sciences and Engineering Research Council of Canada (NSERC, CRDPJ 514761-1), and Safran S.A.

4.6 Supplementary information

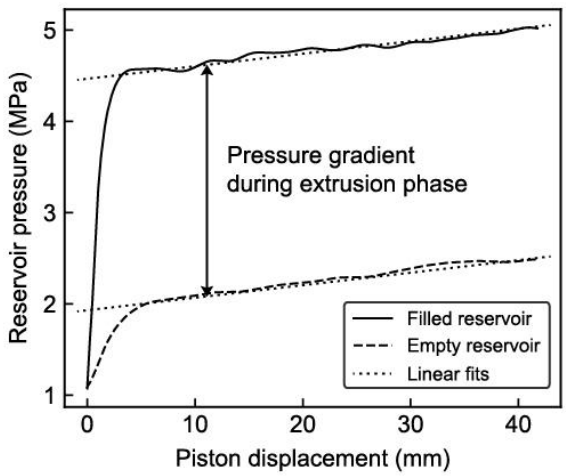

Figure 4.9. Measured pressure inside the multinozzle printhead for the extrusion of organic ink at 50 mm/s printing speed and the measured pressure for the empty reservoir at 50 mm/s printing speed (dry run), with respect to the same piston displacement. During the extrusion phase, the spring is compressed and applies a force on the cross-section area of the piston when the piston moves forward, constantly increasing the pressure in the hydraulic oil. The linear fit slopes exhibit the linear behavior of the spring, according to Hooke's law. The difference between the curves is mainly composed of the pressure gradient during material extrusion. Data was cleaned with a Gaussian filter (with standard deviation σ = 78 kPa).

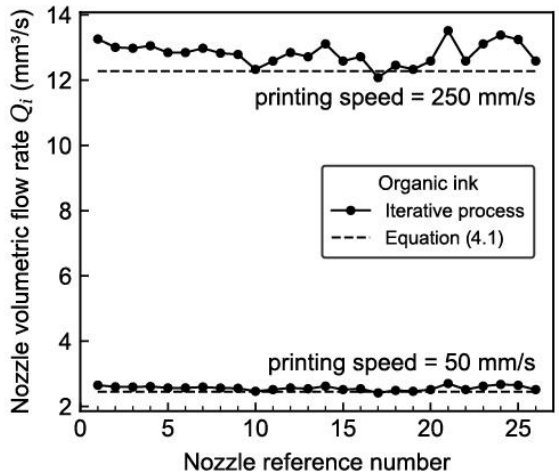

Figure 4.10. MEPM computation for individual nozzle volumetric flow rates using the organic ink at v = 50 and 250 mm/s for each nozzle of the multinozzle printhead. The resulting recalculated individual flow rates (Iterative process, solid line) diverge from to the first flow rate estimates (Equation (4.1), dashed line). The divergence is more significant at 250 mm/s (high printing speed) than at 50 mm/s (moderate printing speed).

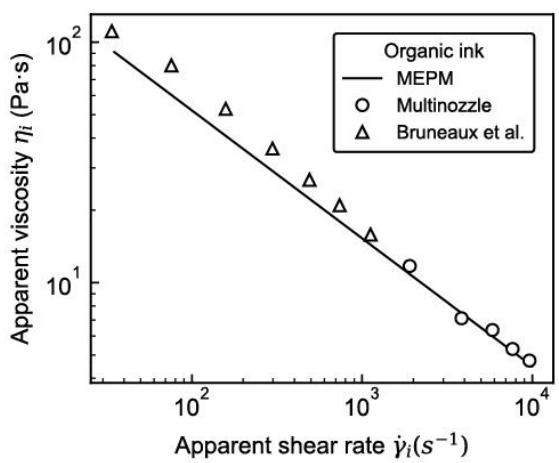

Figure 4.11. Viscosity as a function of the apparent shear rate calculation using the MEPM and experimental measurements for extrusion of organic ink (60/40 wt.%) using the multinozzle printhead (α = 26, D = 250 µm, L = 6.5 mm). Results reported in [40] for single nozzle geometry (α = 1, D = 510 µm, L = 18.87 mm) were superimposed for comparison.

Table 4.2. Experimental volumetric flow rate calculation for printing speed v = 50, 100, 150, 200 and 250 mm/s.

v (mm/s)	Average extruded mass (g)	Average extrusion time (s)	Mass flow rate (g/s)	Volumetric flow rate Q_{exp} (mm³/s)[1]
50	28	500	0.057	63.2
100	31	265	0.115	127.5
150	30	173	0.175	193.5
200	30	131	0.230	254.2
250	31	107	0.289	319.4

[1] Using organic ink density ρ_{ink} = 9.05 × 10^{-4} g/mm³ (estimated using the material components datasheet and ink composition)

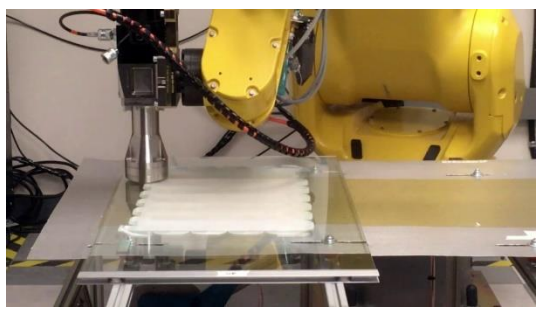

Video 4.1. Case study #1: High-speed additive manufacturing of a large 5-layer microscaffold network (9 × 15 configuration, 225 mm × 375 mm × 1 mm) at 250 mm/s in ~1 minute 36 seconds (available at https://youtu.be/ZkN_StYn4uo).

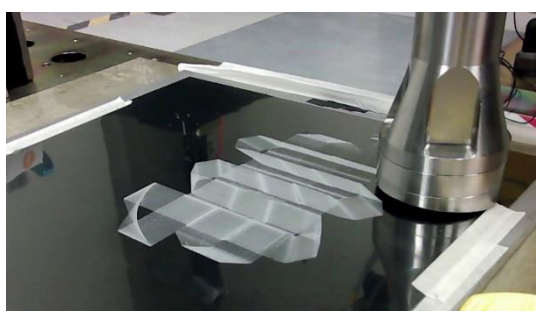

Video 4.2. Case study #2: Multinozzle additive manufacturing of a 2-layer variable pore size microscaffold network (3 × 5 configuration) at 50 mm/s (available at https://youtu.be/xB34lHwUsog).

CHAPTER 5 ARTICLE 2: NON-PLANAR MULTINOZZLE ADDITIVE MANUFACTURING OF THERMOSET COMPOSITE MICROSCAFFOLD NETWORKS

Jean-François Chauvette[1], Iee Lee Hia[1], Rouhollah D. Farahani[1], Raphaël Plante[1], Nicola Piccirelli[2], Daniel Therriault[1]

[1]Laboratory for Multiscale Mechanics (LM[2]), Mechanical engineering department, Polytechnique Montréal, Montréal, Québec H3T 1J4, Canada

[2]Safran Paris Saclay, Centre de R&D et Bureau d'étude, Rue des jeunes bois, Chateaufort - CS80112, 78114 Magny-les-Hameaux, France

Published in Composites Part B: Engineering on February 25, 2023

Abstract

Material extrusion-based non-planar additive manufacturing (AM) using 6-axis industrial robot arms shows great promise for three-dimensional (3D) printing of non-planar parts, despite its typical use of a single large coarse nozzle and high printing time. Here, a non-planar multinozzle AM method capable of achieving high resolution large-scale 3D printing with short printing time using 6-axis robots is reported. A custom Multinozzle Toolpath Generator (MTG), based on non-planar parameterized surface projection, is used to compute the orientation of a multinozzle extrusion array along the curvature of a 3D scanned substrate. The method is demonstrated by the fast 3D printing of large periodic structures (up to an area of ~ 5.2×10^4 mm² within 20 min) consisting of interconnected epoxy composite microscaffolds on a single curvature sinusoidal surface and a double curvature surface of an actual aircraft casing, with an error of 15 µm. The method could be used for AM in various fields such as tissue engineering, microfluidic channels, and porous acoustic coatings of aircraft components.

5.1 Introduction

Non-planar additive manufacturing (AM) can be defined as the process of making parts by joining layers of material made up of non-planar slices of the desired part geometry, as opposed to traditional AM where the material is laid out layer-by-layer on flat and parallel two-dimensional (2D) planes throughout the process [22]. Non-planar AM attempts to overcome some of the main

limitations of extrusion-based AM (*e.g.*, staircase effect, poor bonding of curved features and weak mechanical properties in the thickness direction) [56]. Different approaches have been explored to operate Cartesian three-dimensional (3D) printers (*i.e.*, based on 3-axis movement) in a non-planar way such as cylindrical projection of the machine language (*i.e.*, G-code) generated using a commercial slicer software [156], the combination of planar and non-planar layers using adaptive extrusion methods [60], [62], to completely new framework that automatically generate non-planar G-code using parametric curves without the traditional use of a 3D computer-generated model [67], [68]. In general, the use of a Cartesian 3D printer for non-planar AM is constrained by the geometry of the printhead, which can limit the curvature of non-planar regions of manufactured parts in order to prevent nozzle collision. Therefore, industrial 6-axis robot arms are increasingly used as motion systems for non-planar AM with the potential of producing large-scale parts with more degrees of freedom, allowing for multi-directional printing, easier conformal deposition and AM of overhanging features without the use of supports [82], [83], [93]–[95], [157]. However, one of the main disadvantages of printing large-scale parts composed of small features is the enormous printing time, which can range from several hours up to days depending on the dimensions of the part, material flow rate and size of the nozzle with respect to the size of the part [20], [21].

Multinozzle printheads, *i.e.*, devices capable of material extrusion from more than one nozzle simultaneously, have been developed in an effort to reduce printing time of relatively large-scale periodic structures (*e.g.*, parallel lines, voxelated patterns) consisting of micro-scale features [12], [101], [158]. Uzel et al. investigated the non-planar multinozzle AM for the printing of relatively low-resolution parallel-line patterns (*i.e.*, nozzles diameter = 1.37 mm) made of soft viscoelastic inks on substrates featuring complex topography by independently controlling the nozzles height [120]. The method successfully demonstrates the proof-of-concept of multinozzle AM on non-planar surfaces, although the prints dimensions are relatively small (*i.e.*, few cm wide). The printhead moves at only 5 mm/s in a Cartesian plane (*i.e.*, using a 3-axis gantry system) with vertically oriented nozzles that vary in height to print on the complex topography. The independent variation of nozzles height alone allows for non-planar multinozzle AM, yet the nozzles are rarely oriented perpendicularly to the surface throughout the print. The use of a 6-axis robot arm could complement the efficiency of a multinozzle printhead to achieve fast large-scale AM of non-planar

parts with complete freedom of printhead orientation following multiple printing paths along the substrate curvature.

In our previous work, a 6-axis robotic AM infrastructure was presented to demonstrate the performance of high-speed multinozzle AM of large-scale planar microscaffold networks [158]. The use of a multinozzle printhead allowed the AM of networks as big as 9×10^4 mm² and as thick as 50 layers (~ 10 mm) at a high flow rate (*i.e.*, > 300 mm³/s) while preserving fine features. However, the manufacturing was limited to planar substrate and the material used was a soft paste-like organic ink [115] that could not cure into a solid material.

In this work, the 6-axis robot arm is exploited to develop a large-scale non-planar multinozzle AM method using all six degrees of freedom. The objectives of this work are: (1) to develop a non-planar Multinozzle Toolpath Generator (referred as the MTG) for multinozzle AM using 6-axis industrial robot arms, and (2) to experimentally demonstrate the non-planar multinozzle AM printing method. The achievement of those objectives is shown by tailoring a thermosetting polymer material that features post-printing shape retention for AM of large-scale microscaffold networks similar to those presented in [158]. Then, the developed MTG is used to 3D-print the microscaffold networks on a small, single-curved, non-planar sinusoidal surface and a large, double-curved surface of an aircraft casing of ~ 1 m radius.

5.2 Experimental methods

5.2.1 Material preparation

The material used for all printing experiments was an epoxy composite formulation composed of a mixture of 10 parts of epoxy resin (Epon 828, Hexion, Columbus, Ohio, USA) and 4 parts of curing agent (Epikure 3274, Hexion, Columbus, Ohio, USA) filled with 14 wt% of hydrophilic fumed silica (Aerosil 200, Evonik, Germany). The aerospace-graded Epon 828 epoxy resin was selected for its relatively low viscosity and reasonable gel time at room temperature. The fumed silica was added to modify the rheological properties of the epoxy formulation to grant post-extrusion shape retention properties [11], [159]. The concentration of 14 wt% fumed silica was experimentally determined by gradually increasing the fumed silica composition within the epoxy

mixture (as explained in previous work [11]) and tailoring the apparent viscosity η_{app}through capillary rheology experiments (as developed in [40]).

The epoxy formulation was prepared by mixing the fumed silica with the epoxy resin and the curing agent individually using a speed mixer (FlackTek SpeedMixer DAC 330-100 SE, USA) at 2750 rpm for 30 s (repeated 3 times for a more homogeneous mixing). Then, both filled epoxy and curing agent were mixed together at the weight ratio of 10:4 using the speed mixer at 2750 rpm for 30 s, but only once to prevent overheating and the premature acceleration of the curing process. A few drops of red food coloring (Plochman's, Altius Spice, Montreal) were also added prior to the final mixing to improve visualization.

After mixing, the epoxy formulation was loaded into the multinozzle printhead reservoir using a silicone spatula. The reservoir was then sealed and mounted on the upper part of the printhead, already installed on the 6-axis robot arm. For the AM on the sinusoidal surface, a volume of 48 cm^3 was prepared, and a larger volume of 96 cm^3 was prepared for the AM on the aircraft casing.

5.2.2 Material rheology

Rheological behaviors of the epoxy formulation were measured using a modular compact rheometer (MCR 502, Anton Paar, Germany) fitted with a parallel plate geometry (25 mm diameter, 1 mm gap) at 25 °C. Five different rheological testing procedures were carried out in this study. (1) Shear stress amplitude sweep test was carried out to investigate the linear viscoelastic region (LVER) of the material at shear strain in the range of γ = 0.01 – 10%, and angular frequency ω = 10 rad/s. (2) The material's viscosity η at low shear rate was measured using rotational shear rheology performed using the rheometer at $\dot{\gamma}$ = 10^{-3} – 10^{2} s^{-1}. (3) The material's process-related apparent viscosity η_{app} at high shear rate was measured using capillary rheology method as presented in [40], [158] at room temperature for process-related apparent shear rate $\dot{\gamma}_w$ > 10^{2} s^{-1}. (4) Oscillatory time sweep was then performed to investigate the working time (defined as the time required to complete a print after final mixing of the material) of the epoxy formulation by measuring the evolution of complex viscosity $\eta^{\star}$ over time, at γ = 0.1% within the LVER and angular frequency ω = 10 rad/s. (5) The material's shear storage G' and shear loss G'' moduli's time-dependant behavior were investigated using a three interval thixotropy test (3iTT) [160] at

four consecutive time periods after mixing (5 min, 45 min, 67 min and 84 min). The 3iTT consisted of three different oscillatory parameters, which mimicked the structural deformation and regeneration of the material during extrusion through the nozzles [161], [162]. The first interval was conducted under a low shear strain γ = 0.1%, followed by a high shear strain γ = 100% for 18 s and back to low shear strain γ = 0.1% with all intervals at constant angular frequency ω of 10 rad/s.

5.2.3 3D-printing of the sinusoidal substrate and tooling

To realize the AM of a non-planar microscaffold network with single curvature, a sinusoidal shaped substrate was manufactured using grey photopolymer resin (Formlabs FLGPGR04) in a desktop stereolithography (SLA) 3D printer (Form 2, Formlabs, Boston, MA, USA). The non-planar surface curvature was generated using:

$$z = 5.266 \cdot \sin\left(\frac{\pi}{100}(x - 100)\right) \tag{5.1}$$

for $x, y \in [0, 200]$ mm, and small pyramids were included in three of the non-planar surface corners for the calibration of its reference frame. The surface was fabricated in four sections due to the limited build area and was assembled on a 3D-printed frame made of polylactic acid (PLA) using a quick-set two-parts epoxy glue (J-B Weld, USA). The top surface of the assembled substrate was hand sanded to obtain a smooth finish at the junctions using 60-grit, 240-grit, and 1000-grit sandpapers. For the AM on the aircraft casing, the pyramids were first fabricated separately using the grey photopolymer resin with the SLA 3D printer, and were glued to the surface of the casing. To calibrate the reference frame of both non-planar surfaces, a calibration tip was fabricated using PLA in a Fused Filament Fabrication 3D printer (Raise3D Pro 2, USA).

5.2.4 Non-planar substrate topography acquisition and reference frame calibration

Figure 5.1 shows the topography acquisition and reference frame calibration method of the non-planar substates, using the sinusoidal surface as example. The general approach is to align the reconstructed mesh of the scanned non-planar substate with the actual non-planar substate using

the three pyramid tips. Figure 5.1a shows the topography acquisition of the non-planar substate. A structured light 3D scanner (GOM Atos Core 200, GOM Metrology, Germany) was mounted on a 6-axis robot arm (Fanuc M-20iB/25, Fanuc Canada Ltd., Canada) to scan the non-planar substate (including the three pyramids). Note that multiple 3D scan recordings were necessary to obtain the entire surface topography. Figure 5.1b shows the creation of the mesh reference frame. The mesh was imported in the post-process software GOM Inspect (GOM Software 2021) and the pyramid tips were precisely located by intersecting three of the planes for each pyramid. The mesh origin (which was arbitrarily set by the scanner at first) was then aligned with the three pyramid tips using the GOM Inspect 3-2-1 alignment tool [163] to create the mesh reference frame. Figure 5.1c shows the creation of the experimental reference frame. The PLA calibration tip was mounted on the 3D scanner and used to locate the spatial coordinates of the three small pyramid tips. Their locations were then used to generate the experimental location of the reference frame origin (X, Y and Z axis), using the Fanuc User Frame three points method [77], so that the experimental reference frame matched the mesh reference frame. The matching of both reference frames completed the calibration of the non-planar substate reference frame, which ensured that any location on the scanned mesh would match the real-life location on the actual substate. Precise reference frame calibration is crucial to prevent the nozzles from colliding with the substrate.

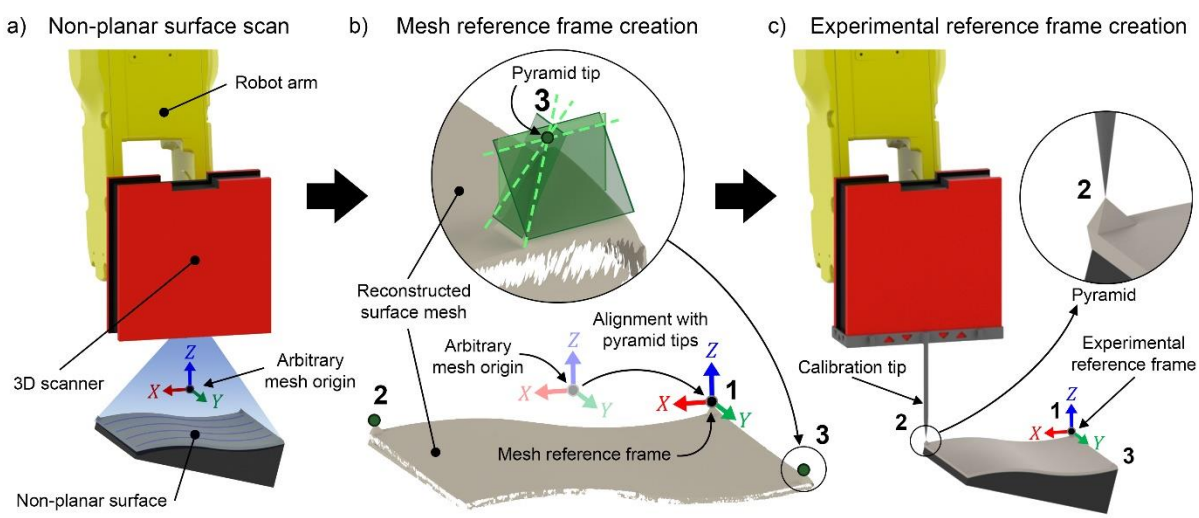

Figure 5.1. Non-planar substate topography acquisition and reference frame calibration method. a) 3D scanning of the substate, including the calibration pyramids (mesh origin is arbitrarily generated). b) Creation of the mesh reference frame by aligning the mesh origin with the pyramids

tip included in the scanned mesh. c) Creation of the experimental reference frame using the calibration tip.

5.2.5 Non-planar multinozzle AM using 6-axis robot

Figure 5.2 presents the designed general workflow which allows the 3D printing of large-scale non-planar microscaffold networks (based on the planar microscaffold network design described in [158]). Figure 5.2a presents the concept for generating a non-planar microscaffold networks. The developed MTG software was used to generate an AM toolpath for a planar microscaffold network and project its coordinates on the mesh of a non-planar substate (see Section 5.3 for more details on the MTG development). The resulting non-planar AM toolpath was then converted to the proprietary file format for Fanuc (*i.e.*, TPP) and imported to the 6-axis robot controller. Figure 5.2b shows the AM of the non-planar microscaffold network on the non-planar substate using the 6-axis robot. A custom-made flow rate-controlled multinozzle Direct Ink Writing printhead (Mëkanic – FACMO Chair collaboration, Montreal, Canada) was synchronized with the robot's motion at a desired material extrusion linear velocity (referred as printing speed) to extrude the thermosetting polymer material.

Figure 5.2c shows a close-up view of the network being printed on the non-planar substate. Microscaffold networks were fabricated in a non-planar layer-by-layer fashion by keeping the printhead oriented with the surface normal $\vec{\boldsymbol{n}}$ at each coordinate, and by alternating the printhead rotation from 0 to 90° around the $\vec{\boldsymbol{n}}$ axis between the layers. Each layer was produced by interconnecting perpendicular arrangements of a series of parallel printing passes to constitute a network of non-planar microscaffolds. Figure 5.2d shows a close-up view of a printing pass, featuring the material extrusion through the 1D multinozzle array. The printhead's 1D multinozzle array is composed of linearly distributed nozzles equally spaced by 1 mm (center to center). In a printing pass, the printhead was simultaneously extruding from 26 nozzles with and inner diameter D = 0.250 mm and a length of 6.5 mm. Completed prints were left to cure for 48 hours at room temperature. In order to be able to remove the printed microscaffold networks for characterization after curing, a thin polyethylene wrap film (~ 20 µm thick) was installed on the non-planar substate prior to launching the print.

5.2.6 Printhead tool center point calibration and toolpath recording

Prior to launching a print, the Fanuc User Tool three points method [77] was used to locate the spatial coordinates of the first and last nozzles of the 1D multinozzle array. Then, an average was calculated on the coordinates of the two nozzles to obtain the calibration of the multinozzle printhead tool center point (TCP).

Experimental AM toolpaths were recorded by saving the TCP position along the executed toolpath as a function of time using Labview (2018, National Instrument) with the DigiMetrix Robotics Library for Fanuc (DigiMetrix GmbH, Germany) at a sampling rate of 0.07 s per sample.

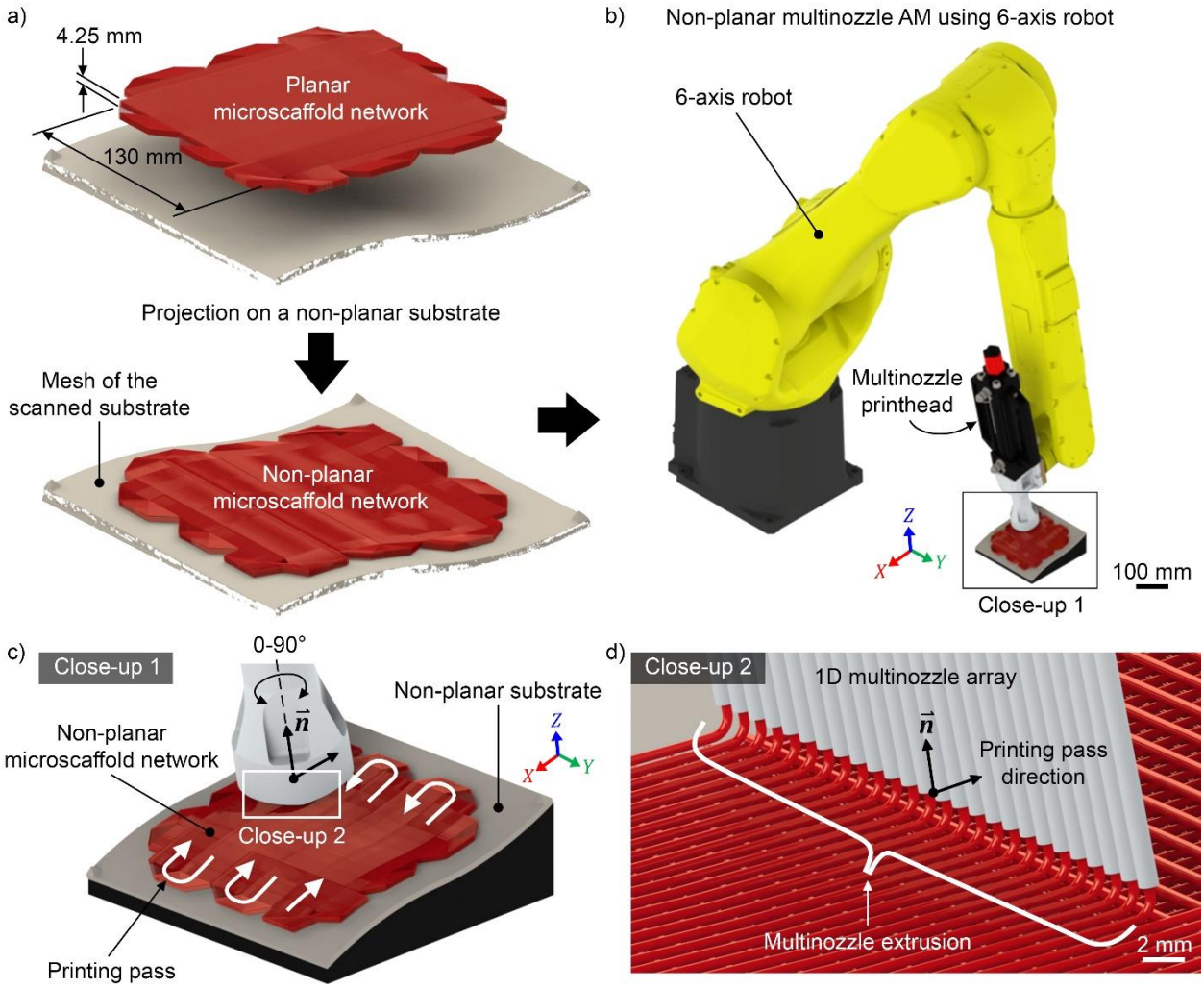

Figure 5.2. Non-planar microscaffold networks manufacturing workflow (using the single curvature sinusoidal surface as example). a) Non-planar microscaffold networks generation using

the developed MTG. b) Non-planar multinozzle additive manufacturing using 6-axis robot. c) Close-up 1: detailed view of the 3D printing of a non-planar microscaffold network. d) Close-up 2: detailed view of the multinozzle extrusion through the 1D multinozzle array.

5.2.7 Characterization of printed non-planar microscaffold networks

Prints were observed using a stereo microscope (Olympus SZX12, Olympus Corporation, Japan) and microscope images were analyzed using an image processing software (ImageJ, version 1.52a). Non-planar printed microscaffold networks were characterized by measuring the printed filaments diameter d, the horizontal inter-filament spacing p (referred as pore size), and the vertical center-to-center spacing $\bar{z}$ (referred as layer spacing) from cross-section side views. Cross-section views were obtained by carefully slicing a thin portion of the cured microscaffold networks with a precision cutting knife (X-ACTO, Westerville, Ohio), using the microscope for sequential image acquisition, and seamlessly stitching the separated images in Adobe Photoshop (CS6).

To evaluate the accuracy of the MTG software, the programmed toolpaths were first rendered as a mesh using Blender (Blender Foundation, version 3.0.1) and compared with a point cloud recording of the experimental toolpaths using the software CloudCompare (version 2.12.4). The MTG accuracy was analyzed by computing the absolute euclidean distance of the cloud-to-mesh comparison method [164].

5.3 Multinozzle Toolpath Generator (MTG)

The MTG is a custom toolpath generator programmed in the Python programming language. The MTG generates non-planar microscaffold network toolpaths (based on the geometry presented in [158]) for multinozzle AM on non-planar substrates using a 6-axis industrial robot arm. The Mayavi library is used for the post-process visualization [165].

5.3.1 Parametrization of the scanned non-planar surface mesh

Figure 5.3 illustrates the main steps of the MTG process using the sinusoidal substate as an example. Figure 5.3a shows a perfectly ordered planar grid mesh (composed of $n_x \times n_y$ vertices, along the X and Y axis, respectively) generated in Blender. The grid mesh is projected on the calibrated non-planar surface mesh (see Section 5.2.4 for reference frame calibration) using the

"Shrinkwrap" Blender modifier in the negative direction of the Z axis. The size of the grid projected onto the XY plane should not exceed the size of the surface mesh, as the grid must be able to conform to a region of the real surface that has been scanned. The ordered grid, which conforms to the non-planar reconstructed surface mesh, is parametrized using the Python library NURBS-Python [166] to obtain a non-uniform rational B-spline (NURBS) surface. The NURBS surface S is generated by a parametric function f, constructed by second-degree splines, using the collection of $n_x \times n_y$ vertices as control points, such that:

$$S = f(u, v) \tag{5.2}$$

where u and v are the surface parameters. S can be evaluated at any given (u, v) parameter pair to evaluate any point on its domain and obtain its Cartesian coordinates (x', y', z'), its surface normal $\vec{\boldsymbol{n}}$, and surface tangents along u and v ($\overrightarrow{\boldsymbol{t_u}}$ and $\overrightarrow{\boldsymbol{t_v}}$, respectively).

5.3.2 Non-planar toolpath generation

Figure 5.3b presents the non-planar toolpath generation step. The print geometry and parameters (*e.g.*, material used, printing speed, number of layers, layer height, etc.) are taken as inputs to generate a planar multinozzle toolpath. The coordinates (x, y, z) of each layer of the generated planar toolpath are mapped with their closest neighboring coordinate (x', y', z') on S. To do so, the relative x and y position of each coordinate, with respect to the domain of S, are used as (u, v) inputs to locate the closest neighbor of the toolpath coordinates on S. The (x', y', z') coordinate of each evaluated neighbor are used to perform a projection of their mapped coordinate and z is used to position the layers away from the non-planar surface along $\vec{\boldsymbol{n}}$. The first layer z position is set to 100% of D, while z is incremented by 80% of D for the subsequent layers to promote layer bonding, based on results reported in [148]. The successive projection of each coordinate using their mapped neighbor results in a non-planar toolpath that now conforms to the NURBS surface S.

For each non-planar toolpath coordinate, the surface tangent $\overrightarrow{\boldsymbol{t_u}}$ is used to determine the direction in which the printhead faces while printing and $\overrightarrow{\boldsymbol{t_v}}$ is parallel to the 1D multinozzle array. Both tangents are joined alongside $\vec{\boldsymbol{n}}$ to compose a 3×3 orthogonal orientation matrix that represents the orientation of the printhead in space around its TCP for each coordinate of the non-planar toolpath. For the toolpath generation of microscaffold networks, the orientation matrix is then

rotated 90° around $\vec{\boldsymbol{n}}$ for even-numbered layers and reset to 0° for odd-numbered layers. Each orientation matrix is used to find a unique rotation matrix $\boldsymbol{R}$ with respect to the scanned surface mesh reference frame, so that:

$$\boldsymbol{R} = \begin{pmatrix} t_{u,x} & t_{v,x} & n_x \\ t_{u,y} & t_{v,y} & n_y \\ t_{u,z} & t_{v,z} & n_z \end{pmatrix} \boldsymbol{B}^{-1} \tag{5.3}$$

where $\boldsymbol{B}$ is an orthonormal basis composed of the non-planar substate calibrated reference frame vectors (*i.e.*, the identity matrix in most cases). Rotation matrices are used to solve the inverse kinematic problem required for the robot arm movements.

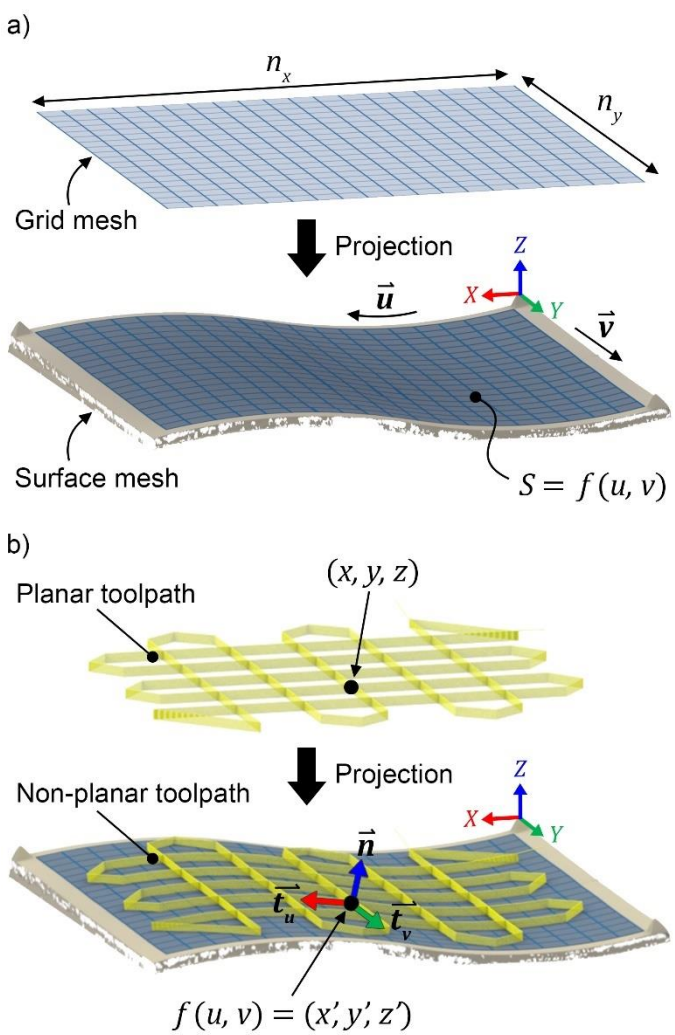

Figure 5.3. Schematics of the two main MTG process steps where the non-planar sinusoidal surface is used as an example. a) NURBS surface parametrization on the calibrated scanned mesh of non-

planar surface. b) Non-planar toolpath generation by projection of the planar toolpath on the NURBS surface.

5.3.3 Inverse kinematic problem solving

The non-planar toolpath is sent to a robotic simulation software (RoboDK, version 5.4.1) along with generated rotation matrices for all its coordinates to solve the inverse kinematic problem of the 6-axis robot trajectory. The solution to the inverse kinematic problem results in a 6-axis robot trajectory with precise robot arm joints configuration for each position of the AM toolpath. Each joint configuration allows the multinozzle printhead TCP to be adequately positioned and oriented in space relative to the calibrated scanned surface mesh reference frame, which corresponds to the print reference frame of the experiment.

5.4 Results and discussion

5.4.1 Material properties

5.4.1.1 Viscosity characterization

Figure 5.4 presents some of the rheological properties of the epoxy composite formulation. Figure 5.4a shows the measured material's viscosity η (obtained via rotational rheology) with respect to the shear rate and process-related apparent viscosity η_{app} (obtained via capillary rheology) with respect to the process-related apparent shear rate. Results for η and η_{app} are fitted using a power law model (*i.e.*, $\eta = K\dot{\gamma}^{n-1}$), thereby obtaining the power law index n = 0.2429 and flow consistency index K = 10,120 Pa·s^{n} [38], that span both low and high studied shear rates. The viscosity decreases with increasing shear rate, revealing the shear-thinning behavior (n < 1) of the epoxy formulation. The power law parameters can be used to predict the required extrusion pressure for the AM process [158], which was useful to find the proper FS wt% loading during material development. Viscosity measurements for $\dot{\gamma}$ > 10^{0} s^{-1} were excluded from the fit due to material instabilities occurring in the rheometer, as reported in [11].

5.4.1.2 Working time

Oscillatory time sweep as presented in Figure 5.4b demonstrates the time-dependence of the epoxy's complex viscosity η^* after the final mixing of the resin and curing agent (test started at t = 7 min 30 s). From t = 7 min 30 s to 45 min, $\eta^\star$ increases from 1.4 × 10^4 Pa·s to 2.2 × 10^4 Pa·s (1.57 times). The complex viscosity profile is important to understand the pressure required to extrude the material over time. Thus, the working time of this epoxy formulation for the multinozzle extrusion process can be estimated by accounting the extrusion time (which mostly depends on the printing speed and print dimensions) and the time for material preparation (e.g., mixing, filling, and installation of material reservoir) which usually varied between 10 – 20 min. Material extrusion can therefore be carried out without difficulty up to t = 45 min, since the complex viscosity increases steadily up to this point (provided that the extrusion pressure also increases accordingly).

Another aspect to be considered for evaluating the working time of the epoxy formulation is its recovery of viscoelastic properties after the removal of shear stress. Figure 5.4c shows shear storage G' and shear loss G'' moduli of the epoxy formulation within four time periods tested after mixing via 3iTT. At the third interval (*i.e.*, after the removal of high shear stress), the material showed immediate recovery of storage modulus G' while dominating the loss modulus G'' for every time period (from t = 5 to 84 min). A storage modulus G' greater than the loss modulus G'' over time leads to a favorable printability [167] within a working time of up to at least t = 84 min after final mixing.

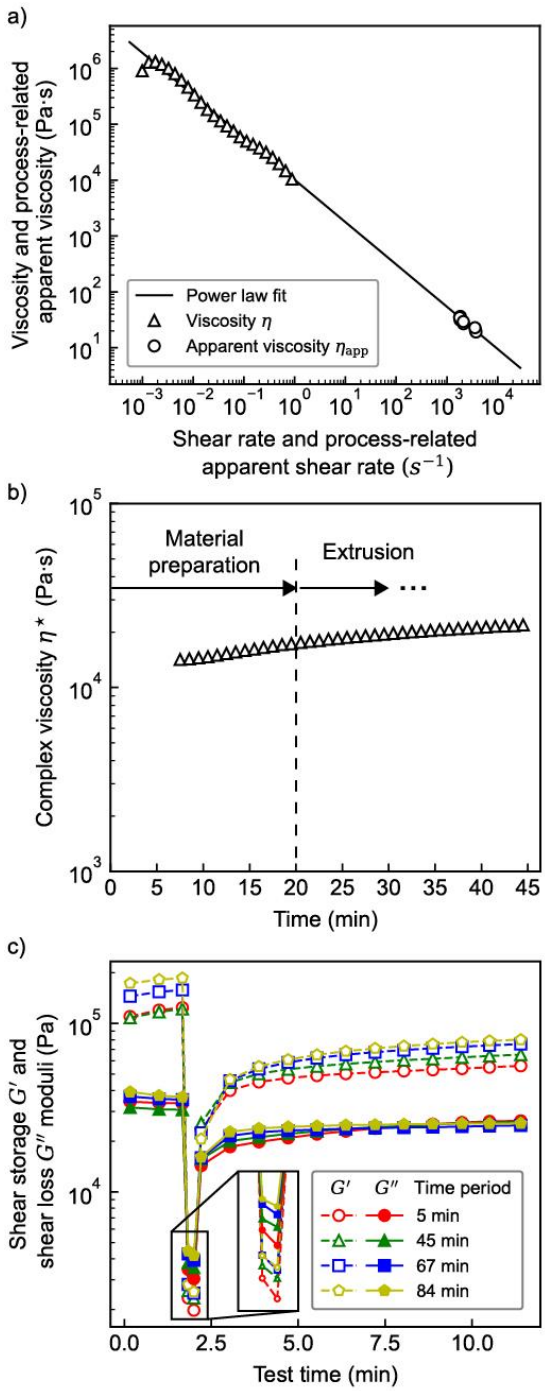

Figure 5.4. Epoxy formulation rheological properties. a) Shear-thinning fluid behavior of viscosity (obtained by rotational rheology) and process-related apparent viscosity (obtained by capillary rheology). b) Time-dependency of complex viscosity over 45 min obtained by oscillatory time sweeps. c) Shear storage and shear loss moduli time-dependency of the epoxy formulation within four time periods tested after mixing via 3iTT.

5.4.2 AM of non-planar microscaffold networks

5.4.2.1 Single curvature sinusoidal surface

Figure 5.5 shows the visualization module of the MTG process for the single curvature sinusoidal surface. Figure 5.5a shows the generated non-planar toolpath with orientation matrices (*i.e.*, vectors $\vec{\boldsymbol{n}}$, $\overrightarrow{\boldsymbol{t_u}}$ and $\overrightarrow{\boldsymbol{t_v}}$) for each TCP coordinate. The non-planar toolpath appears to conform to the NURBS surface so that the orientation matrices follow the curvature of the non-planar surface. Yet, the non-planar toolpath only gives the positions and orientations of the TCP on the NURBS surface. Since the TCP is calibrated at the middle position of the 1D multinozzle array, a collision detection was programmed in the MTG to detect potential collision with the NURBS surface and prevent damage to the nozzles.

Figure 5.5b shows the collision detection visualization, using cyan lines, for the location of the nozzle tips of the 1D multinozzle array (referred as a multinozzle footprint) along the non-planar toolpath. The collision detection for only the first two layers of the non-planar toolpath is calculated since those are the layers at 0 and 90° closest to the substrate. For each footprint, positions at both ends of the nozzle array are calculated on opposite side of the TCP along the direction of $\overrightarrow{\boldsymbol{t_v}}$ and compared to their closest neighboring coordinate on the NURBS surface. It was found that the majority of multinozzle footprints collide with the surface in the concave region (represented by a pink line on Figure 5.5b). To avoid the collision of a nozzle with the surface (represented by a red sphere), the toolpath coordinate (*i.e.*, at the TCP) is offset toward the positive direction of $\vec{\boldsymbol{n}}$ so that both ends of the nozzle array are at a distance equal to at least 100% of D from the surface for the first layer, and 180% of D for the second layer (as mentioned in Section 5.3.2). In this specific case, a maximum relative distance between the TCP and the top of the surface $\Delta z = 2.2D$ was calculated to allow adequate non-planar deposition while avoiding collision between the multinozzle and the concave region of the surface. Since a maximum $\Delta z = 24.2D$ was found to be the limiting distance before the non-planar multinozzle extrusion fails to be satisfactory (see Supplementary Section 5.6.2 for the experiment), a positive offset of $\Delta z = 2.2D$ along $\vec{\boldsymbol{n}}$ is within the allowable range to achieve non-planar multinozzle AM on the sinusoidal surface. After a coordinate is offset toward $\vec{\boldsymbol{n}}$, the rest of the coordinates above it on the following layers are also offset by the same calculated distance.

Figure 5.5c shows the prediction of the non-planar microscaffold network printed geometry. Filaments of the network seem to be projected on the surface adequately by following the curvature of the NURBS surface. However, it appears that the pore size increases (*i.e.*, creating an uneven spacing) between two printing passes on the convex region of the surface as the filaments are further from the surface. The same irregularity can be found in the concave region, but the uneven spacings decrease to a smaller pore size on the last layer. Uneven spacings are caused by a toolpath distortion following the projection on the non-planar surface. Those uneven spacings are not important when the curvature is small, because the toolpath distortion is imperceptible. However, when the surface curvature is high, the distortion is noticeable and the spacing can become negative (in concave region) to the point that some nozzles can collide with already printed filaments.

Figure 5.6 shows a non-planar microscaffold network printed on the sinusoidal surface with single curvature. The resulting print is a ~ 130 mm × 130 mm × 4.25 mm curved epoxy microscaffold network (130 filaments in both direction of X and Y, and an orthogonal stacking of 20 layers) that was manufactured at a programmed printing speed of 50 mm/s in ~ 7 min 30 s (see supplementary Video 5.1). Figure 5.6a provides details about the print specifications. The filaments average diameter $\bar{d}$ is 254 µm (standard deviation σ = 14 µm, d_{theo} = 250 µm, by neglecting material swelling) and its mean relative error (MRE) is 1.5%. The average pore size $\bar{p}$ is 754 µm (σ = 25 µm, p_{theo} = 750 µm) and its MRE is 0.5%. The average layer spacing $\bar{z}$ is 390 µm (σ = 13 µm, z_{theo} = 400 µm) and its MRE is 2.4%. $\bar{z}$ is lower than z_{theo} because the viscoelastic behavior and weight of the epoxy slightly collapse the filament stacking. All geometrical specifications demonstrate compliance with the expected non-planar geometry of such microscaffold network when comparing with planar prints of previous work [158].

Figure 5.6b shows the side view of the Cross-section A – A. By generating three-points arcs using ImageJ on the stitched microscopic image of the Cross-section A – A, the first layer radii are measured at $\bar{r}_{\text{convex}}$ = 242 mm (σ = 6 mm, MRE = 1.0%) and $\bar{r}_{\text{concave}}$ = 228 mm (σ = 7 mm, MRE = 5.0%). The surface was designed with a theoretical convex and concave radius or 240 mm. The notable smaller concave radius (~ 5.0% smaller) is probably due to excessive sanding of the SLA-printed surface and might not be related to the MTG.

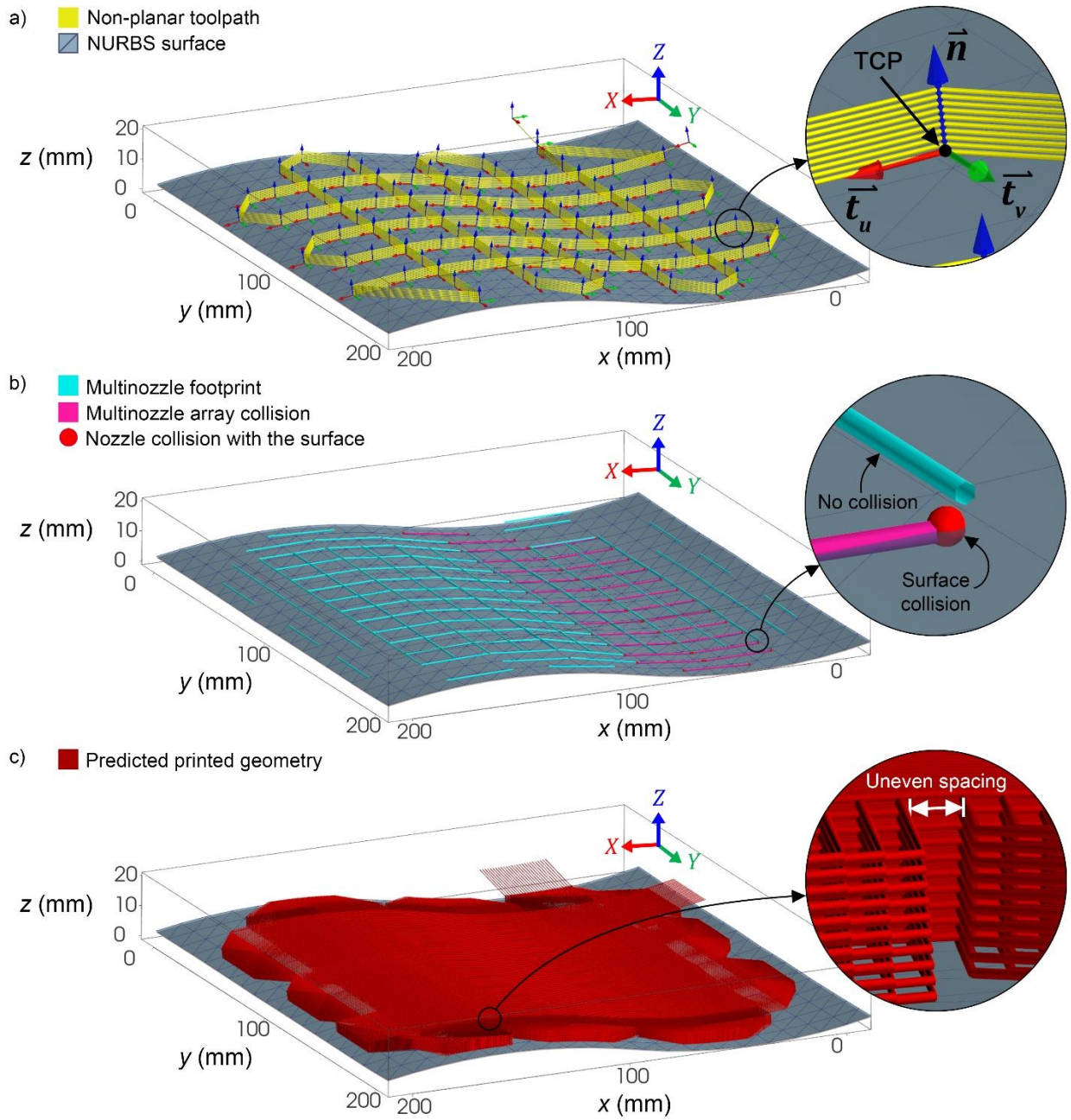

Figure 5.5. Visualization module of the MTG process for the single curvature sinusoidal surface. a) Generated sinusoidal non-planar toolpath and orientation matrices. b) Collision detection between multinozzle footprint for the first two layers and the NURBS surface. c) Prediction of the non-planar microscaffold network printed geometry. Uneven spacings are created by distortion of the toolpath following the projection.

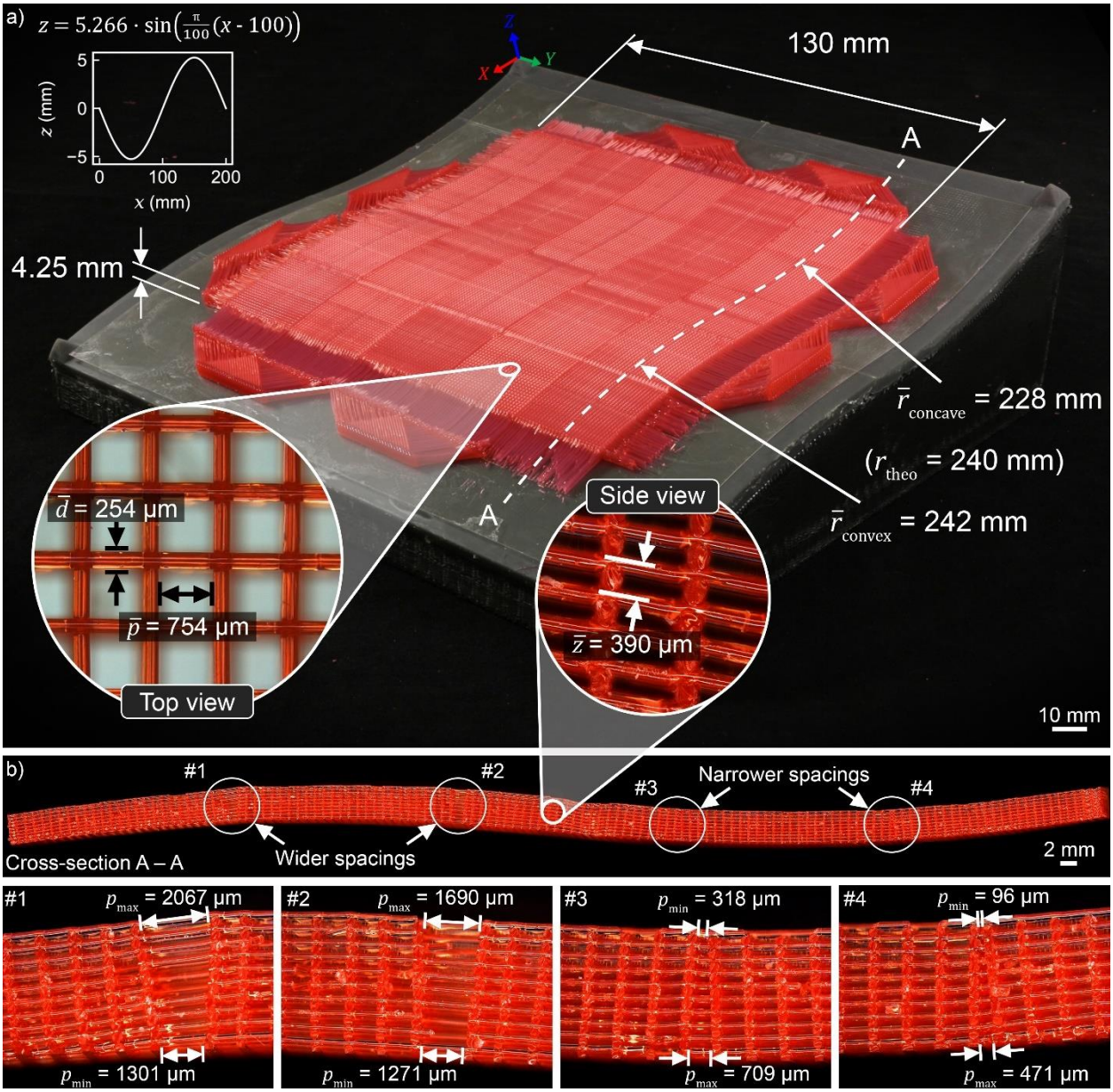

Figure 5.6. Non-planar AM of a microscaffold network on a sinusoidal surface (theoretical radius of both convex and concave region r_{theo} = 240 mm). a) Microscaffold network dimensions: ~ 130 mm × 130 mm × 4.25 mm (130 filaments in both X and Y directions, and 20 layers). Filaments average diameter $\bar{d}$ = 254 µm (σ = 14 µm, MRE = 1.5%) and pore size $\bar{p}$ = 754 µm (σ = 25 µm, MRE = 0.5%). Average first layer radii of the print: $\bar{r}_{convex}$ = 242 mm (σ = 7 mm, MRE = 1.0%) and $\bar{r}_{concave}$ = 228 mm (σ = 9 mm, MRE = 5.0%). Average layer spacing $\bar{z}$ = 390 µm (σ = 13 µm, MRE = 2.4%). b) Cross-section A – A: side view of the layer stacking showing uneven spacings between each printing pass, due to distortion of the toolpath. Wider spacings (#1 & #2) dimension

increases, and narrower spacings (#3 & #4) dimension decreases as the number of layers increase. Cross-section A – A view, the side view inset, and uneven spacing close-up views were digitally post-processed to hide the background and improve clarity of the desired features.

Four uneven spacings can be observed on the Cross-section A – A and are located between each of the five printing passes that are perpendicular to the cross-section view, as anticipated when comparing to the expected printed geometry from Figure 5.5c. Wider spacings (uneven spacing #1 & #2, located on the convex region) dimension increases from the first to the top layer. Uneven spacing #1 ranges from $p_{\min}$ = 1301 µm to $p_{\max}$ = 2067 µm and uneven spacing #2 ranges from $p_{\min}$ = 1271 µm to $p_{\max}$ = 1690 µm. Narrower spacings (uneven spacing #3 & #4, located on the concave region) dimension decreases across the stacked layers. Uneven spacing #3 ranges from $p_{\max}$ = 709 µm to $p_{\min}$ = 318 µm and uneven spacing #4 ranges from $p_{\max}$ = 471 µm to $p_{\min}$ = 96 µm. Hypothetically, those uneven spacings could be minimized by adjusting the printing passes position during the MTG process. After the first two layers are generated, the position and orientation of the multinozzle footprint for all TCP positions are known. Expected spacings on the first or last layer could be calculated by obtaining the distance between the closest ends of the nozzle array between each parallel pass. Evaluated spacings could be used as a reference offset on x and y when evaluating $S = f(u, v)$ to obtain newly adjusted non-planar toolpath coordinates (x', y', z'), reducing or increasing the first or last layer spacings to a target value between printing passes.

5.4.2.2 Surface of aircraft casing with double curvature

Figure 5.7 demonstrates the applicability of the MTG by printing a large-scale microscaffold network on the inside surface of an aircraft casing whose largest radius is ~ 1 m (see supplementary Video 5.1). In this case, the main difficulty was to generate a 3D printing toolpath that allowed the positioning of the 1D multinozzle array over a large surface featuring a double curvature (*i.e.*, similar to a hyperbolic paraboloid). Figure 5.7a shows the generated toolpath over of the NURBS surface of the casing using the MTG. Despite being limited with the possible robot arm joints configurations to orient the printhead (*i.e.*, to keep the orientation at 0 – 90°), the MTG is able to generate a non-planar toolpath for the multinozzle on the double curved surface of the scanned casing without causing any collisions between the printhead and such a large substate. Not a single

collision was detected between the 1D multinozzle array and the region of the casing surface shown on Figure 5.7a due to the small curvature of the substrate. The large-scale microscaffold network is manufactured at 50 mm/s printing speed (as for the sinusoidal surface case study) in ~ 20 min. In comparison, it would take more than ~ 8.5 hours to print the same part using a single nozzle with D = 0.250 mm at 50 mm/s. Using the multinozzle printhead at its highest flow rate (*i.e.*, ~ 300 mm³/s), the printing time would have been less than 5 min.

Figure 5.7b features the main specifications of the print (overall dimensions: ~ 402 mm × 130 mm × 4.25 mm). The print is composed of 390 filaments in the X direction, 130 filaments in the Y direction, and 20 layers. From the top view, the filaments average diameter $\bar{d}$ is 246 µm (σ = 14 µm, d_{theo} = 250 µm) and its MRE is 1.5%. The average pore size $\bar{p}$ is 755 µm (σ = 40 µm, p_{theo} = 750 µm) and its MRE is 0.7%. From the side view, the average layer spacing $\bar{z}$ is 392 µm (σ = 17 µm, z_{theo} = 400 µm) and its MRE is 2.0%. Geometrical dimensions all comply with the specifications input into the MTG with a maximum MRE of 2.0%, although uneven spacings are also present between printing passes due to the toolpath distortion in the X direction ($\bar{p}$ = 1829 µm, σ = 151 µm). There does not appear to be any noticeable uneven spacing along the Y axis since the curvature of the substrate perpendicular to this direction is small.

Next, a distance computation is performed to assess the accuracy of the recorded toolpath with respect to the programmed toolpath using the MTG. Figure 5.7c shows the visualization result of the calculation. A total of 17,196 recorded points were aligned and compared with their closest neighboring points on the theoretical toolpath to compute the absolute euclidean distance [164]. The maximum distance between the recorded and programmed toolpath is equal to 148 µm but is found where the printhead is changing joints configuration (*i.e.*, rotating between 0 and 90°) and is rapidly retracting away from the surface for the next layer deposition (*i.e.*, producing material loss outside of the microscaffold). A saturation threshold (shown in red) was set to 20 µm to be consistent with the 6-axis robot's repeatability (as provided by the manufacturer). It was found that 95% of the points have a distance below the saturation threshold and are located among the microscaffold region of the print. The analysis also reports that 84% of the points represent a distance that ranges from 0 – 10 µm (shown from blue to green, respectively). Recorded points at a distance averaging 10 µm (green) are located above the programmed toolpath coordinates at the boundaries of a printed microscaffold unit. Such a deviation from the programmed coordinates is

typical of an industrial robot arm, as its path planning process allows linear tool movements to be approximated by smoother curved paths (*i.e.*, allowing the robot to bypass the points in favor of a more fluid movement). The worst zone of the microscaffold features an average distance of 15 µm and is located in the second printing pass of odd numbered layers. Overall, the calculated distances between the recorded non-planar toolpath and the programmed coordinates are below 15 µm, which is equivalent to 6% of D.

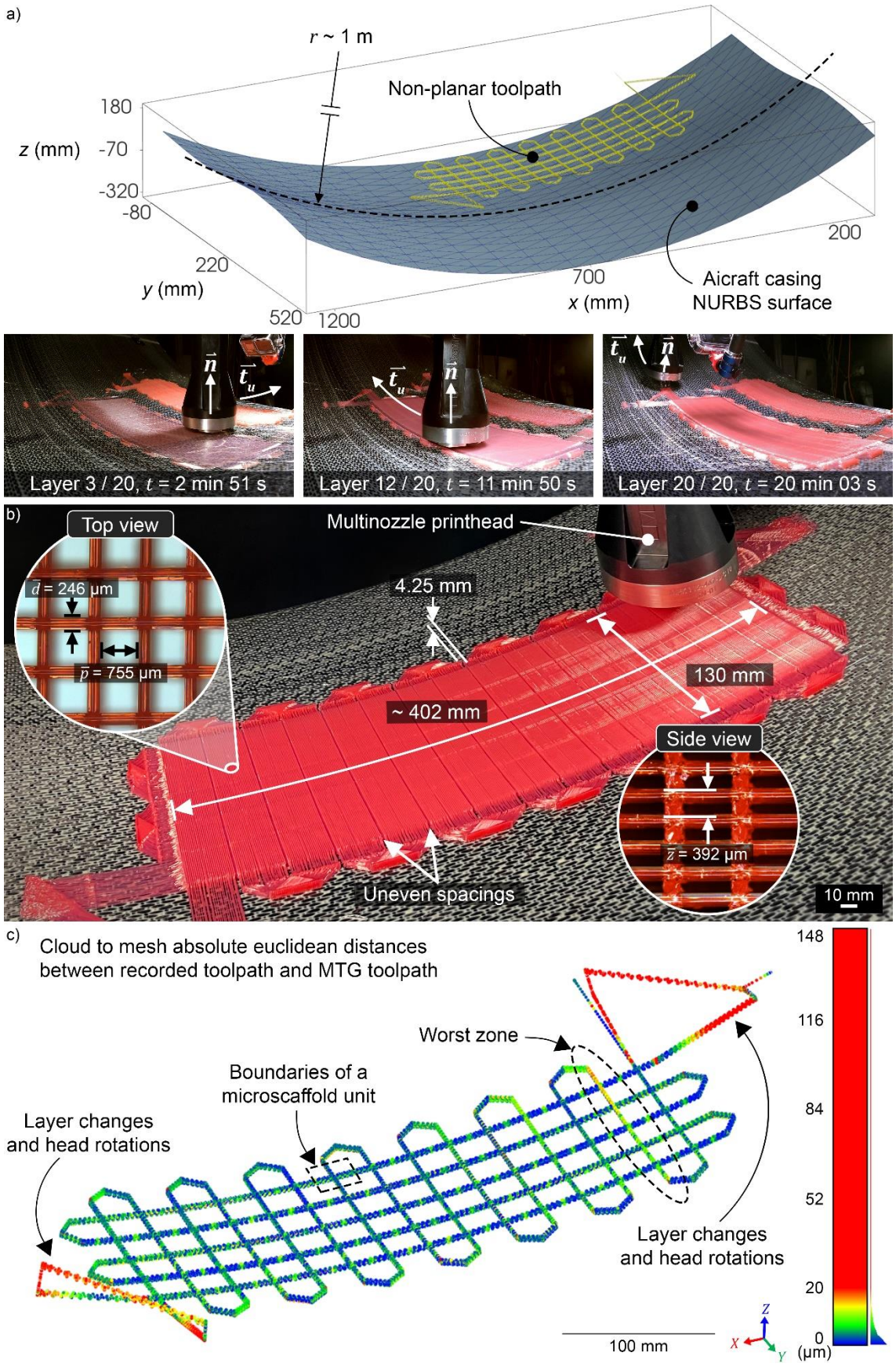
a)
r ~ 1 m
Non-planar toolpath
180
z (mm)
-70
-320
-80
220
y (mm)
520
1200
700
x (mm)
200
Aicraft casing
NURBS surface
Layer 3 / 20, t = 2 min 51 s
Layer 12 / 20, t = 11 min 50 s
Layer 20 / 20, t = 20 min 03 s
b)
Top view
d = 246 µm
p = 755 µm
Multinozzle printhead
4.25 mm
130 mm
~ 402 mm
Side view
z = 392 µm
Uneven spacings
10 mm
c)
Cloud to mesh absolute euclidean distances
between recorded toolpath and MTG toolpath
Worst zone
Boundaries of a
microscaffold unit
Layer changes
and head rotations
Layer changes
and head rotations
148
116
84
52
20
0
(µm)
100 mm
Z
X
Y

Figure 5.7. Non-planar AM of a large-scale microscaffold network on an aircraft casing. a) MTG result of the projected toolpath on the double curved surface of the casing. b) Microscaffold network dimensions: ~ 402 mm × 130 mm × 4.25 mm (390 × 130 filaments, and 20 layers). Filaments average diameter $\bar{d}$ = 246 µm (σ = 14 µm), pore size $\bar{p}$ = 755 µm (σ = 40 µm) and layer spacing $\bar{z}$ = 392 µm (σ = 17 µm). The side view inset was digitally post-processed to hide the background and improve clarity of the desired features. c) Cloud-to-mesh comparison for the computation of the absolute euclidean distance between recorded and programmed toolpaths. Saturation is set at 20 µm to be consistent with the robot's repeatability and reaches a maximum distance of 148 µm in layer changes. The microscaffold network is composed of ~ 95% of the 17,196 recorded points (~ 5% material loss), whose error is below the saturation threshold.

5.5 Conclusion

Using the freedom of movement of 6-axis industrial robot arms, the development of the MTG allowed the large-scale non-planar multinozzle AM of microscaffold networks made of an epoxy formulation. The study of the material's rheological properties (*i.e.*, viscosity, shear storage and loss moduli) shows a working time of at least 84 min after final mixing. The working time is well enough to cover the material preparation time (*i.e.*, 10 – 20 min) in addition to the printing times presented in this work (*i.e.*, maximum of ~ 20 min for the print on the aircraft casing).

Based on a surface projection method using NURBS surface parametrization, the MTG is used to project the coordinates of a planar toolpath to the scanned surface of a non-planar substate and generate a non-planar multinozzle AM trajectory for 6-axis robots. The generation of the non-planar toolpath for a sinusoidal surface case study reveals potential collisions of the 1D multinozzle array with the concave region of the surface. The collision detection feature calculated a maximum relative distance $\Delta z = 2.2D$ from the top of the substrate to prevent damaging the nozzles. The presence of uneven spacings between printing passes shows that the projection process induces a distortion of the toolpath but does not lead to a deformation of the microscaffold geometry. A greater or smaller distance between printing passes is observed depending on the substrate curvature. The observed $\bar{d}$, $\bar{p}$ and $\bar{z}$ all match the programmed specifications with small errors.

The applicability of the MTG is also demonstrated by printing a relatively large-scale microscaffold network on the double curved surface of an actual aircraft casing, without detecting

any collision with the surface. The large printed microscaffold network (overall dimensions: ~ 402 mm × 130 mm × 4.25 mm) was printed in ~ 20 min using the multinozzle printhead and would have taken more than 8.5 hours using a single nozzle with the same characteristics. Using a cloud-to-mesh comparison between recorded and programmed toolpaths, it was found that 95% of the recorded points are within 20 µm of the programmed toolpath, which supports the efficiency of the MTG. All $\bar{d}$, $\bar{p}$ and $\bar{z}$ match the specifications with small errors.

As a non-planar toolpath generator for multinozzle printheads, the MTG has a strong potential to be used as an approach in the AM of microscaffolds utilized in the fields of tissue engineering [168] and for sound proofing patterns of aircraft components [11], [169]. The developed method could also be combined with an adaptable non-planar printing bed, as reported in [170], for on-the-fly production of supportless parts. The impact of this work also encourages the use of multinozzle devices for the rapid AM of non-planar architectural structures made of concrete [85], complex shapes for the study of drug-release kinetics in the pharmaceutical field [171] and large-scale non-planar PDMS microfluidic channels [172].

Acknowledgements

We acknowledge the financial support from the FACMO Chair supported by the Natural Sciences and Engineering Research Council of Canada (NSERC, CRDPJ 514761-1), the Canada Foundation for Innovation (CFI, Project #36450), the Government of Québec (Project #36450), and Safran Group (France). The authors also thank the collaboration of Mëkanic for multiple upgrades made on the printhead, Mr. Thierry Lafrance for his help during filming, Mr. Yanik Landry-Ducharme for his help with experimental setups, Mr. David Brzeski for his help with the epoxy material, and Mr. Gabriel Chenier for his help on the calibration process.

5.6 Supplementary information

5.6.1 Supplementary videos

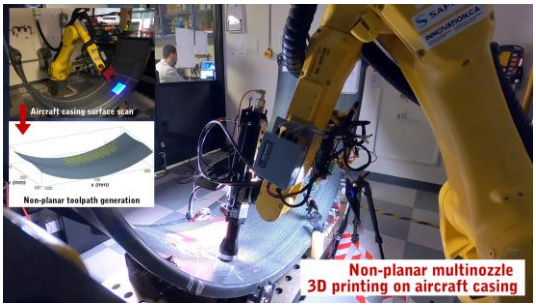

Video 5.1. Non-planar multinozzle additive manufacturing of thermoset composite microscaffold networks (available at https://youtu.be/GVyqH3ieYt0).

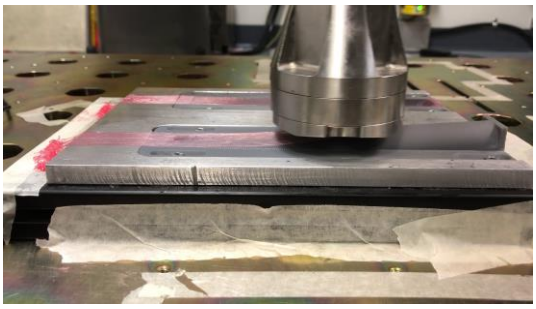

Video 5.2. Multinozzle additive manufacturing over a convex surface to study the effect of relative distance between nozzles tip and the surface (available at https://youtu.be/VeQNQTJUrB4).

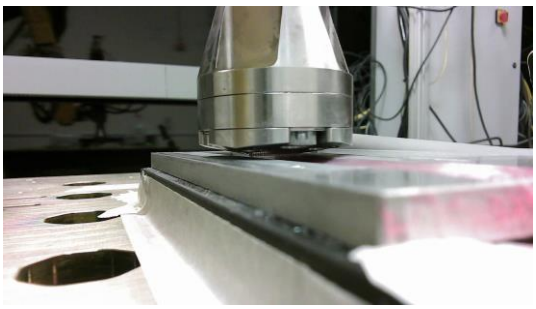

Video 5.3. Multinozzle additive manufacturing over a concave surface to study the effect of relative distance between nozzles tip and the surface (available at https://youtu.be/Sd902JQLBzU).

5.6.2 Effect of the relative distance between nozzles tip and the substrate top surface

In the general case of non-planar multinozzle AM using an 1D multinozzle array, the distance between the nozzles and the surface is rarely constant, because the printing surface is curved, unlike planar AM. Since the length and nozzle height (*i.e.*, vertical position with respect to the printhead's main axis) of the 26 nozzles of the printhead are equally fixed, some filaments may be at a greater or lesser distance from the non-planar printing surface than others when exiting the nozzles at any given time during printing. Therefore, the effect of the relative distance h between nozzles tip and the surface on multinozzle AM is investigated. A non-planar convex and a concave printing surfaces were fabricated using the grey photopolymer resin in the SLA printer. The surfaces consisted of a progressively decreasing radius over a total length L = 175 mm, starting at $r = \infty$ (*i.e.*, flat, at L = 0) and ending at its minimum dimension $r_{\min}$ = 12.5 mm (*i.e.*, half the width of the nozzle array, at L = 175 mm). Material extrusion was performed from L = -10 to 175 mm at a printing speed of 50 mm/s, where the -10 – 0 mm portion consist of a flat surface before the beginning of the radius variation. The deposition of each nozzle was then characterized for each experiment by measuring the printed filaments diameter d and the pore size p from the top view of microscopic images.

5.6.2.1 Design of experiment

Figure 5.8 presents the effect of relative distance between nozzles tip and the surface. Figure 5.8a illustrates the design of the experiment. For each surface, the printhead linearly moves from P_1 (where L = 0 and $r = \infty$) to P_2 (where L = 175 mm and $r = r_{\min}$ = 12.75 mm) while extruding the epoxy formulation at a printing speed of 50 mm/s (see supplementary Video 5.2 and Video 5.3). Figure 5.8b displays the mathematical relationships that govern the design of the surfaces. The maximum distance of the deposited filaments from the surface h linearly increases over the deposition length $L = [0, 175]$ mm to reach $h_{\max} = r_{\min}$. In order to obtain extruded filaments with diameter equal to the nozzle inner diameter, the nozzle array is positioned at an offset $\Delta z = D$ = 0.250 mm from the closest point on the surface at P_1 and P_2. For the convex surface, nozzles that are further away from the center of the array are printing over an increasing Δz ($\Delta z_{\max} = h + D$ = 13 mm = $52D$, at both ends of the nozzle array) and the center of the array is constrained at a

constant $\Delta z = D$ along L. Contrarily, for the concave surface, Δz is maximum at the center of the nozzle array and both ends are constrained to print at $\Delta z = D$. The radius of the curved surface r is calculated along L using Heron's formula for the area of a triangle [173] within the law of sines, by which the radius of a circle can be calculated using the three points of a triangle and its circumscribed circle (using h and both ends of the nozzle array to create the triangle). Starting from $r = \infty$, the radius decreases in an inverse square root trend. From L = 0 – 10 mm, r steeply decreases from ∞ to r = 112 mm, after which r slowly converges toward $r_{\min}$.

5.6.2.2 Deposition efficiency and characterization

Figure 5.8c presents top and close-up views of the linear deposition on the curved surfaces. For both convex and concave surface experiments, the filaments deposition appears intact from L = 0 to ~ 10 mm (*i.e.*, where h = 0.729 mm and $\Delta z_{\max}$ = 3.9D). At L = 10 mm on the convex surface, the average measured filaments diameter $\bar{d}$ is 249 µm (σ = 21 µm) and the average inter-filament spacing $\bar{p}$ is 739 µm (σ = 63 µm). As the printing experiment proceeds beyond L ~ 10 mm, the filaments that are extruded through the nozzles with increasing Δz are suspended in the air as they exit the nozzles, before falling onto the curved surface. At L = 140 mm, the printhead reaches a wall, where $\Delta z = D$ for each nozzle, and the filaments are supported by the wall. Filaments appear to be well deposited up to L = 140 mm, where h = 10.2 mm and $\Delta z_{\max}$ = 41.8D, beyond which the filaments are still suspended. For L = 140 mm, $\bar{d}$ = 308 µm (σ = 40 µm) and $\bar{p}$ = 697 µm (σ = 101 µm). However, it was observed that one of the outer most extruded filament broke at L ~ 80 mm. It seems that the height (h ~ 5.8 mm, $\Delta z_{\max}$ = 24.2D) at which the filament was extruded led to a sudden fracture of the filament, which caused a 4 mm long discontinuity during this filament deposition. Considering that a printing discontinuity of 4 mm indicates no filament deposition, the non-planar multinozzle extrusion seemingly fails to be satisfactory when $\Delta z \geq 24.2D$ somewhere on the nozzle array, potentially causing other printing discontinuities from this point. Results demonstrate that the average geometry of the print is still mostly intact up to L ~ 80 mm despite some of the filaments being extruded further away from the curved surface when printing. Similar observations were made on the concave surface. At L = 10 mm, $\bar{d}$ = 257 µm (σ = 22 µm) and $\bar{p}$ = 762 µm (σ = 45 µm). At L = 140 mm, $\bar{d}$ = 258 µm (σ = 31 µm) and $\bar{p}$ = 704 µm (σ = 87 µm). Assuming that the printing speed is perfectly synchronized with the motion speed of the printhead,

the effect of the relative distance between nozzles tip and the substrate top surface is therefore practically insignificant for the adequate printing of the epoxy formulation, when printing in straight lines at 50 mm/s, up to at least $\Delta z = 24.2D$.

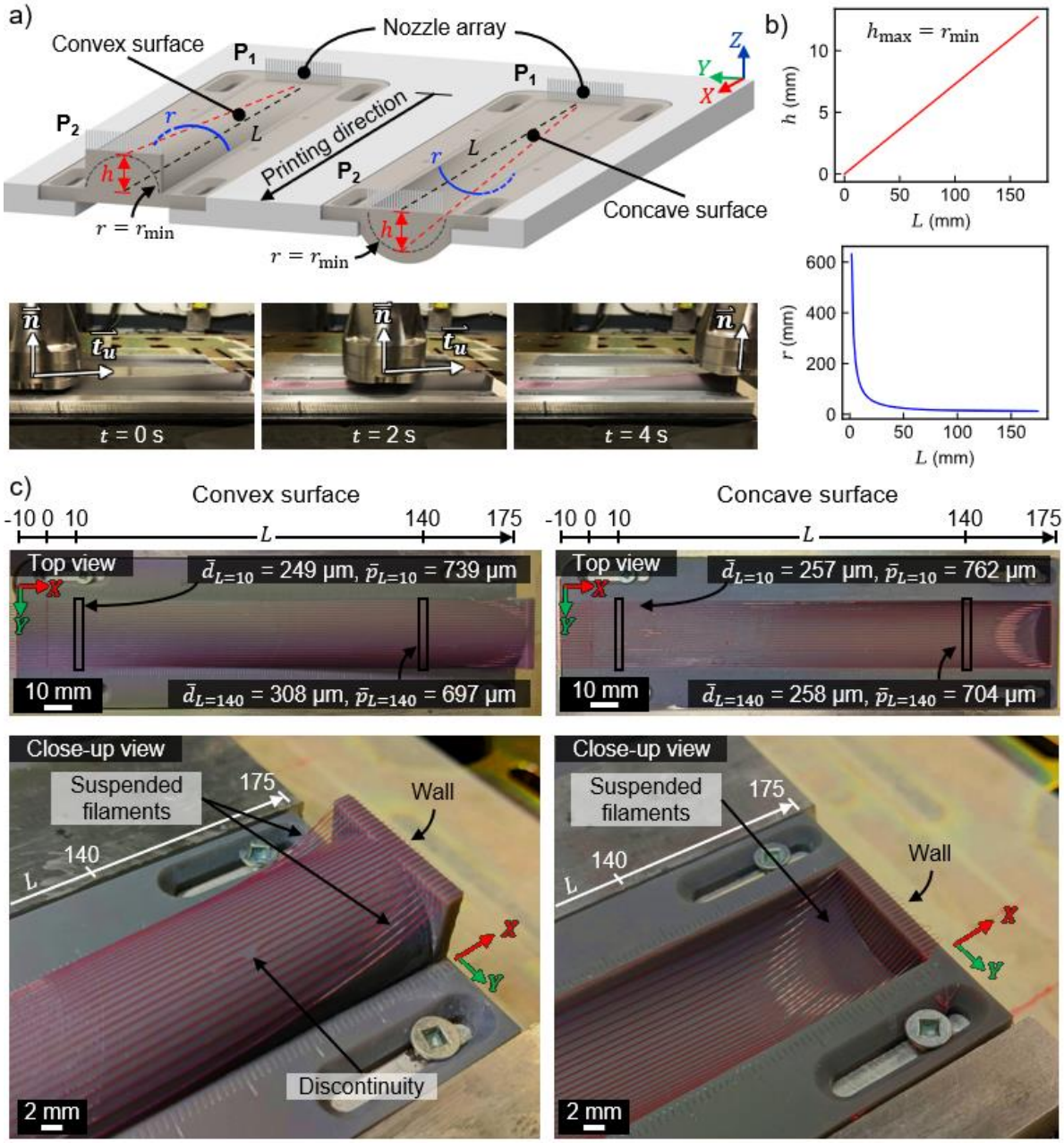

Figure 5.8. Effect of relative distance between nozzles tip and the substrate top surface. a) Design of experiment for convex and concave surfaces: the printhead linearly travels from P_1 to P_2 at 50 mm/s. b) Mathematical relationships governing the surfaces: linear increase of h with L. c) Top and close-up views of deposition results for convex and concave surfaces.

CHAPTER 6 ARTICLE 3: NON-PLANAR MULTIPROCESS ADDITIVE MANUFACTURING OF MULTIFUNCTIONAL COMPOSITES

Jean-François Chauvette[1], Iee Lee Hia[1], Juliette Pierre[1], Gabriel Chenier[1], Rouhollah D. Farahani[1], Nicola Piccirelli[2], Daniel Therriault[1]

[1]Laboratory for Multiscale Mechanics (LM[2]), Mechanical engineering department, Polytechnique Montréal, Montréal, Québec H3T 1J4, Canada

[2]Safran Paris Saclay, Centre de R&D et Bureau d'étude, Rue des jeunes bois, Chateaufort - CS80112, 78114 Magny-les-Hameaux, France

Submitted to Advanced Materials Technologies on March 13, 2023

Abstract

Multiprocess additive manufacturing (AM) consists of integrating different 3D printing techniques to enable the fabrication of multifunctional parts, based on their geometry and material properties. The combination of fused filament fabrication (FFF) and direct ink writing (DIW) techniques, respectively involving thermoplastics and thermosetting polymers (or composites), often focuses on planar and small-scale applications (*i.e.*, few cm), with limited nozzle orientation freedom for the fabrication of complex parts. Many industries, such as the aerospace sector, could benefit from the AM of lightweight multifunctional parts. For instance, one of the key aircraft component, the abradable seal coating, is applied on gas turbine engines casing to increase engine efficiency and is mechanically abraded by the rotor blades during engine startup. Abradable coatings made of thermosetting polymer could be 3D-printed using a multiprocess to obtain more functionalities. In this paper, we present a non-planar multiprocess AM approach involving FFF of a complex large sandwich panel structure with low material density and large-scale DIW of an abradable thermosetting coating with controlled porosity for sound absorption potential, and better mechanical abradability than a commercial product. This multiprocess AM approach could be used to manufacture lightweight multifunctional structural parts for the automotive or aerospace industries.

6.1 Introduction

Multiprocess additive manufacturing (AM) is an emerging field of 3D printing research allowing the use of multiple processes or techniques in a single AM build.[46] The typical approach consists of combining different types of AM technologies, such as fused filament fabrication (FFF), stereolithography (SLA), or direct ink writing (DIW), in sequence to create a more complex final product that could not be achieved with a single process.[4], [22] Multiprocess AM can lead to multifunctional devices (*i.e.*, objects with capabilities obtained from the combination of their geometry and properties) that can range, for example, from electrical or thermal conductivity, sensing capabilities or mechanical reinforcement.[41]–[44], [174] FFF of high-temperature reinforced polymers (HTRP) is typically used to add a structural function for 3D-printed parts.[49]–[51] Extrusion of HTRP usually requires a high processing temperature to melt the feedstock filament (*i.e.*, above the glass transition temperature).[175], [176] On the other hand, DIW is based on the principle of continuous extrusion of a viscoelastic ink filament through a micronozzle to form a filament when the ink is coming out and is usually performed at room temperature and its integration into a multiprocess AM build could provide complementary functionalities to the structural reinforcement of HTRP material. For example, the use of thermosetting polymers has shown potential for fire retardancy, electrostatic discharge and sound absorption, all of which could be harnessed to manufacture multifunctional industrial parts.[10], [52], [53] In general, it is necessary to use a combination of several AM techniques when the part to be manufactured is composed of thermoplastic and thermosetting polymers (or composites).

The use of combined FFF and DIW techniques was explored by Rafiee et al. to realize the multiprocess and multimaterial AM of piezoelectric polymer (using DIW) on various thermoplastic structures (using FFF).[47] The prototypes were very small (*i.e.*, few cm long) and the geometries were simple (*e.g.*, beams, dome). A combination of four AM technologies (*i.e.*, inkjet, FFF, DIW and aerosol jetting) was demonstrated by Roach et al. to fabricate various complex multimaterial, multifunctional devices.[177] Prototypes consist, among other things, of soft pneumatic actuators and stretchable electronics that are also relatively small (*i.e.*, not more than a few cm). This work is notable for the integration of a compact 6-axis robot (maximum arm reach of 665 mm) to perform only some pick and place operations during the process. Other researchers also reported the use of FFF and DIW for the multiprocess fabrication of tactile sensors for soft robotics, smart structures

with embedded flexible sensors, multifunctional drone safety cage, and triboelectric nanogenerators.[48], [178]–[180] So far, the use of thermoplastics in multiprocess AM builds has been limited to low processing temperature and relatively low-performance applications.[181] Even though, use of low-performance polylactic acid (PLA) has been investigated for the FFF of a planar multifunctional (*i.e.*, mechanical and acoustic) sandwich panel.[182] A sandwich panel is a structure made of a thick low-density core encased in thinner top and bottom skins, and is a popular structural aircraft component. The 3D-printed sandwich panel was ~ 205 mm × 76 mm × 36 mm, and had a stiffness of up to ~ 10 % higher than that of standard hexagonal honeycomb sandwich structure. Also, by printing the panel core as Helmholtz resonators (*e.g.*, shaped as hollow trapezoidal prisms designed for sound absorption), the sandwich panel featured a perpendicular angle sound absorption in the frequency range of ~ 600 to 1200 Hz. Other authors also report the use of FFF for the fabrication of sandwich panel structures that feature a sound absorption functionality.[183]–[185]

In the aerospace industry, aircraft engines operate in one of the most demanding environments, where thermal expansion, misalignment or rotation-induced stresses can cause rotating parts to rub against their casing.[122], [125] To minimize the clearance between rotor blade tips and casing, sacrificial abradable coatings are applied on the casing inner surface. When the engine is running at steady state, the rotor blades extend to abrade a layer of the sacrificial coating, and the low tip clearance prevents air from leaking further into the engine, which is critical to engines efficiency and fuel economy.[122]–[124], [130] Commercial thermosetting composites have been used in the industry as abradable coatings for low operating temperature regions (*i.e.*, up to 500 °C).[128], [129], [134], [186] Our previous work demonstrated that small-scale DIW (*i.e.*, few cm) of a thermosetting composite has potential for producing fine abradable microscaffolds featuring sound absorption functionalities in the frequency range of 500 to 6000 Hz.[11], [137] Microscaffolds are a type of micro-scale, three-dimensional periodic filaments stacking structure (*e.g.*, with layer orientation at 0 – 90°). However, scaling these particular multifunctional composite microscaffolds into actual aircraft components is a challenging task because of the usually slow printing speed and the long printing time associated with such a complex non-planar, high-resolution structure, and the need to print the actual coating on a non-planar structural aircraft component.[187], [188]

Industrial 6-axis robot arms are increasingly used as AM motion system to offer the possibility of printing more complex parts with freedom of large-scale and multidirectional printing.[81], [82] While 3D printing of large-scale functional industrial parts can be made possible by using 6-axis robot arms, associated printing times can be very long (*e.g.*, up to days).[20], [21] Long printing times can be overcome by multinozzle devices, which typically consist of a DIW printhead composed of several nozzles that can simultaneously extrude more than one filament.[12], [13], [101] The addition of a multinozzle printhead to a 6-axis robot arm has been shown to reduce the time it takes to print high-resolution large-scale microscaffold networks made of thermosetting polymer.[158], [189]

In this work, two different AM technologies, including FFF of HTRP and multinozzle DIW of a thermosetting composite are integrated into a multiprocess AM approach using a 6-axis robot arm to demonstrate a manufacturing proof-of-concept of a large-scale non-planar complex multifunctional part. The achievement of this objective is demonstrated by manufacturing a relatively large non-planar aircraft component demonstrator, composed of a curved high-performance thermoplastic sandwich panel and a network of interconnected abradable thermosetting microscaffolds. The multifunctionality of the demonstrator is obtained by manufacturing a lightweight part, featuring the combined sound-absorption potential of Helmholtz resonators and microscaffolds, and by validating the abradable functionality of the microscaffold network in comparison to a commercially available abradable coating, referred as the benchmark.[134], [169]

6.2 Results and discussion

6.2.1 Non-planar multiprocess FFF of HTRP sandwich panel and DIW of thermosetting microscaffold network

The fabrication of the aircraft component demonstrator via non-planar multiprocess FFF of an HTRP sandwich panel and multinozzle DIW of a thermosetting microscaffold network is highlighted in Figure 6.1. Figure 6.1a shows the three main steps of the multiprocess AM method. First, a 6-axis robot arm is setup with a custom heating enclosure and a high temperature FFF extruder to 3D print a curved HTRP sandwich panel. Specifically, the curvature of the sandwich

panel conforms to the double curvature of a scanned aircraft casing topography. To reduce the risk of printing failure, the overall sandwich panel is printed in four geometrically identical sections at 15 mm s^{-1} and requires a total printing time of ~ 60 h using a single nozzle of 400 µm inner diameter. Then, the panel sections are assembled together on the bottom half of the aircraft casing. The FFF extruder is unmounted from the robot flange and replaced by a 3D scanner to scan the top surface of the sandwich panel assembly and obtain a parameterized surface. The parameterized surface is then used to generate a non-planar multinozzle AM toolpath for the 6-axis robot arm (Figure 6.4, Supporting Information). The computed trajectory is used to guide a flow-controlled multinozzle printhead composed of 26 cylindrical nozzles of 6.5 mm long and 250 µm inner diameter, linearly spaced from center to center by 1 mm. The multinozzle printhead is used for simultaneous extrusion of a modified thermosetting composite abradable material, referred as the 0GM12FS formulation (Section 6.5.1, Supporting Information), in the shape of a microscaffold network. The thermosetting microscaffold network is 3D-printed in a non-planar layer-by-layer fashion, following the curvature of the top surface of the panel at a printing speed of 50 mm s^{-1}, and requiring ~ 40 min to complete (Video 6.1, Supporting Information).

Figure 6.1b shows some of the characteristics of a printed HTRP sandwich panel section. The sandwich panel consists of a bottom skin with a thickness varying from 2 – 5.8 mm, a 16 mm thick core inspired by Helmholtz resonators [182], [190] printed as a single extrusion wall of 0.4 mm thick, and a 12 mm thick top skin, comprising a grid infill. An analysis of the Euclidean distance between the computer-assisted drawing (CAD) model and the scan mesh of one of the printed panel sections (Figure 6.1c) revealed that the maximum absolute error of the geometric comparison is 0.80 mm (yellow), which can be explained by toolpath positioning miscalculations from our custom non-planar G-code slicing script. On the top surface, the maximum absolute error is 0.28 mm (in shades of green). The error is only 30 µm larger than the nozzles diameter of the multinozzle, which is not a problem for deposition of the thermosetting filaments.[189]

In the multinozzle process, the observed shear-thinning behavior of the 0GM12FS formulation (Figure 6.1d), fitted by a power law (*i.e.*, $n = 0.3578$, $K = 6{,}673$ Pa·s^n), facilitates the highly viscous material extrusion by reducing the apparent viscosity of the material η_{app} to ~ 20 – 50 Pa·s for process-related shear rates of $\dot{\gamma}_w \sim 10^3 - 10^4$ s^{-1}. The immediate recovery of shear storage modulus G' and its dominance over the shear loss modulus G'' after removal of high shear stress (Figure

6.1e) allow the printed thermosetting filaments to keep their shape upon extrusion for a working time of up to 45 min. Figure 6.1f presents a schematic of the multinozzle extrusion of the 0GM12FS formulation on top of the HTRP sandwich panel assembly. The printed thermosetting microscaffold network is 5.6 mm thick (30 layers) and is fabricated with two levels of different porosity (*i.e.*, related to the density of printed filaments in a given space), which has been shown to be effective for broadband frequency sound absorption.[169] The first printed porosity level (*i.e.*, bottom) is presented on Figure 6.1g. It is composed of layers 1 – 16 and has a thickness $\bar{z}_{\mathrm{tot}}$ of 2.83 mm (standard deviation σ = 0.12 mm, mean relative error (MRE) of = 11.6 %). The target programmed inter-filament spacing (*i.e.*, pore size) p on the bottom level is 750 µm and its averaged measured $\bar{p}$ is 726 µm (σ = 100 µm, MRE = 3.2 %). The top porosity level (Figure 6.1h), is composed of layers 17 – 30 and has a thickness $\bar{z}_{\mathrm{tot}}$ of 2.74 mm (σ = 0.11 mm, MRE = 2.2 %). Here, the filaments are printed closer together by rotating the multinozzle printhead around its axis $\vec{\boldsymbol{n}}$ by an angle θ of 64.28° to obtain a target p of 184 µm. The average observed $\bar{p}$ is 183 µm (σ = 36 µm, MRE = 0.3 %). On both levels' side view, the overall average vertical stacking distance for layers in the same orientation $\bar{z}$ is 397 µm (σ = 49 µm, programmed z = 400 µm, MRE = 0.8 %) and the overall average printed filaments diameter $\bar{d}$ is 257 µm (σ = 22 µm, theoretical d = 250 µm, by neglecting material swelling, and MRE = 2.8 %). Overall, all dimensions show consistency with the target programmed geometry of the microscaffold network. The last layer, observed from the top view (Figure 6.1i), features an average $\bar{d}$ of 256 µm (σ = 12 µm, MRE = 2.4 %) and $\bar{p}$ of 176 µm (σ = 18 µm, MRE = 4.1 %), which is in agreement with Figure 6.1h.

Figure 6.1j shows the entire printed aircraft component demonstrator. The largest radius of the demonstrator is ~ 996 mm and is located on the bottom surface of the sandwich panel which conforms to the aircraft casing curvature. On top of the panel, the curved thermosetting microscaffold network features an overall dimensions of ~ 520 mm × 78 mm. Using a single nozzle with the same characteristics as the multinozzle would have required more than 20 h to 3D print the same thermosetting microscaffold network with controlled porosity at the same printing speed. Such long printing time would have inevitably exceeded the working time of the 0GM12FS formulation or required a large number of material refills (estimated at ~ 42 refills using 3 cm³ syringes). The long printing times resulting from large-scale AM of thermoset composites could be overcome by mixing a latent curing agent into the material formulation.[191] Latent curing

agents, such as dicyandiamide, have been shown to cause very slow reactivity at room temperature (*i.e.*, over a week without any external thermal activation curing mechanisms).[192], [193] Here, the aircraft component demonstrator exhibit the capability of the developed large-scale non-planar multiprocess method for combining high-performance thermoplastics and thermosetting composites in one AM build. The AM method successfully integrates the scaling up of a tailored thermosetting composites to obtain a 3D-printed multifunctional part, composed of high-resolution micro-scale features, printed in a relatively short time.

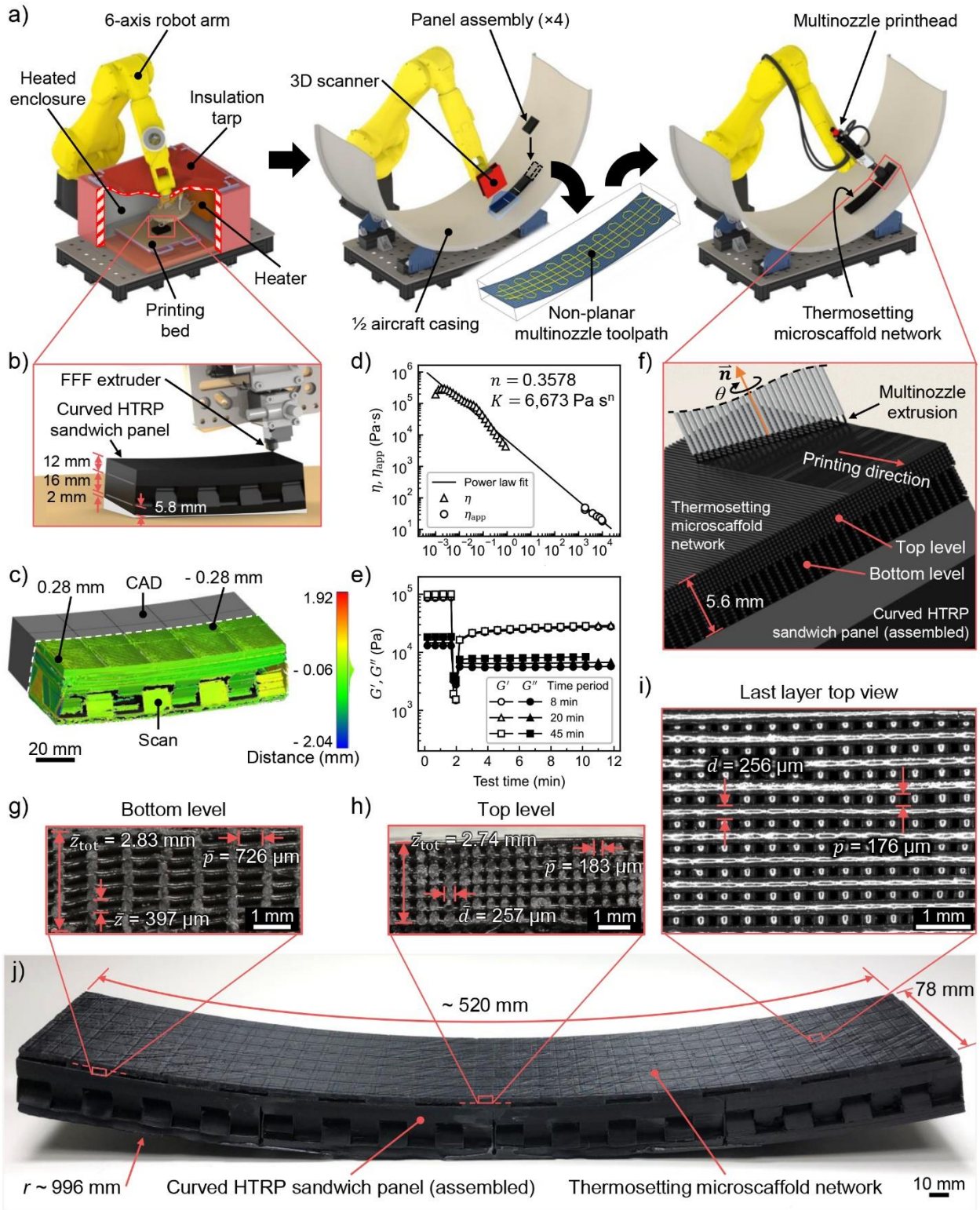

Figure 6.1. Non-planar multiprocess FFF of an HTRP sandwich panel and multinozzle DIW of a thermosetting microscaffold network. a) (1) FFF of curved HTRP sandwich panel using custom

heated enclosure and 6-axis robot arm (the enclosure is shown with an open cross-section to see the interior), (2) HTRP sandwich panel assembly on the aircraft casing, 3D scanning of the top surface topography and multinozzle toolpath generation, (3) non-planar multinozzle AM of abradable thermosetting microscaffold networks on top of HTRP panel assembly. b) Close-up view on FFF process and characteristics of a printed HTRP sandwich panel section, whose total thickness varies from 30 to 33.8 mm. c) Euclidean distance analysis from the comparison between CAD and scan mesh of a panel section. Max error on top surface is 0.28 mm. d) Abradable material (0GM12FS formulation) shear-thinning behavior of viscosity η (obtained by rotational rheology) and process-related apparent viscosity η_{app} (obtained by capillary rheology). e) Shear storage G' and shear loss moduli G'' time-dependency of the abradable material (0GM12FS formulation) obtained from three interval thixotropy test (3iTT). f) Close-up view of multinozzle DIW process and characteristics of the printed microscaffold network, whose thickness is 5.6 mm. g) Side view on the bottom porosity level, whose thickness $\bar{z}_{\mathrm{tot}}$ is 2.83 mm and pore size $\bar{p}$ is 726 µm. h) Side view on the top porosity level, whose $\bar{z}_{\mathrm{tot}}$ is 2.74 mm and $\bar{p}$ is 183 µm. i) Top view on the last printed layer, where $\bar{d}$ = 256 µm and $\bar{p}$ = 176 µm. j) Overall view of the aircraft component demonstrator. Largest radius r ~ 996 mm, dimensions of the thermosetting microscaffold network is ~ 520 mm × 78 mm. Overall filament diameter $\bar{d}$ = 257 µm and layer stacking distance $\bar{z}$ = 397 µm.

6.2.2 Multifunctionalities of 3D-printed aircraft component demonstrator

As a potential aircraft component, the 3D-printed demonstrator should be lightweight. Table 6.1 presents the density of the benchmark abradable material and different parts of the manufactured aircraft component demonstrator. The 0GM12FS formulation used to 3D print the thermosetting microscaffold on top of the HTRP sandwich panel has a density of 1.279 g cm^{-3} (due to the absence of glass microspheres), which is 153 % higher than that of the commercial benchmark material typically used as coating in aircraft engines (0.505 g cm^{-3}). However, the fabrication of the abradable coating as a microscaffold network with controlled porosity (*i.e.*, p_{bottom} = 750 µm and p_{top} = 184 µm) results in an apparent density of 0.535 g cm^{-3}, which is only 5 % higher than the benchmark's density. In addition, the density of the raw HTRP material is 1.380 g cm^{-3} (as provided

by the manufacturer) and is approximately half that of traditional aluminum alloys (*i.e.*, ~ 2.7 g cm^{-3}) commonly used for the fabrication of aircraft casing.[194], [195]

Table 6.1. Density of benchmark and parts of the aircraft component demonstrator.

Part	***p* [µm]**	**Density [g cm^{-3}]**
Benchmark material	-	0.505
0GM12FS formulation	-	1.279
Bottom porosity level	750	0.346
Top porosity level	184	0.735
Overall microscaffold (both levels)	750, 184	0.535
HTRP (PEEK CF30) material	-	1.380

As a case study for the main functionality of the aircraft component demonstrator, the abradability of the printed thermosetting microscaffold geometry is tested by mimicking the abrasion event of aircraft engine fan blade tip during engine startup with the abradable coating. Figure 6.2 presents the abradability test setup and observations of the trace left by the blade during abrasion. To comply with the experimental procedure of an in-house test rig at our industrial partner, the 0GM12FS formulation is 3D-printed using a single nozzle, as a smaller planar microscaffold geometry (~ 45 mm × 45 mm × 6 mm) that matches the characteristics of the top layers of the non-planar thermosetting microscaffold network printed using the multinozzle printhead (*i.e.*, d = 250 µm, p = 184 µm, z = 400 µm) (Figure 6.2a). Figure 6.2b shows the experimental setup of the abradability test. During the test, the titanium blades rotate at 15,000 rpm, penetrate the sample following a depth setpoint of 1 mm by moving up the sample with the stage, and remove parts of the abradable material in a circular trace, while the sample temperature is recorded using a thermal camera.

Figure 6.2c shows the close-up top view of the blade trace on a solid molded block made of the benchmark material, which is used as a reference. The blade trace is ~ 8.6 mm wide and features an averaged length of ~ 35.1 mm. Figure 6.2d shows a similar top view of the blade trace on the 3D-printed sample made of 0GM12FS formulation. The blade trace is ~ 8.6 mm wide and ~ 36.6 mm long (dimensions not shown). It appears that some of the filaments diameter have enlarged (orange region) by ~ 15 % after abrasion. The sample reached a temperature of T ~ 160 °C (Figure 6.2e) in the region of the blade trace for a duration of ~ 6.5 s during the test, which is

higher than the glass transition temperature T_g of the 0GM12FS formulation of 45.1 °C. The rubbery state of the material at T ~ 160 °C can perhaps explain the enlargement of filaments, which would imply that some of its mechanical properties are reduced compared to its glassy state. The printed filament deformation hypothesis is supported by the blade – coating interaction that typically involves structural wear and a contribution from thermal effects that can result in plastic deformation and extensive flow of the coating, leading to some smearing.[196], [197] The enlargement of filaments caused some of the pore sizes to be slightly reduced by ~ 15 % (orange region). In some cases, the pores appear to be blocked by material that was probably smeared or removed during the abrasion (red regions). It is possible that the pore size variation could alter the sound absorption functionality of the abradable thermosetting microscaffold network, as reported by some studies.[169], [198]

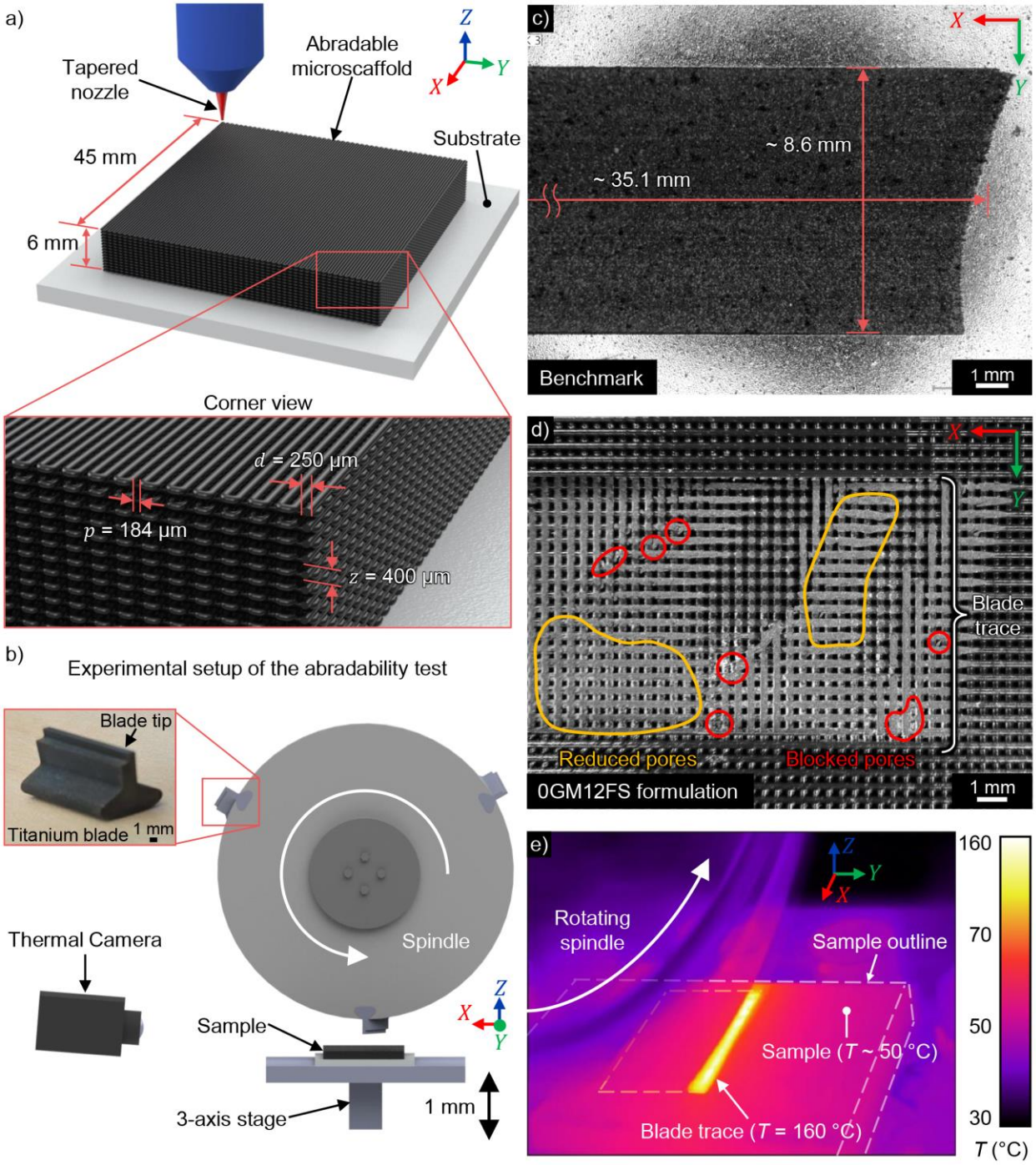

Figure 6.2. Abradability test setup and blade trace results. a) Schematic of a 3D-printed abradable sample made of the 0GM12FS formulation using a single nozzle (~ 45 mm × 45 mm × 6 mm). b) Schematic of the abradability test rig. Three titanium blades are mounted on a rotating spindle while the abradable sample is mounted on a 3-axis stage. A thermal camera is used to record the temperature profile of the 3D-printed sample throughout the process. Once the spindle reaches the

rotating speed of 15,000 rpm, the stage is moved toward the spindle at the linear speed of 0.15 mm s^{-1} and penetration depth of 1 mm. c) Microscopic top view of an abraded benchmark sample showing a blade trace of ~ 8.6 mm wide and ~ 35.1 mm long. d) Microscopic top view of an abraded 0GM12FS formulation sample. The blade trace shows that some pore sizes are reduced after abrasion (orange region) while some pores appear blocked (red regions). e) Side view from the thermal camera during the abradability test. The sample reached a temperature T = 160 °C at the location of the blade trace during abrasion.

Figure 6.3a shows a bar chart of the measured pore size area occupied by air with respect to the overall blade trace area from the top view, referred as percentage of open area (POA). The measurements are reported for the last layer of the 3D-printed samples before the abradability test and for the remaining abraded layers on top of the 3D-printed samples after the test. Based on the microscaffold characteristics presented in Figure 6.2a, the theoretical POA can be calculated using:[169]

$$\mathrm{POA_{theo}} = \frac{p^2}{(p+d)^2}\,. \tag{6.1}$$

POA_{theo} is found to be 18 %. Before the test, the POA of the 3D-printed microscaffold was measured at POA_{before} = 19 % (σ = 1 %) which is close to the value of POA_{theo}. After the test, the overall pore size is reduced, and it was observed that POA_{after} = 16 % (σ = 2 %), which is caused by reduced pore size and blocked pores. Although a POA reduction of 3 % (from 19 % down to 16 %) is observed after the test, the POA_{after} is still in range of POA_{theo} when adding the error bar of POA_{after} (*i.e.*, σ = 2 %) and should not significantly reduce the sound absorption functionality of the microscaffold network.[198], [199]

Figure 6.3b shows a bar chart of the measured maximum blade penetration depth (*i.e.*, the depth to which the abradable material has been removed), based on a 1 mm setpoint. The blade penetration was measured at 126 % of the setpoint (σ = 5 %) for the benchmark samples and at 128 % of the setpoint (σ = 4 %) for the 3D-printed samples. The proximity between the blade penetration values on both samples shows that the material removal performance of the 0GM12FS formulation is similar to the performance of the benchmark material. Although, as shown on Figure 6.3c, it was observed that there is a greater overall length variation of the titanium blades after abrasion of the

samples made of benchmark material than after abrasion of the samples made of the 0GM12FS formulation. In some cases of samples made of benchmark, some abraded material accumulated (positive values) on the blades during the test, thus increasing the blades length by up to 0.05 mm. Some blades were also damaged (negative values), and their length was reduced by up to 0.05 mm. In the case of samples made of the 0GM12FS formulation, no significant material accumulation was observed on the blades, but some blades were worn out by 0.02 mm, which is less than for the benchmark samples. Material accumulation on actual fan blades of an aircraft engine could lead to a weight imbalance sufficient to cause damage or reduced engine performance.[128], [129] On the other hand, the ejected particles that do not accumulate on the blades would be burned by the heat of the engine without causing degradation. Here, the 3D-printed abradable thermosetting microscaffolds made of the 0GM12FS formulation appear to perform better than the commercial benchmark material because of the similar blade penetration depth and a better preservation of the blades' integrity after abrasion. The abradability performance of the 0GM12FS formulation and the controlled porosity of the thermosetting microscaffold network printed on top of the HTRP sandwich panel demonstrate the ability to integrate lightweight functionalities and abrasion resistance into the 3D-printed aircraft component demonstrator.

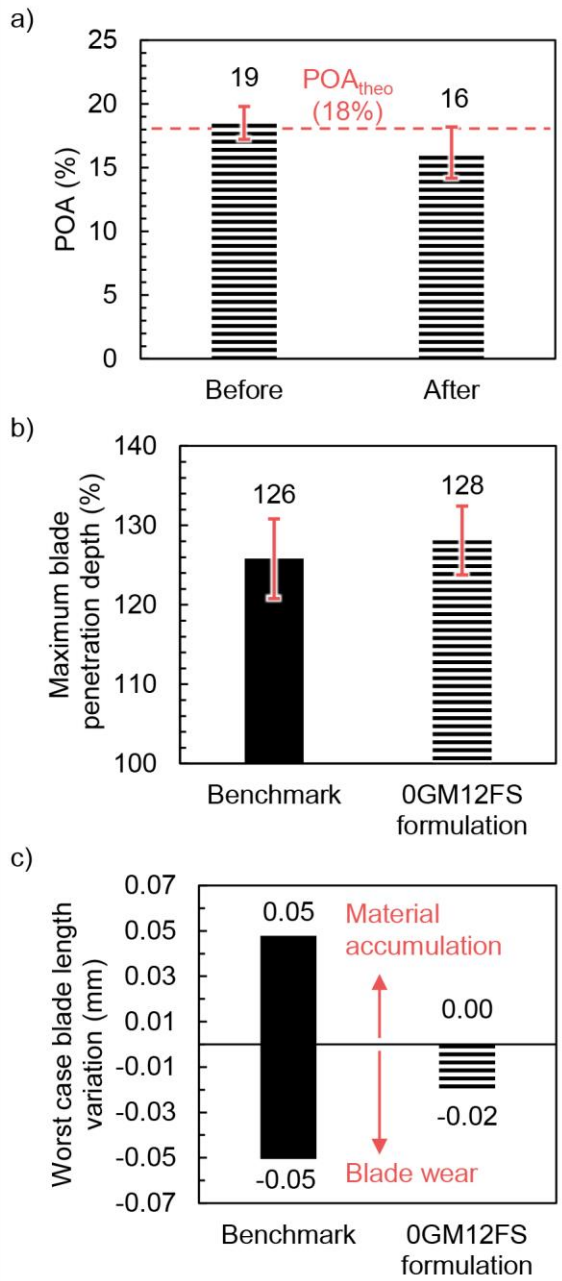

Figure 6.3. Analysis of abradability results between 3D-printed samples made of 0GM12FS formulation ≡ and molded samples made of benchmark material ■. a) Measured percentage of open area (POA) of 3D-printed sample on the last layer before the test and on the top remaining layers after the test. The theoretical POA of the printed sample is 18 %. Error bars represent standard deviation (σ = 1 % and 2 %, respectively). b) Comparison of measured maximum blade penetration depth after test for benchmark and 3D-printed samples. Percentages are given with respect to the 1 mm setpoint. Error bars represent standard deviation (σ = 5 % and 4 %,

respectively). c) Comparison of measured worst case blade length after test for benchmark and 0GM12FS formulation samples. Negative values represent a blade wear and positive values represent material accumulation on the blade.

6.3 Conclusion

In summary, we have developed and demonstrated a large-scale multiprocess AM proof-of-concept for fabricating geometrically complex multifunctional parts made of HTRP and thermosetting composites. The manufactured aircraft component demonstrator required the combination of FFF of HTRP and the multinozzle DIW of thermosetting composite using a 6-axis robotic arm. It was shown that the multiprocess method can 3D print a non-planar multifunctional part, composed of a reinforced sandwich panel coated with a thermosetting microscaffold network, that possesses abradability and lightweight functionalities. The 3D-printed porous coating made of an abradable thermosetting microscaffold network performed better than a bulk coating made of non-printable commercial abradable material, for a similar apparent density. In addition, the combination of a sandwich panel structure inspired by Helmholtz resonators and a multilevel porosity microscaffold network could show great potential for broadband sound absorption. The reported manufactured abradable thermosetting microscaffold dimensions accounts for $1/12^{th}$ of the circumference of the casing used in this work. It is estimated that it would take ~ 12 h to manufacture an abradable coating of the full circumference, which is ~ 4 times longer than the actual manual application method. However, it is important to note that the current application method does not allow the abradable material to be applied in the form of a microscaffold, which is an important added value to the proposed approach. The proposed multiprocess AM proof-of-concept presented in this work contributes to the large-scale integration of multifunctional materials into multiprocess AM by scaling up the DIW of thermosetting composites. Future work should focus on complete acoustic and mechanical characterization, which could lead to the manufacturing of lightweight, sound-absorbing, structural parts beneficial for the automotive or aerospace industry.

6.4 Experimental methods

6.4.1 Heated enclosure for AM of high-temperature reinforced polymer (HTRP)

A custom FFF printhead device was mounted on a 6-axis robot arm (Fanuc M-20iB/25, Fanuc Canada Ltd., Canada). The device consisted of an FFF extruder (Dyze Pro, Dyze Design, Canada) installed on a high-temperature resistant machined bracket made of polyetherimide (PEI), attached to the robot mounting plate. A thick (~10 mm) aluminum plate (~ 450 mm × 450 mm) covered with polyimide adhesive film (Kapton, Dupont, USA) was used as a printing bed and was heated using a silicone rubber pad heater (SainSmart, USA). A custom heated enclosure was built for FFF of high-performance polymers in a controlled heated environment. The custom heated enclosure's floor and walls were fabricated using T-slotted aluminum extrusions and polyisocyanurate R-6 insulating panels (Atlas E148, Atlas, Canada). The printing bed was placed inside the enclosure and the top opening was isolated using an insulation tarp made of silicone (Rubber-Cal, USA), attached to the machine PEI bracket. A 3.75 kW ceramic panel (CRP20074, Omega, Canada) emitting in the infrared spectrum was used to increase the air temperature inside the enclosure and was controlled with type K thermocouples. The sandwich panel was printed using a spool of polyether ether ketone (PEEK) material reinforced with 30 wt% of carbon fibers (TECAPEEK CF30 black, Ensinger, Germany). Prior to printing, the material was dried in a vacuum oven at 60 °C for 24 hours. The printing bed temperature was heated to 150 °C, the enclosure environment was heated to 110 °C and the extruder temperature was heated to 440 °C. All heaters were turned on before printing began until all temperatures stabilize.

6.4.2 Slicing and 3D printing of non-planar HTRP sandwich panel

The casing surface was scanned using a 3D scanner (GOM Atos Core 200, GOM Metrology, Germany) and reconstructed as a non-uniform rational B-spline (NURBS) surface. The NURBS surface was used in a custom FFF slicer (programmed in Python) to generate a non-planar machine language for AM (G-code) that allows the FFF extruder to be aligned with the casing surface curvature. The G-code is generated using a custom non-planar variable layer height slicing method so that the first layer of the sandwich panel conforms to the curvature of the casing and the last

layer of the panel conforms to a cylindrical shape whose revolution axis coincides with that of the casing.[62] Since the casing was too large to fit inside the heated enclosure, the panel was fabricated on top of conventional support material on a planar heated printing bed. The G-code for the support material was generated using Simplify 3D by a traditional planar slicing technique and added at the beginning of the sandwich panel G-code. The combined G-code is then converted to the proprietary file format for Fanuc (*i.e.*, teach pendant programming – TPP) and launched at a printing speed of 15 mm s^{-1}. After the print, all heat sources were turned off and the printed panel was left to cool down at room temperature overnight within the open enclosure.

6.4.3 Characterization of sandwich panel

The sandwich panel sections were individually scanned using the 3D scanner and compared with the computed-assisted drawing (CAD) model of the part. The accuracy of our HTRP FFF method was evaluated by computing the Euclidean distance between the scans and the CAD using the software CloudCompare (version 2.12.4).

6.4.4 Sandwich panel assembly

The sandwich panel sections were glued together end to end using an epoxy resin (Epon 862, Hexion, Columbus, Ohio, USA) mixed with the curing agent (Epikure 3274, Hexion, Columbus, Ohio, USA) and were left to cure for 48 h. The sandwich panel assembly was then fixed on the aircraft casing using double-sided adhesive tape (300LSE, 3M scotch, USA). Masking tape was added at the borders of the sandwich panel top surface to protect the panel from material losses during the multinozzle AM process.

6.4.5 Abradable material preparation

The commercial abradable material (*i.e.*, benchmark) (Scotch-Weld EC-3524 B/A Black, 3M, France)[134] is composed of a two-part system: an amine hardener (part A) and epoxy resin (part B) which were premixed to ~ 22.5 wt% of hollow glass microspheres (GM) (Glass Bubbles Floated Series, A20/1000, 3M, France). For the production of the abradability tests samples, the benchmark was prepared by mixing part A and B together (8 g per sample) at the weight ratio of 94:100 (part A: part B) using a speed mixer (FlackTek SpeedMixer DAC 330-100 SE, USA) at 2750 rpm for

30 s. The benchmark abradable material was not readily 3D printable (*i.e.*, could not retain its printed shape after material extrusion). Thus, the abradable thermosetting 0GM12FS formulation was developed by adding up to 12 wt% hydrophobic fumed silica (FS) (CAB-O-SIL TS-720, Cabot, USA) to the neat resins (*i.e.*, no GM content) of the commercial material, which is inspired by our previous work.[11] The 0GM12FS formulation was then prepared by mixing part A and B individually with 12 wt% of FS using the speed mixer at 2750 rpm and 30 s for three cycles. Both filled parts were then mixed together at the weight ratio of 94:100 (part A: part B) using the speed mixer at 2750 rpm for 30 s for one cycle only. For AM of an abradability test sample, the 0GM12FS formulation (3.8 g) was loaded into 3 cm³ syringes (Nordson EFD, USA) fitted with a tapered nozzle (inner outlet diameter of 250 µm, inlet diameter of 2.7 mm, and half cone angle of 5.7°). For the AM of large-scale non-planar abradable thermosetting microscaffold networks using the multinozzle printhead, the 0GM12FS formulation (160 g total) was loaded into a 250 cm³ reservoir fitted with a custom multinozzle array (Mëkanic – FACMO Chair collaboration, Montreal, Canada).

6.4.6 Material's viscosity measurements

Rotational shear rheology was performed using a modular compact rheometer (MCR 502, Anton Paar, Germany) fitted with a parallel plate (25 mm diameter, 1 mm gap) at 25 °C. The material's viscosity η at low shear rate was measured for $\dot{\gamma}$ ranging from 10^{-3} to 10^{0} s^{-1}. Viscosity measurements for $\dot{\gamma} > 10^{0}$ s^{-1} were excluded from the fit due to material instabilities occurring in the rheometer.[11] The material's process-related apparent viscosity η_{app} at high shear rate was measured using capillary rheology method at room temperature for process-related apparent shear rate $\dot{\gamma}_w > 10^{3}$ s^{-1}.[40], [158] Results for η and η_{app} were fitted using a power law model $\eta = K\,\dot{\gamma}^{n-1}$.

6.4.7 Three interval thixotropy test (3iTT)

The material's shear storage G' and shear loss G'' moduli's time-dependant behavior were investigated using a three interval thixotropy test (3iTT) using the rheometer at three consecutive time periods after mixing (8 min, 20 min and 45 min).[160] The 3iTT mimicked the structural deformation and shape regeneration of the material during extrusion through the nozzles by undergoing three different oscillatory intervals.[161], [162] The first interval was conducted under

a low shear strain γ = 0.1 % for 90 s, followed by a high shear strain γ = 100 % for 19 s and back to low shear strain γ = 0.1 % for ~ 10 min. All intervals were conducted at constant angular frequency ω = 10 rad s^{-1}.

6.4.8 Non-planar multinozzle toolpath generation

The surface of the sandwich panel assembly was scanned using the 3D scanner and reconstructed as a NURBS surface. The NURBS surface was then used to generate a non-planar multinozzle AM toolpath using the Multinozzle Toolpath Generator (MTG), a custom software based on non-planar parameterized surface projection, developed in previous work.[189] The toolpath was generated to fabricate a non-planar microscaffold network and imported in a robotic simulation software (RoboDK, version 5.4.1) to solve the inverse kinematic problem for each coordinate of the toolpath. The toolpath was then converted to TPP and imported to the 6-axis robot controller.

6.4.9 Multinozzle AM of abradable thermosetting material

The abradable coating was fabricated as a non-planar microscaffold network using a custom multinozzle printhead (Mëkanic –FACMO Chair collaboration, Montreal, Canada) mounted on the 6-axis robot arm. Extrusion was continuous along the programmed toolpath because the printhead does not have a retraction feature, which resulted in material losses outside the microscaffold network. The multinozzle printhead was flow rate-controlled and the hydraulic pressure was automatically adjusted during all the experiment to allow the multinozzle extrusion of the 0GM12FS formulation at a printing speed of 50 mm s^{-1}. The material extrusion required a pressure gradient starting at ΔP ~ 9 MPa, which increased at ΔP ~ 18 MPa after 25 min of printing time, due to polymerization of the resin. Since the maximum available hydraulic pressure of the printing process was 20 MPa, the process was paused to refill the reservoir with a fresh batch of thermosetting material and was resumed to complete the print. After printing was complete, the abradable microscaffold network was left to cure at room temperature for 48 h (as reported by the manufacturer).

6.4.10 Characterization of thermosetting microscaffold network

After the printed thermosetting microscaffold network was fully cured, material losses collected on masking tape were manually cut away using a precision cutting knife (X-ACTO, Westerville, Ohio). The microscaffold network was observed using a stereo microscope (Olympus SZX12, Olympus Corporation, Japan) and a DSLR camera (Canon EOS Rebel T4i, Canon, USA) using a macro lens (EF 100 mm 1:2.8, Canon, USA). The printed filaments diameter *d*, the horizontal inter-filaments spacing *p* (*i.e.*, pore size), the vertical layer stacking distance *z* and the porosity level thickness z_{tot} were measured using an image processing software (ImageJ, version 1.52a).

6.4.11 Abradability test samples preparation

Six aluminum substrates (7075 T6) of dimensions 60 mm × 60 mm × 3 mm were sanded using a polisher (Metaserv 2000, Buehler, UK) with 600-grit sandpaper to remove aluminum oxide layer, followed by acetone cleaning. Samples were deposited on the substrates immediately within 2 hr. For samples made of the benchmark, the prepared material was manually coated on the aluminum substrates using a silicone mold and spatula and compressed with an acetate sheet on top to achieve a flat surface. The samples were left to cure for 48 hr at room temperature and the acetate sheet was removed after curing. A total of three samples were produced with dimensions of 45 mm × 45 mm × 6 mm. Samples made of the 0GM12FS formulation were 3D-printed on top of the aluminum substrates using a material extrusion dispensing system controlled by a pressure regulator (HP-7 X, Nordson EFD, USA), operated at a pressure range of 2.7 – 5.10 MPa to match a constant printing speed of 80 mm s^{-1}. The dispensing system was installed on a 3-axis linear stage system (Aerotech, USA) made of two planar ALS25030 stages and one vertical ALS130–100 stage, controlled via the Automation 3200 software (version 2.13). The printing parameters were set to 104 lines wide and 30 layers thick, with pore size of 184 µm for each print. A total of three 3 cm^3 syringes were required to manufacture one sample with dimension of ~ 45 mm × 45 mm × 6 mm. A total of three samples were 3D-printed and subsequently left to cure at room temperature for 48 hr.

6.4.12 Abradability tests

The test rig (Safran Aircraft Engine, France) consists of a metal disk connected to a high-speed rotating spindle, a three-axis positioning stage and a thermal camera (Flir A325SC, Flir, France).

Three blades made of annealed titanium material were mounted on the metallic disk at a separation angle of 120°. Each abradable sample was fixed on the three-axis positioning stage, where lateral positions were adjusted so that the sample surface was within the cutting range of the blade tips. The vertical position was controlled remotely to determine the origin, where both the sample and blade tip surfaces touched each other. The initial position of the sample was set at 1 mm below the blade tip. Abradability tests began by increasing the spindle speed to 15,000 rpm gradually, associated with a blade tip velocity of ~ 210 m s^{-1}. Once the desired speed was achieved, the sample was raised toward the blades at a linear speed of 0.15 mm s^{-1} with a blade penetration depth setpoint of 1 mm. After the test, the sample was returned to the initial position and the spindle was stopped.

6.4.13 Analysis of abraded samples

The abradability performance of each sample was evaluated by measuring the experimental blade penetration depth using a profilometer (ContourGT, Bruker, USA). The length of each blade was also measured using a vernier caliper, before and after the tests, to verify the blade wear and the amount of abradable material sticking to the blade. Abraded samples were then observed using a digital microscope (Keyence VH-ZST, Keyence, USA) with RZ 20 – 200 × and 200 – 2000 × objectives. The percentage of open area (POA) of the 3D-printed microscaffold was measured using an image processing software (ImageJ, version 1.52a) by dividing the area of pores by the total area of the abraded region from the top view on microscopic images.

6.4.14 Differential scanning calorimetry (DSC)

The glass transition temperature (T_g) of abradable materials was determined from DSC (Q1000, TA Instruments, USA) with hermetic aluminum pans and purged with nitrogen gas at 50 ml min^{-1}. Samples were prepared by weighing and mixing parts A and B manually, followed by loading into the hermetic pan and sealed immediately. Each sample was heated from -20 °C to 200 °C at 20 °C min^{-1}, cooled down to -20 °C at 20 °C min^{-1}, and heated again at 20 °C min^{-1} to 200 °C. Only the thermal history of the second heating cycle was useful to determine the T_g. All measurements were carried out within 5 min from the moment parts A and B were mixed.

6.4.15 Density measurements

The bulk cured density of the abradable materials were measured via a helium gas pycnometer (AccuPyc II 12340, Micromeritics, USA). Cured material (~ 1 g) was poured into a 3.5 cm^3 container, and placed inside the pycnometer. The densities measured were based on the average of 100 data points. The apparent densities of the printed microscaffold network were estimated by first estimating the mass of each porosity level (by multiplying the bulk cured density of the 0GM12FS formulation and the volume of printed filaments) and then dividing the obtained masses by the overall volume occupied by the microscaffold network.

Acknowledgements

We acknowledge the financial support from the FACMO Chair supported by the Natural Sciences and Engineering Research Council of Canada (NSERC, CRDPJ 514761-1), the Canada Foundation for Innovation (CFI, Project #36450), the Government of Québec (Project #36450), and Safran Group (France). The authors also acknowledge the collaboration of Mr. Mathieu Verville for his development of the heated FFF enclosure, Mr. Dimitri Soteras for the abradability tests, Mr. Yanik Landry-Ducharme for his technical help with experimental setups, Mr. David Brzeski for his help tailoring the abradable material formulation, and the company Mëkanic for upgrades made on the multinozzle printhead.

6.5 Supporting Information

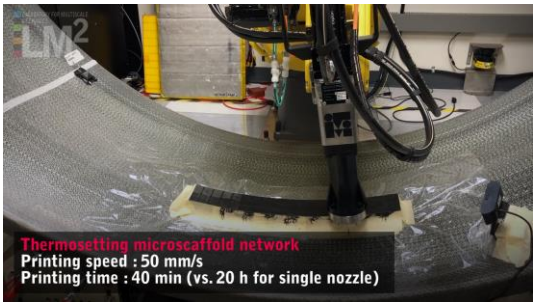

Video 6.1. Non-planar multiprocess additive manufacturing of multifunctional composites (available at https://youtu.be/rOM-yvUt5iw).

6.5.1 Comparison of commercial and modified 3D-printable abradable materials

Table 6.2 presents a comparison of the two abradable composite materials. The benchmark (Scotch-Weld EC-3524 B/A Black, 3M, France) is composed of two-part systems: an amine hardener (part A) and epoxy resin (part B). Both parts were already pre-loaded with ~ 22.5 wt% of GM intended to lower the material cured density to 0.505 g cm^{-3}. The 0GM12FS formulation (*i.e.*, addition of 0 wt% GM and 12 wt% FS) is based on the same epoxy resin and amine hardener as the benchmark, but without any GM, to avoid any risk of nozzle clogging and crushing of the GM, bringing its cured density to 1.279 g cm^{-3}.

Table 6.2. GM and FS loadings of abradable materials with the measured cured density.

Abradable material	**Part A/ part B [wt%]**	**GM [wt%]**	**FS [wt%]**	**Cured density [g cm^{-3}]**
Benchmark	77.5	22.5	0	0.505
0GM12FS formulation	88	0	12	1.279

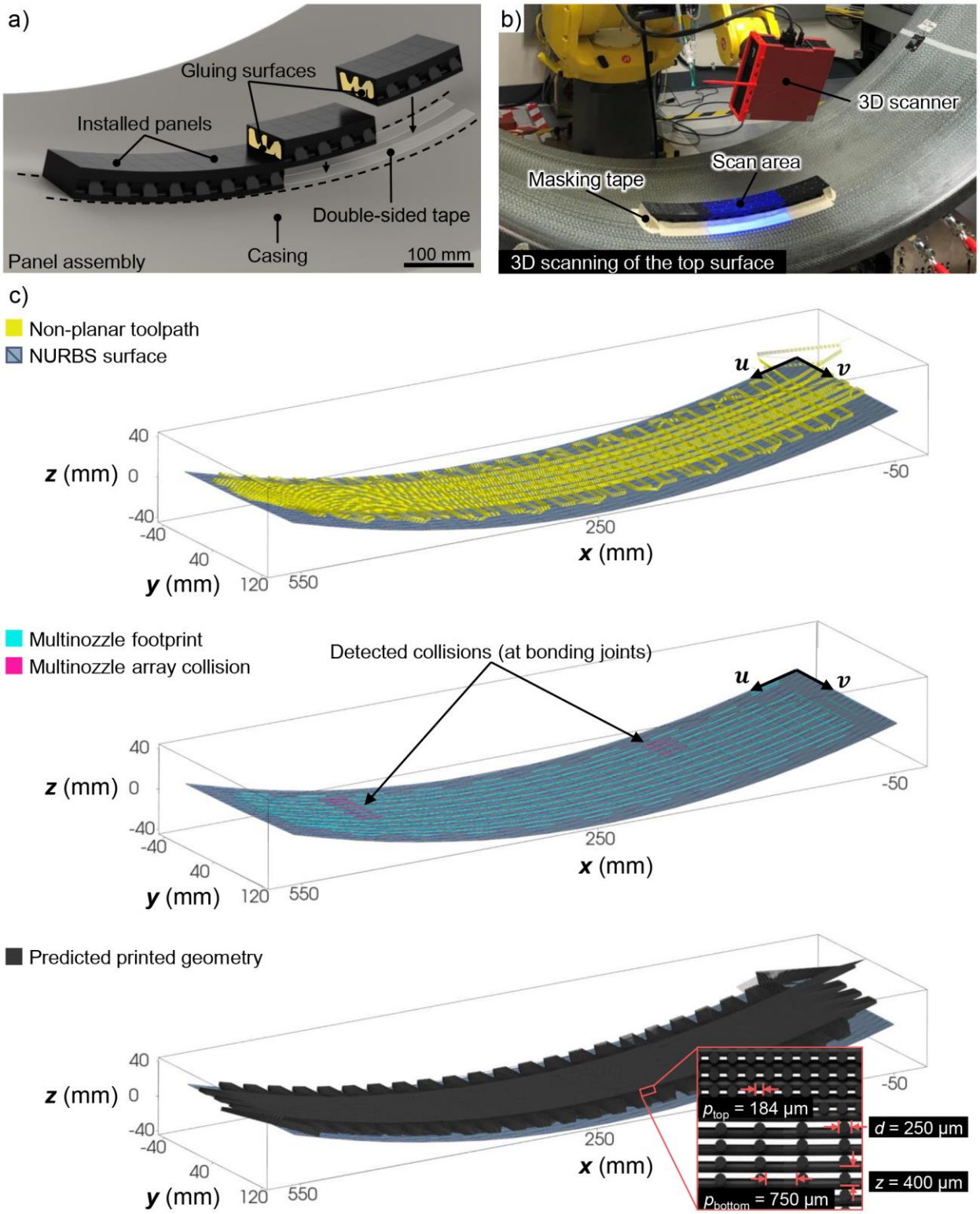

Figure 6.4. a) Sandwich panel assembly. The panels were glued together side-by-side using the epoxy resin Epon 862 and Epikure 3274 curing agent, and installed on the aircraft casing using

double-sided tape. b) Masking tape was installed on the side of the panel to protect it from material losses during the multinozzle AM process. The 3D scanner was used to obtain a mesh representation of the top surface of the panel. c) Multinozzle Toolpath Generator (MTG): the scanned surface of the sandwich panel was used to generate a NURBS surface composed of 50 × 11 control points (in the *u* and *v* directions, respectively), and second degree interpolation splines. The MTG generated a non-planar multinozzle AM toolpath on top of the NURBS surface and corrected some nozzle array collisions with the substrate (that appear to be located at the bonding joints of the panels, probably due to misalignment during assembly). Rotation matrices were calculated for all positions of the toolpath and sent to simulation software RoboDK to solve the inverse kinematic problem that allows the 6-axis robot to manufacture the printed geometry predicted by the MTG. The programmed microscaffold geometry consists of filaments diameter d = 250 µm, same orientation layer height of z = 400 µm, bottom porosity level pore size p = 750 µm, and top porosity level pore size p = 184 µm.

CHAPTER 7 GENERAL DISCUSSION

Microscaffolds that are manufactured for tissue regeneration and sound absorption patterns typically comprise micro-scale features and, so far, their overall dimensions rarely exceeded a few cm. The need to scale-up the size of microscaffolds up to the meter scale while preserving the accuracy and the repeatability of the deposited microfilaments presented a number of challenges. In this section, the following challenges will be discussed: the large volume of material required, the printing speed limitations, the characterization of large-scale high-resolution microscaffolds, the limitations of the MTG, and some of the difficulties encountered in the fabrication of the aircraft component demonstrator.

First, the large dimensions of the designed microscaffold networks required a larger volume than that of the 3 cm^3 syringes typically used for DIW. The printed microscaffold networks reported in Chapter 4 and Chapter 5 required preparing a material volume of up to ~ 50 cm^3. The abradable coating of Chapter 6 required two volumes of ~ 125 cm^3. The thermosetting materials used in Chapter 5 and Chapter 6 were two-parts epoxy composites which cure when mixed together, unlike the organic ink used in Chapter 4. Since the MEPM does not account for any time consideration in the viscosity calculation, the time to prepare, mix and fill such a large amount of epoxy into the material reservoir added some time uncertainty to the prediction of the required pressures. Since only the pressure required for extrusion at $t = 0$ (*i.e.*, after mixing) could be predicted, it was necessary to carefully monitor the pressure evolution during printing (via the Labview interface) when fabricating the abradable coating in Chapter 6 (the abradable material required the greatest pressure of the three to extrude). Although having to fill the material reservoir twice is an improvement over using 12 syringes (as reported by Dubourg-Cassagne [10]), some progress could still be made to slow down the curing reaction and allow the printing of highly viscous thermosetting material for large-scale DIW. Nevertheless, thanks to a high hydraulic pressure, the multinozzle printhead, and a tailored material viscosity, the high-speed multinozzle extrusion of thermosetting composites was investigated and the manufacturing of large high-resolution microscaffolds was made possible for a highly viscous material, which would not have been feasible using the DIW technologies available prior to this research, as described in Chapter 2.

The Fanuc robot's TCP speed could theoretically reach 2 m/s (as reported in the specifications sheet). Ideally, it was intended to print the microscaffold network of the abradable coating in

Chapter 6 at a printing speed of more than 50 mm/s. As discussed in Figure 4.5, a high printing speed of 250 mm/s was achieved at 4.75 MPa for printing of the organic ink. However, a significantly higher pressure was required to extrude the thermosetting materials at 250 mm/s. Figure 7.1 summarises the required applied pressure for extrusion of all three materials used in this project, using the MEPM.

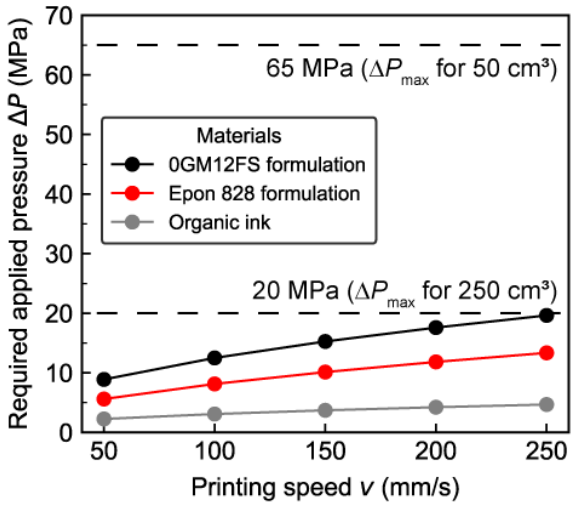

Figure 7.1. Summary of required applied extrusion pressure *ΔP* as a function of the printing speed *v* for organic ink, Epon 828 formulation and 0GM12FS abradable formulation. Maximum pressure limits are 65 MPa (for 50 cm³ reservoir) and 20 MPa (for 250 cm³ reservoir).

The maximum allowable pressure of 65 MPa mentioned in Figure 4.3a and Figure 7.1 is the maximum pressure associated with a 50 cm³ material reservoir, which uses a 28.5 mm diameter piston to push the material through the nozzle array. For the printing on the aircraft casing (Figure 5.7) and for the abradable coating demonstrator (Figure 6.1), a larger 250 cm³ material reservoir was needed, and required to use a 50.8 mm diameter piston. The circular area of this larger piston is 3.17 times that of the one used in the 50 cm³ reservoir, which reduced the applied pressure by 3.17 times and thus, the maximum allowable pressure for extrusion to 20 MPa. It was determined experimentally, and validated using the MEPM, that the pressure required after mixing to extrude the abradable material for a printing speed of 250 mm/s was ~ 19 MPa, which was very close to the pressure limit and would have inevitably resulted in exceeding the maximum after 1 or 2 min of printing. Moreover, as explained in Section 4.4.3.1, reaching and maintaining a TCP speed of 250 mm/s is difficult when the robot is rapidly changing direction due to the short travel distances,

which is exactly the case when the printhead moves in the width direction of the HTRP sandwich panel (see Figure 6.1). As a result, the maximum achievable TCP speed for printing the abradable coating was experimentally determined to be ~ 50 mm/s, which corresponds to ΔP = 9 MPa.

The large dimensions of printed microscaffold networks also made it difficult to characterize the finely printed filaments. For example, the X-ray microcomputer tomography (micro-CT) scanner could not accommodate the large printed microscaffolds presented in Chapter 5 and 6 because the dimensions of the prints exceeded the physical volume available inside the micro-CT. Thus, the limitations of the micro-CT scanner made it difficult to characterize the print quality of the filaments within the prints, unlike the thick encapsulated microscaffold network of Chapter 4. Therefore, measurements were always made on the last, uppermost printed layer to report the average filaments diameter $\bar{d}$ and average pore size $\bar{p}$. Measurements from the side views were made under microscopic observation on cross-sections (obtained by manually cutting the printed microscaffolds), but these cross-sections were difficult to obtain without destroying the printed filaments. A larger volume CT scanner (e.g., the XT H 225 industrial CT scanner, maximum active area 432 mm × 432 mm) could have been used, but the minimum pixel size is 150 µm, which is slightly more than half the diameter of our deposited filaments, resulting in a relatively low-resolution scan. The Atos Core 200 3D scanner, used to scan non-planar substrates, was also tested to scan the overall dimensions of printed microscaffold networks. However, as it is the case for the larger volume CT scanner, the method presents a low resolution (*i.e.*, a distance of 0.08 mm between two scanned points) to obtain accurate dimensions of the fine printed features. In addition, the projected structured light of the 3D scanner reflected on the glossy surface finish of the filaments and the deformation of the light could not always be recorded by the sensors of the scanner. Overall, when the robot's motion is synchronized with the printing speed, the average filaments diameter appears consistent across the layers, as observed on cross-sections in Figure 4.8 and in Figure 5.6, and as measured on Figure 6.1. In the end, the assumption of negligible swelling of polymer at the nozzles outlet, made for the development of the MEPM, was verified and the measurements made by microscopic observation were sufficient for the scope of this work.

Since the MTG is based on the multinozzle planar toolpath generation developed in Chapter 4, the principle of toolpath generation is different from that of the AM slicing methods presented in Chapter 2. The MTG is designed to avoid the need to input a CAD model and is capable of

generating a toolpath through user-entered parameters that govern the desired geometry. This design choice eliminates the need to model complex curved geometries, but also limits the design of toolpaths to overall rectangular-shaped geometries that are automatically dimensioned based on any multinozzle arrangement. Unlike non-planar slicing methods, layers of generated non-planar geometries using the MTG are always curved depending on the curvature of the scanned substrate. The MTG also does not allow for on-the-fly extrusion adjustment, which is sometimes used with FFF to compensate for toolpath distortion. Additionally, due to the limitations of the multinozzle pressure system, the MTG does not include a retraction functionality, but it could be easily implemented by the same kind of programming instructions as the extrusion. The MTG was mainly demonstrated using the multinozzle printhead developed for this work but could be used with other multinozzle configurations to produce similar printing patterns.

Finally, within the context of the FACMO research Chair, it was initially planned to fabricate a non-planar aircraft component demonstrator that would account for 1/4 of the circumference of the aircraft casing. However, the original 50 cm^3 material reservoir was too small to hold the estimated volume of ~ 750 cm^3 required for the entire print. To this end, several potential solutions were investigated with our subcontractor partner, including continuous material feed, mixing of the material inside the printhead and a larger reservoir. For time and budgetary reasons, it was decided to opt for a larger material reservoir of 250 cm^3, which allowed the fabrication of a demonstrator 3 times shorter, leading to a 1/12-circumference demonstrator. Based on experiments in Chapter 6, the initial 1/4-circumference demonstrator would have taken about 3 h to manufacture in three separated parts, assuming that the preparation and filling of the material into the reservoir takes 20 minutes and the printing takes 40 minutes. For a full-circumference demonstrator, it can be quickly estimated that the fabrication of twelve separated curved panels would have taken at least 12 h, which has potential to be cost-effective in an industrial context, considering the added value of the part. Overall, the proof of concept of 3D printing a non-planar abradable coating inspired by sound absorption patterns has been achieved. The abradability performance of the 3D-printed coating has been validated and showed similar results to the commercial product. It would have been interesting to validate the acoustic absorption and evaluate the impact of pore size reduction and pore blockage, caused by abrasion. However, because of equipment limitations and availability, there was no solution available to perform these acoustic tests on such a large sample.

CHAPTER 8 CONCLUSION AND RECOMMENDATIONS

8.1 Conclusion

In this work, the AM potential for the creation of large thermosetting-based abradable seal coatings for future generation of aircraft was investigated. A non-planar multinozzle AM method using a 6-axis industrial robot arm was developed to achieve the large-scale manufacturing of thermosetting-based high-resolution multifunctional periodic structures that are inspired by sound absorption patterns.

A custom multinozzle printhead was equipped on a 6-axis industrial robot arm to unlock the potential for high-speed and large-scale AM. Achievement of very high flow rate (*i.e.*, 319 mm^3/s) and printing speed (*i.e.*, 250 mm/s) was demonstrated while preserving the micro-scale features of printed microscaffold networks made of low-viscosity organic ink. A Multinozzle Extrusion Prediction Model (MEPM) was developed, based on capillary rheometry, to predict the extrusion pressure gradient ΔP inside the nozzles and the total volumetric flow rate Q_{tot} of the printing process. The MEPM was also used to explore the design of several multinozzle printhead configurations and their potential for reducing printing times of large-scale DIW. The multinozzle AM method was demonstrated by completing a print at 319 mm^3/s over an area of ~ 9×10^4 mm^2 in ~ 1 min 36 s, which is ~ 3 times faster than the related published work. Printing with variable inter-filament spacing up to 750 µm was also demonstrated, and a thick 50-layer print was studied to characterize the simultaneous extrusion quality, which featured an average layer stacking alignment error of 57 µm when the robot TCP velocity is synchronized with the printing speed.

A custom Multinozzle Toolpath Generator (MTG) was also programmed, based on non-planar parameterized surface projection of the planar toolpaths designed in Chapter 4, to generate non-planar toolpaths suited for multinozzle printheads and obtain 6-axis robot trajectories that follow the curvature of 3D-scanned substrates. The MTG also prevented the multinozzle array from colliding with the substrate by calculating the positions of the outermost nozzles relative to the closest points on the NURBS parameterization of the scanned substrate. A tailored aerospace-graded epoxy material (*i.e.*, Epon 828 formulation) was printed to demonstrate the non-planar multinozzle AM of large curved microscaffold networks (up to an area of ~ 5.2×10^4 mm^2 in

20 min). Printed geometries were predicted and analyzed for a single curvature sinusoidal surface and the double curvature surface of an actual aircraft casing, with a toolpath error of 15 µm.

Finally, the capability of the MTG and the proposed non-planar multinozzle AM method was demonstrated by fabricating an aircraft component demonstrator composed of an abradable seal coating on top of a curved HTRP sandwich panel. A custom abradable composite (*i.e.*, 0GM12FS formulation) was tailored for 3D printing, based on a commercial benchmark product (*i.e.*, Scotch-Weld EC-3524 B/A Black), and was integrated into a multiprocess AM approach. The approach was successfully used to 3D print a non-planar abradable thermosetting microscaffold network in ~ 40 min comprising a total of 14,040 printed microfilaments featuring an average diameter $\bar{d}$ of 257 µm (with mean relative error of 2.8 %). The 5.6 mm thick abradable coating conformed to a curved surface with overall dimensions of ~ 520 mm × 78 mm and radius of 962 mm, and accounted for 1/12 of the circumference of the aircraft casing that was used as an example during this project. Using the method to achieve the variable pore size explained in Chapter 4, the multifunctionality of the thermosetting composite was included by controlling the non-planar porosity of two coating levels (*i.e.*, 16 layers at $\bar{p}$ = 726 µm and 14 layers at $\bar{p}$ = 183 µm), inspired by sound absorption patterns, which provided the abradable coating a low apparent density of 0.535 g/cm³. From abradability tests conducted at Safran S.A., the printed 0GM12FS microscaffolds appeared to perform better than the benchmark product, with a blade penetration depth of 128 % (compared to 126 % for benchmark), no significant material accumulation on the blades, and a blade wear of 0.020 mm (compared to 0.050 for the benchmark).

This work has contributed to the multinozzle printhead development efforts, the use of 6-axis robotic arms in AM, the scaling up of the DIW technique, the development of non-planar AM methods, and advances in large-scale multiprocess AM. The full code of the two software packages developed as part of this work was also made available to the public via an Internet hosting service for software development (GitHub) [200], [201]. This study is the first to attempt non-planar multinozzle AM of thermosetting composite on large-scale substrates while providing accurate micro-scale filament deposition and to demonstrate direct application in the aerospace field.

8.2 Recommendations

Future research and work are recommended in the following areas:

Multinozzle printhead

- The multinozzle printhead communication protocol with the robot controller should be remade. At the beginning of the project, digital and analog input/output (I/O) signals were chosen for their simplicity and knowledge limitations of the Fanuc communication protocols capabilities. In retrospect, sending discretized 0 – 10 VDC analog signals that correspond to a maximum of ten possible preprogrammed extrusion linear velocity values is a very limiting approach of managing the extrusion flow rate considering the acceleration profile of the robot. The Fanuc R-30iB Plus robot controller used in this work is compatible with serial communication protocol RS-232, which allows more information to be transmitted than I/O signals. The RS-232 protocol could be used to send a printing speed setpoint as a function of the real-time TCP velocity (using the TCP speed prediction Fanuc option package) and control the extrusion flowrate using a feedback control loop that could be programmed in the Fanuc proprietary language Karel. The feedback control loop could also be used to implement a retraction feature to the multinozzle printhead, which would definitely be useful to avoid material losses.
- It should be considered to explore the manufacturing of a multinozzle printhead containing conical (*i.e.*, tapered) nozzles instead of cylindrical ones. Although it was reported by our subcontractor partner that the fabrication of cylindrical micronozzles capable of handling high pressures was already a difficult task, using conical nozzles would allow for a lower pressure drop to achieve material extrusion at the same printing speeds as reported in this work. The pressure generated at the inlet of the cylindrical nozzles for the AM of the abradable coating in Chapter 6 was very high due to the resin polymerization and reached the maximum pressure of the multinozzle controller. Using a larger diameter nozzle (i.e. > 250 µm) would also reduce the pressure drop, while producing larger extruded filaments. A lower pressure drop inside the nozzles would allow for an overall decrease of required pressure to extrude, thus a larger margin before reaching maximum allowable pressure.
- Multinozzle extrusion resulted in all nozzles being filled with leftover material inside the nozzles after printing. Purging and cleaning of the multinozzle device was meticulously performed by unclogging each nozzle with a micro-needle and a high-performance resin

remover (EpoxSol 23) in the of case epoxy resins extrusion. The current cleaning method is tedious and time consuming, which would not be suitable for industrial needs. A new cleaning method requiring minimal human interaction should be investigated.

Multinozzle Extrusion Prediction Model (MEPM)

- The MEPM should include time and temperature variables to allow the prediction of the evolution of viscosity over time for thermosetting polymers (as explained in [11]). By entering variables such as the time of mixing, time of printing, gel time and mixture temperature, the MEPM could predict the exact required pressure at the printing time estimated by the MTG, as a function of the material used and its rheological properties.
- The MEPM could also account for other neglected capillary rheology effects, when significant, such as entrance and exit effects, swelling, and wall slip. Our assumptions were based on the fact that the multinozzle printhead has a large nozzle L/D ratio and that there is no slip at the walls for tube flow, which is a standard assumption. Correcting those effects for pressure prediction would allow using a wider range of nozzles configuration with the MEPM.

Multinozzle Toolpath Generator (MTG)

- The MEPM should be integrated with the MTG in future versions of the code. In addition to the modifications already proposed for the MEPM, a more comprehensive model would allow for accurate prediction of pressure and volumetric flow rate along the generated toolpath. A better understanding of the material's viscosity and required pressure along the toolpath would allow a better control of the printing process.
- As discussed in Chapters 5 and 6, the MTG uses a NURBS surface to position and orient the multinozzle array along the toolpath. The printhead is oriented to print toward vector $\overrightarrow{\boldsymbol{t_u}}$ and is aligned using the normal vector $\vec{\boldsymbol{n}}$. Since the position and orientation of those vectors are the product of a 3D scan, they are subject to surface defects, which led to small differences between the orientation of the printhead on the same printing pass of some prints. The small differences were not sufficient to cause print failure, but it was observed that some printed microfilaments were misaligned in some printing experiments. Although

sanding to obtain a smooth surface was a suitable solution for the work of Chapter 5, a vector smoothing algorithm could be added to the MTG to overcome the vectors orientation differences due to surface defects [202], [203].

Additive manufacturing of abradable seal coatings

- The multinozzle AM of abradable material focused on a material formulation that did not include glass microspheres (GM), which are mainly used to reduce coating density. As part of the FACMO Chair, colleagues developed three abradable material formulations, one of which did not contain GM and was used for the experiments in Chapter 6. The other two formulations, which contained different amounts of GM, were quickly tested for printability using the multinozzle but the results were inconclusive. Due to time constraints and material shortage, it was decided to focus on the printability of the abradable formulation without GM. In a future work, it would be interesting to validate the printability of these abradable formulations containing GM, as their density is lower than the one used in this work.
- The abradability tests performed at Safran were all performed on planar printed samples. Although the curvature of the non-planar abradable coating is small, it would be interesting to compare the abradability performance of curved and planar samples. Abradable tests should also be conducted on the other material formulations that include GM.

Industrial 6-axis robotic arm

- The path planning of industrial 6-axis robots is calibrated using theoretical Denavit–Hartenberg parameters (*i.e.*, four physical parameters representing the position and orientation of each link in the robot's kinematic chain). To improve accuracy of the robot's positioning, an accurate kinematic calibration could be done using a laser tracker, which was reported to reduce a mean distance error by ~ 600 µm [72]. An accurate calibration of the robot could also allow for the simulation of the highest achievable TCP speed for a given toolpath, which could be used to predict the highest achievable extrusion pressure for the given printing speed, using the MEPM. Motion planning could also be tailored for process optimization by maximizing the printing speed while minimizing the robot joints rotation which often introduces precision errors such as when changing layers.

BIBLIOGRAPHY

[1] "Additive Manufacturing Global Market Report 2022: High Adoption of Additive Manufacturing in the Automotive and Aerospace Sector Drives Growth - ResearchAndMarkets.com," Dec. 15, 2022. https://www.businesswire.com/news/home/20221215005918/en/Additive-Manufacturing-Global-Market-Report-2022-High-Adoption-of-Additive-Manufacturing-in-the-Automotive-and-Aerospace-Sector-Drives-Growth---ResearchAndMarkets.com (accessed Jan. 25, 2023).

[2] L. Nickels, "AM and aerospace: an ideal combination," *Met. Powder Rep.*, vol. 70, no. 6, pp. 300–303, Nov. 2015, doi: 10.1016/j.mprp.2015.06.005.

[3] G. Daugherty, "Outside the Box: How GE Aviation Entered the Brave New World of Additive Manufacturing," *The GE Aerospace Blog | Aviation & Flight News*, Aug. 08, 2019. https://blog.geaerospace.com/manufacturing/outside-the-box-how-ge-aviation-entered-the-brave-new-world-of-additive-manufacturing/ (accessed Feb. 22, 2023).

[4] M. Rafiee, R. D. Farahani, and D. Therriault, "Multi-Material 3D and 4D Printing: A Survey," *Adv. Sci.*, vol. n/a, no. n/a, p. 1902307, doi: 10.1002/advs.201902307.

[5] A. K. Ghosh and M. Dwivedi, "Advantages and Applications of Polymeric Composites," in *Processability of Polymeric Composites*, A. K. Ghosh and M. Dwivedi, Eds., New Delhi: Springer India, 2020, pp. 29–57. doi: 10.1007/978-81-322-3933-8_2.

[6] L. Li, Q. Lin, M. Tang, A. J. E. Duncan, and C. Ke, "Advanced Polymer Designs for Direct-Ink-Write 3D Printing," *Chem. – Eur. J.*, vol. 25, no. 46, pp. 10768–10781, 2019, doi: 10.1002/chem.201900975.

[7] J. A. Lewis and G. M. Gratson, "Direct writing in three dimensions," *Mater. Today*, vol. 7, no. 7, pp. 32–39, Jul. 2004, doi: 10.1016/S1369-7021(04)00344-X.

[8] A. P. Dowling and Y. Mahmoudi, "Combustion noise," *Proc. Combust. Inst.*, vol. 35, no. 1, pp. 65–100, Jan. 2015, doi: 10.1016/j.proci.2014.08.016.

[9] R. E. Chupp, R. C. Hendricks, S. B. Lattime, and B. M. Steinetz, "Sealing in Turbomachinery," *J. Propuls. Power*, vol. 22, no. 2, pp. 313–349, 2006, doi: 10.2514/1.17778.

[10] A. Dubourg-Cassagne, "Intégration de structures absorbantes acoustique innovantes au sein d'une turbosoufflante," Master thesis, Polytechnique Montréal, Montréal, Canada, 2015.

[11] D. Brzeski *et al.*, "Design of thermoset composites for high-speed additive manufacturing of lightweight sound absorbing micro-scaffolds," *Addit. Manuf.*, vol. 47, p. 102245, Nov. 2021, doi: 10.1016/j.addma.2021.102245.

[12] C. J. Hansen *et al.*, "High-throughput printing via microvascular multinozzle arrays," *Adv. Mater.*, vol. 25, no. 1, pp. 96–102, Jan. 2013, doi: 10.1002/adma.201203321.

[13] S. J. Kranz, "Multinozzle Printheads for 3D Printing of Viscoelastic Inks," Master thesis, University of Illinois at Urbana-Champaign, Urbana, Illinois, 2013. [Online]. Available: http://stevecrayons.com/

[14] T. Lehmann *et al.*, “Large-scale metal additive manufacturing: a holistic review of the state of the art and challenges,” *Int. Mater. Rev.*, vol. 67, no. 4, pp. 410–459, May 2022, doi: 10.1080/09506608.2021.1971427.

[15] T. Wohlers and T. Gornet, “History of additive manufacturing,” Wohlers Associates, inc., Technical report, 2016.

[16] L. J. Kumar and C. G. Krishnadas Nair, “Current Trends of Additive Manufacturing in the Aerospace Industry,” in *Advances in 3D Printing & Additive Manufacturing Technologies*, D. I. Wimpenny, P. M. Pandey, and L. J. Kumar, Eds., Singapore: Springer, 2017, pp. 39–54. doi: 10.1007/978-981-10-0812-2_4.

[17] I. Simon, M. Gurley, and S. Van Roosenbeek, “Market changes and technological shifts in the 3D printing marker,” Hubs, Amsterdam, Apr. 2022.

[18] R. D. Farahani, D. Therriault, M. Dubé, S. Bodkhe, and M. Mahdavi, “6.13 Additive Manufacturing of Multifunctional Nanocomposites and Composites,” in *Comprehensive Composite Materials II*, Elsevier, 2018, pp. 380–407. doi: 10.1016/B978-0-12-803581-8.10019-0.

[19] B. Bhushan and M. Caspers, “An overview of additive manufacturing (3D printing) for microfabrication,” *Microsyst. Technol.*, vol. 23, no. 4, pp. 1117–1124, Apr. 2017, doi: 10.1007/s00542-017-3342-8.

[20] A. V. Shembekar, Y. J. Yoon, A. Kanyuck, and S. K. Gupta, “Generating Robot Trajectories for Conformal Three-Dimensional Printing Using Nonplanar Layers,” *J. Comput. Inf. Sci. Eng.*, vol. 19, no. 3, Sep. 2019, doi: 10.1115/1.4043013.

[21] K. Silver, J. Potgieter, K. Arif, and R. Archer, “Opportunities and challenges for large scale 3D printing of complex parts,” in *2017 24th International Conference on Mechatronics and Machine Vision in Practice (M2VIP)*, Nov. 2017, pp. 1–6. doi: 10.1109/M2VIP.2017.8211515.

[22] “ISO/ASTM 52900 Additive Manufacturing - General Principles - Terminology.pdf,” ISO/ASTE International, Switzerlang, International Standard 2015 First edition, Dec. 2015.

[23] R. D. Farahani, K. Chizari, and D. Therriault, “Three-dimensional printing of freeform helical microstructures: a review,” *Nanoscale*, vol. 6, no. 18, p. 10470, Jun. 2014, doi: 10.1039/C4NR02041C.

[24] A. Elkaseer, S. Schneider, and S. G. Scholz, “Experiment-Based Process Modeling and Optimization for High-Quality and Resource-Efficient FFF 3D Printing,” *Appl. Sci.*, vol. 10, no. 8, Art. no. 8, Jan. 2020, doi: 10.3390/app10082899.

[25] R. L. Truby and J. A. Lewis, “Printing soft matter in three dimensions,” *Nature*, vol. 540, no. 7633, pp. 371–378, Dec. 2016, doi: 10.1038/nature21003.

[26] S.-Z. Guo, M.-C. Heuzey, and D. Therriault, “Properties of Polylactide Inks for Solvent-Cast Printing of Three-Dimensional Freeform Microstructures,” *Langmuir*, vol. 30, no. 4, pp. 1142–1150, Feb. 2014, doi: 10.1021/la4036425.

[27] B. Wang, Z. Zhang, Z. Pei, J. Qiu, and S. Wang, “Current progress on the 3D printing of thermosets,” *Adv. Compos. Hybrid Mater.*, vol. 3, no. 4, pp. 462–472, Dec. 2020, doi: 10.1007/s42114-020-00183-z.

[28] K. K. B. Hon, L. Li, and I. M. Hutchings, “Direct writing technology—Advances and developments,” *CIRP Ann.*, vol. 57, no. 2, pp. 601–620, Jan. 2008, doi: 10.1016/j.cirp.2008.09.006.

[29] R. Bey-Oueslati, S. J. Palm, D. Therriault, and S. Martel, “High speed direct-write for rapid fabrication of three-dimensional microfluidic devices,” *Int. J. Heat Technol.*, vol. 26, p. 8, 2006.

[30] “Ender-7 3D Printer,” *creality*. https://www.creality.com/products/ender-7-3d-printer (accessed Feb. 20, 2023).

[31] N. S. Hmeidat, J. W. Kemp, and B. G. Compton, “High-strength epoxy nanocomposites for 3D printing,” *Compos. Sci. Technol.*, vol. 160, pp. 9–20, May 2018, doi: 10.1016/j.compscitech.2018.03.008.

[32] K. Chen, X. Kuang, V. Li, G. Kang, and H. J. Qi, “Fabrication of tough epoxy with shape memory effects by UV-assisted direct-ink write printing,” *Soft Matter*, vol. 14, no. 10, pp. 1879–1886, Mar. 2018, doi: 10.1039/C7SM02362F.

[33] N. Nawafleh and E. Celik, “Additive manufacturing of short fiber reinforced thermoset composites with unprecedented mechanical performance,” *Addit. Manuf.*, vol. 33, p. 101109, May 2020, doi: 10.1016/j.addma.2020.101109.

[34] T. Yuan, L. Zhang, T. Li, R. Tu, and H. A. Sodano, “3D Printing of a self-healing, high strength, and reprocessable thermoset,” *Polym. Chem.*, vol. 11, no. 40, pp. 6441–6452, Oct. 2020, doi: 10.1039/D0PY00819B.

[35] S. Chandrasekaran, E. B. Duoss, M. A. Worsley, and J. P. Lewicki, “3D printing of high performance cyanate ester thermoset polymers,” *J. Mater. Chem. A*, vol. 6, no. 3, pp. 853–858, Jan. 2018, doi: 10.1039/C7TA09466C.

[36] N. Nawafleh, W. Wright, N. Dariavach, and E. Celik, “3D-printed thermoset syntactic foams with tailorable mechanical performance,” *J. Mater. Sci.*, vol. 55, no. 33, pp. 16048–16057, Nov. 2020, doi: 10.1007/s10853-020-05111-6.

[37] R. C. Pack, S. K. Romberg, A. A. Badran, N. S. Hmeidat, T. Yount, and B. G. Compton, “Carbon Fiber and Syntactic Foam Hybrid Materials via Core–Shell Material Extrusion Additive Manufacturing,” *Adv. Mater. Technol.*, vol. 5, no. 12, p. 2000731, 2020, doi: 10.1002/admt.202000731.

[38] F. A. Morrison, *Understanding rheology*. in Topics in chemical engineering. New York: Oxford University Press, 2001.

[39] P. J. Carreau, De Kee, Daniel C.R., and R. P. Chhabra, *Rheology of Polymeric Systems : Principles and Applications*. Hanser Pub Inc, 1997.

[40] J. Bruneaux, D. Therriault, and M.-C. Heuzey, “Micro-extrusion of organic inks for direct-write assembly,” *J. Micromechanics Microengineering*, vol. 18, no. 11, p. 115020, Nov. 2008, doi: 10.1088/0960-1317/18/11/115020.

[41] J. L. C. Jr, K. H. Fehr, D. D. Kelly, D. Espalin, and R. B. Wicker, “Increasing component functionality via multi-process additive manufacturing,” in *Micro- and Nanotechnology Sensors, Systems, and Applications IX*, SPIE, May 2017, pp. 250–257. doi: 10.1117/12.2263257.

[42] S. Yang, H. Tang, C. Feng, J. Shi, and J. Yang, "The Research on Multi-Material 3D Vascularized Network Integrated Printing Technology," *Micromachines*, vol. 11, no. 3, Art. no. 3, Mar. 2020, doi: 10.3390/mi11030237.

[43] R. Tao, J. Shi, F. Granier, M. Moeini, A. Akbarzadeh, and D. Therriault, "Multi-material fused filament fabrication of flexible 3D piezoelectric nanocomposite lattices for pressure sensing and energy harvesting applications," *Appl. Mater. Today*, vol. 29, p. 101596, Dec. 2022, doi: 10.1016/j.apmt.2022.101596.

[44] S. Khuje *et al.*, "Printed Structural Temperature Monitoring Embedded in Multi-Process Hybrid Additive Manufacturing," *J. Mater. Eng. Perform.*, vol. 30, no. 7, pp. 5093–5099, Jul. 2021, doi: 10.1007/s11665-021-05658-8.

[45] R. Tao, "Multi-Material Three-Dimensional Printing of Piezoelectric Devices for Sensing and Energy Harvesting Applications," phd, Polytechnique Montréal, 2022. Accessed: Jan. 16, 2023. [Online]. Available: https://publications.polymtl.ca/10291/

[46] E. MacDonald and R. Wicker, "Multiprocess 3D printing for increasing component functionality," *Science*, vol. 353, no. 6307, p. aaf2093, Sep. 2016, doi: 10.1126/science.aaf2093.

[47] M. Rafiee, F. Granier, R. Tao, A. Bhérer-Constant, G. Chenier, and D. Therriault, "Multi-Material, Multi-Process, Planar, and Nonplanar Additive Manufacturing of Piezoelectric Devices," *Adv. Eng. Mater.*, vol. 24, no. 10, p. 2200294, 2022, doi: 10.1002/adem.202200294.

[48] X. Zhou and P. S. Lee, "Three-dimensional printing of tactile sensors for soft robotics," *MRS Bull.*, vol. 46, no. 4, pp. 330–336, Apr. 2021, doi: 10.1557/s43577-021-00079-3.

[49] A. Diouf-Lewis *et al.*, "Design and characterization of carbon fiber-reinforced PEEK/PEI blends for Fused Filament Fabrication additive manufacturing," *Mater. Today Commun.*, vol. 31, p. 103445, Jun. 2022, doi: 10.1016/j.mtcomm.2022.103445.

[50] B. Hu *et al.*, "Improved design of fused deposition modeling equipment for 3D printing of high-performance PEEK parts," *Mech. Mater.*, vol. 137, p. 103139, Oct. 2019, doi: 10.1016/j.mechmat.2019.103139.

[51] H. Jiang, P. Aihemaiti, W. Aiyiti, and A. Kasimu, "Study Of the compression behaviours of 3D-printed PEEK/CFR-PEEK sandwich composite structures," *Virtual Phys. Prototyp.*, vol. 17, no. 2, pp. 138–155, Apr. 2022, doi: 10.1080/17452759.2021.2014636.

[52] H. Vahabi, F. Laoutid, M. Mehrpouya, M. R. Saeb, and P. Dubois, "Flame retardant polymer materials: An update and the future for 3D printing developments," *Mater. Sci. Eng. R Rep.*, vol. 144, p. 100604, Apr. 2021, doi: 10.1016/j.mser.2020.100604.

[53] B. G. Compton, N. S. Hmeidat, R. C. Pack, M. F. Heres, and J. R. Sangoro, "Electrical and Mechanical Properties of 3D-Printed Graphene-Reinforced Epoxy," *JOM*, vol. 70, no. 3, pp. 292–297, Mar. 2018, doi: 10.1007/s11837-017-2707-x.

[54] J. Hu, "Study on STL-based Slicing Process for 3D Printing," in *Proceedings of the 28th Annual International Solid Freeform Fabrication Symposium – An Additive Manufacturing Conference*, Austin, Texas, Oct. 2017, p. 11.

[55] RepRap contributors, "G-code - RepRap," *RepRap Wiki*, Jan. 17, 2020. https://reprap.org/mediawiki/index.php?title=G-code&oldid=187302 (accessed Jan. 18, 2020).

[56] G. A. Nisja, A. Cao, and C. Gao, “Short review of nonplanar fused deposition modeling printing,” *Mater. Des. Process. Commun.*, vol. 3, no. 4, p. e221, 2021, doi: 10.1002/mdp2.221.

[57] L. Chen, M.-F. Chung, Y. Tian, A. Joneja, and K. Tang, “Variable-depth curved layer fused deposition modeling of thin-shells,” *Robot. Comput.-Integr. Manuf.*, vol. 57, pp. 422–434, Jun. 2019, doi: 10.1016/j.rcim.2018.12.016.

[58] H. Zhao, Y. He, J. Fu, and J. Qiu, “Inclined layer printing for fused deposition modeling without assisted supporting structure,” *Robot. Comput.-Integr. Manuf.*, vol. 51, pp. 1–13, Jun. 2018, doi: 10.1016/j.rcim.2017.11.011.

[59] B. Huang and S. B. Singamneni, “Curved Layer Adaptive Slicing (CLAS) for fused deposition modelling,” *Rapid Prototyp. J.*, vol. 21, no. 4, pp. 354–367, Jun. 2015, doi: 10.1108/RPJ-06-2013-0059.

[60] D. Ahlers, F. Wasserfall, N. Hendrich, and J. Zhang, “3D Printing of Nonplanar Layers for Smooth Surface Generation,” Master thesis, Universität Hamburg, Hamburg, Germany, 2019. Accessed: Oct. 06, 2019. [Online]. Available: https://ieeexplore.ieee.org/document/8843116/

[61] G. Boutin, “Non-planar. Nonplanar.xyz,” *nonplanar.xyz*. https://www.nonplanar.xyz (accessed Feb. 02, 2023).

[62] L. Pelzer and C. Hopmann, “Additive Manufacturing of Non-Planar Layers with Variable Layer Height,” *Addit. Manuf.*, p. 101697, Nov. 2020, doi: 10.1016/j.addma.2020.101697.

[63] F. Alkadi, K.-C. Lee, A. H. Bashiri, and J.-W. Choi, “Conformal additive manufacturing using a direct-print process,” *Addit. Manuf.*, vol. 32, p. 100975, Mar. 2020, doi: 10.1016/j.addma.2019.100975.

[64] G. Fang, T. Zhang, S. Zhong, X. Chen, Z. Zhong, and C. C. L. Wang, “Reinforced FDM: multi-axis filament alignment with controlled anisotropic strength,” *ACM Trans. Graph.*, vol. 39, no. 6, pp. 1–15, Nov. 2020, doi: 10.1145/3414685.3417834.

[65] G. Zhao, G. Ma, J. Feng, and W. Xiao, “Nonplanar slicing and path generation methods for robotic additive manufacturing,” *Int. J. Adv. Manuf. Technol.*, vol. 96, no. 9–12, pp. 3149–3159, Jun. 2018, doi: 10.1007/s00170-018-1772-9.

[66] D. Ding, Z. Pan, D. Cuiuri, H. Li, N. Larkin, and S. van Duin, “Multi-Direction Slicing of STL Models for Robotic Wire-feed Additive Manufacturing,” presented at the International Solid Freeform Fabrication Symposium 2015, Aug. 2015, p. 12.

[67] A. Gleadall, “FullControl GCode Designer - open-source software for unconstrained design in additive manufacturing,” *Addit. Manuf.*, p. 102109, Jun. 2021, doi: 10.1016/j.addma.2021.102109.

[68] J. C. S. McCaw and E. Cuan-Urquizo, “Curved-Layered Additive Manufacturing of non-planar, parametric lattice structures,” *Mater. Des.*, vol. 160, pp. 949–963, Dec. 2018, doi: 10.1016/j.matdes.2018.10.024.

[69] F. Hong, S. Hodges, C. Myant, and D. Boyle, “Open5x: Accessible 5-axis 3D printing and conformal slicing,” in *CHI Conference on Human Factors in Computing Systems Extended Abstracts*, Apr. 2022, pp. 1–6. doi: 10.1145/3491101.3519782.

[70] D. Zhao, T. Li, B. Shen, Y. Jiang, W. Guo, and F. Gao, “A multi-DOF rotary 3D printer: machine design, performance analysis and process planning of curved layer fused deposition

modeling (CLFDM)," *Rapid Prototyp. J.*, vol. 26, no. 6, pp. 1079–1093, Mar. 2020, doi: 10.1108/RPJ-06-2019-0160.

[71] "Premier robot Unimates en 1961 chez GM en fonderie sous pression - My Little Blog Fonderie," Dec. 05, 2016. http://souspression.canalblog.com/archives/2012/02/01/13561147.html (accessed Jan. 21, 2020).

[72] A. Nubiola, "Contribution to improving the accuracy of serial robots," phd, École de technologie supérieure, Montréal, 2014. Accessed: Jan. 08, 2020. [Online]. Available: http://espace.etsmtl.ca/1432/

[73] J. Nielsen and B. Roth, "Formulation and Solution for the Direct and Inverse Kinematics Problems for Mechanisms and Mechatronics Systems," in *Computational Methods in Mechanical Systems: Mechanism Analysis, Synthesis, and Optimization*, J. Angeles and E. Zakhariev, Eds., in NATO ASI Series. Berlin, Heidelberg: Springer, 1998, pp. 33–52. doi: 10.1007/978-3-662-03729-4_2.

[74] E. Dombre and W. Khalil, Eds., *Modeling, Performance Analysis and Control of Robot Manipulators*. London, UK: ISTE, 2007. doi: 10.1002/9780470612286.

[75] K. Berns and D. Görges, *Advances in Service and Industrial Robotics: Proceedings of the 28th International Conference on Robotics in Alpe-Adria-Danube Region (RAAD 2019)*. 2019. Accessed: Jan. 09, 2020. [Online]. Available: https://doi.org/10.1007/978-3-030-19648-6

[76] A. Ghoul, O. Bachir, and I. K. Bousserhane, "Chapitre I Modélisation des robots manipulateurs," Algeria, 2016, p. 37.

[77] "Handling tool setup and operation manual," FANUC America Corporation, Rochester Hills, Michigan, Documentation manual MAROUHT9102171E REV E, Version 9.10 series, 2018.

[78] A. Gasparetto, P. Boscariol, A. Lanzutti, and R. Vidoni, "Trajectory Planning in Robotics," *Math. Comput. Sci.*, vol. 6, no. 3, pp. 269–279, Sep. 2012, doi: 10.1007/s11786-012-0123-8.

[79] A. Gasparetto, P. Boscariol, A. Lanzutti, and R. Vidoni, "Path Planning and Trajectory Planning Algorithms: A General Overview," in *Motion and Operation Planning of Robotic Systems: Background and Practical Approaches*, G. Carbone and F. Gomez-Bravo, Eds., in Mechanisms and Machine Science. Cham: Springer International Publishing, 2015, pp. 3–27. doi: 10.1007/978-3-319-14705-5_1.

[80] J. Angeles, *Fundamentals of Robotic Mechanical Systems: Theory, Methods, and Algorithms; Second Edition*, 2nd ed. in Mechanical Engineering Series. Montreal: Springer, 2002.

[81] P. Urhal, A. Weightman, C. Diver, and P. Bartolo, "Robot assisted additive manufacturing: A review," *Robot. Comput.-Integr. Manuf.*, vol. 59, pp. 335–345, Oct. 2019, doi: 10.1016/j.rcim.2019.05.005.

[82] P. M. Bhatt, R. K. Malhan, A. V. Shembekar, Y. J. Yoon, and S. K. Gupta, "Expanding capabilities of additive manufacturing through use of robotics technologies: A survey," *Addit. Manuf.*, vol. 31, p. 100933, Jan. 2020, doi: 10.1016/j.addma.2019.100933.

[83] C. Gosselin, R. Duballet, Ph. Roux, N. Gaudillière, J. Dirrenberger, and Ph. Morel, "Large-scale 3D printing of ultra-high performance concrete – a new processing route for architects and builders," *Mater. Des.*, vol. 100, pp. 102–109, Jun. 2016, doi: 10.1016/j.matdes.2016.03.097.

[84] R. A. Buswell, W. R. Leal de Silva, S. Z. Jones, and J. Dirrenberger, "3D printing using concrete extrusion: A roadmap for research," *Cem. Concr. Res.*, vol. 112, pp. 37–49, Oct. 2018, doi: 10.1016/j.cemconres.2018.05.006.

[85] S. Huang, W. Xu, and Y. Li, "The impacts of fabrication systems on 3D concrete printing building forms," *Front. Archit. Res.*, vol. 11, no. 4, pp. 653–669, Aug. 2022, doi: 10.1016/j.foar.2022.03.004.

[86] N. D. Watson, N. A. Meisel, S. G. Bilén, J. Duarte, and S. Nazarian, "Large-Scale Additive Manufacturing of Concrete Using a 6-Axis Robotic Arm for Autonomous Habitat Construction," in *Proceedings of the 30th Annual International Solid Freeform Fabrication Symposium*, University of Texas at Austin, 2019. doi: 10.26153/tsw/17383.

[87] C. Scott, "Relativity Space 3D Prints 11-Foot-Tall Fuel Tank with Stargate 3D Printer - 3DPrint.com | The Voice of 3D Printing / Additive Manufacturing," *3dprint.com*, Dec. 12, 2018. https://3dprint.com/231703/relativity-space-3d-prints-fuel-tank/ (accessed Feb. 02, 2023).

[88] "High Performance 3D Printer Extruders, Hotends & Parts," *DYZE DESIGN*. https://dyzedesign.com/ (accessed Feb. 03, 2023).

[89] "CEAD B.V. | Large Scale 3D Printing | Robot & Gantry Systems," *CEAD | Large Scale Additive Manufacturing*. https://ceadgroup.com/ (accessed Feb. 03, 2023).

[90] "Pellet 3D Printers & Extruders – Buyer's Guide," *All3DP Pro*, Oct. 27, 2022. https://all3dp.com/1/cheaper-3d-printing-with-pellets/ (accessed Feb. 03, 2023).

[91] "KUKA & Ai Build Launch 3D Printing Production Cells - 3DPrint.com | The Voice of 3D Printing / Additive Manufacturing." https://3dprint.com/295756/d-ai-build-kuka-launch-3d-printing-production-cells/ (accessed Feb. 03, 2023).

[92] "Ai Build | Additive Manufacturing Software." https://ai-build.com/ (accessed Feb. 03, 2023).

[93] G. Q. Zhang, W. Mondesir, C. Martinez, X. Li, T. A. Fuhlbrigge, and H. Bheda, "Robotic additive manufacturing along curved surface — A step towards free-form fabrication," in *2015 IEEE International Conference on Robotics and Biomimetics (ROBIO)*, Zhuhai: IEEE, Dec. 2015, pp. 721–726. doi: 10.1109/ROBIO.2015.7418854.

[94] P. M. Bhatt *et al.*, "A Robotic Cell for Multi-Resolution Additive Manufacturing," in *2019 International Conference on Robotics and Automation (ICRA)*, May 2019, pp. 2800–2807. doi: 10.1109/ICRA.2019.8793730.

[95] N. R. Fry, R. C. Richardson, and J. H. Boyle, "Robotic additive manufacturing system for dynamic build orientations," *Rapid Prototyp. J.*, vol. ahead-of-print, no. ahead-of-print, Jan. 2020, doi: 10.1108/RPJ-09-2019-0243.

[96] B. H. Jafari and N. Gans, “Surface Parameterization and Trajectory Generation on Regular Surfaces With Application in Robot-Guided Deposition Printing,” *IEEE Robot. Autom. Lett.*, vol. 5, no. 4, pp. 6113–6120, Oct. 2020, doi: 10.1109/LRA.2020.3010454.

[97] A. Nubiola and I. A. Bonev, “Absolute calibration of an ABB IRB 1600 robot using a laser tracker,” *Robot. Comput.-Integr. Manuf.*, vol. 29, no. 1, pp. 236–245, Feb. 2013, doi: 10.1016/j.rcim.2012.06.004.

[98] D. Kraljić, M. Štefanič, and R. Kamnik, “3D Printing with 6D of Freedom: Controlling Material Extrusion Speed,” in *Advances in Service and Industrial Robotics*, K. Berns and D. Görges, Eds., in Advances in Intelligent Systems and Computing. Cham: Springer International Publishing, 2020, pp. 170–178. doi: 10.1007/978-3-030-19648-6_20.

[99] C. Dai, S. Lefebvre, K.-M. Yu, J. M. P. Geraedts, and C. C. L. Wang, “Planning Jerk-Optimized Trajectory with Discrete-Time Constraints for Redundant Robots,” *ArXiv190906570 Cs*, Sep. 2019, Accessed: Jan. 08, 2020. [Online]. Available: http://arxiv.org/abs/1909.06570

[100] M. Safeea, R. Bearee, and P. Neto, “An integrated framework for collaborative robot-assisted additive manufacturing,” *J. Manuf. Process.*, vol. 81, pp. 406–413, Sep. 2022, doi: 10.1016/j.jmapro.2022.06.067.

[101] M. A. Skylar-Scott, J. Mueller, C. W. Visser, and J. A. Lewis, “Voxelated soft matter via multimaterial multinozzle 3D printing,” *Nature*, vol. 575, no. 7782, pp. 330–335, Nov. 2019, doi: 10.1038/s41586-019-1736-8.

[102] Y. J. Yoon, M. Yon, S. E. Jung, and S. K. Gupta, “Development of Three-Nozzle Extrusion System for Conformal Multi-Resolution 3D Printing with a Robotic Manipulator,” in *Volume 1: 39th Computers and Information in Engineering Conference*, Anaheim, California, USA: American Society of Mechanical Engineers, Aug. 2019, p. V001T02A024. doi: 10.1115/DETC2019-98069.

[103] B. P. Croom *et al.*, “Mechanics of nozzle clogging during direct ink writing of fiber-reinforced composites,” *Addit. Manuf.*, p. 101701, Nov. 2020, doi: 10.1016/j.addma.2020.101701.

[104] T. Beran, T. Mulholland, F. Henning, N. Rudolph, and T. A. Osswald, “Nozzle clogging factors during fused filament fabrication of spherical particle filled polymers,” *Addit. Manuf.*, vol. 23, pp. 206–214, Oct. 2018, doi: 10.1016/j.addma.2018.08.009.

[105] X. Zhao, J. R. G. Evans, M. J. Edirisinghe, and J. H. Song, “Ceramic Freeforming Using an Advanced Multinozzle Ink-Jet Printer,” *J. Mater. Synth. Process.*, vol. 9, no. 6, pp. 319–327, Nov. 2001, doi: 10.1023/A:1016352522493.

[106] J.-S. Lee *et al.*, “Design and evaluation of a silicon based multi-nozzle for addressable jetting using a controlled flow rate in electrohydrodynamic jet printing,” *Appl. Phys. Lett.*, vol. 93, no. 24, p. 243114, Dec. 2008, doi: 10.1063/1.3049609.

[107] R. J. Chesterfield *et al.*, “63.3: Multinozzle Printing: A Cost-Effective Process for OLED Display Fabrication,” *SID Symp. Dig. Tech. Pap.*, vol. 40, no. 1, pp. 951–954, 2009, doi: 10.1889/1.3256956.

[108] A. Khan, K. Rahman, D. S. Kim, and K. H. Choi, “Direct printing of copper conductive micro-tracks by multi-nozzle electrohydrodynamic inkjet printing process,” *J. Mater. Process. Technol.*, vol. 212, no. 3, pp. 700–706, Mar. 2012, doi: 10.1016/j.jmatprotec.2011.10.024.

[109] Y. Yan, Z. Xiong, Y. Hu, S. Wang, R. Zhang, and C. Zhang, “Layered manufacturing of tissue engineering scaffolds via multi-nozzle deposition,” *Mater. Lett.*, vol. 57, no. 18, pp. 2623–2628, May 2003, doi: 10.1016/S0167-577X(02)01339-3.

[110] Z. Chen *et al.*, “3D multi-nozzle system with dual drives highly potential for 3D complex scaffolds with multi-biomaterials,” *Int. J. Precis. Eng. Manuf.*, vol. 18, no. 5, pp. 755–761, May 2017, doi: 10.1007/s12541-017-0090-8.

[111] S. Khalil, J. Nam, and W. Sun, “Multi-nozzle deposition for construction of 3D biopolymer tissue scaffolds,” *Rapid Prototyp. J. Bradf.*, vol. 11, no. 1, pp. 9–17, 2005, doi: http://dx.doi.org/10.1108/13552540510573347.

[112] X. Wang, Y. Yan, and R. Zhang, “Recent trends and challenges in complex organ manufacturing,” *Tissue Eng. Part B Rev.*, vol. 16, no. 2, pp. 189–197, Apr. 2010, doi: 10.1089/ten.TEB.2009.0576.

[113] C. D. Meinhart and H. Zhang, “The flow structure inside a microfabricated inkjet printhead,” *J. Microelectromechanical Syst.*, vol. 9, no. 1, pp. 67–75, Mar. 2000, doi: 10.1109/84.825779.

[114] S. Khalil and W. Sun, “Biopolymer deposition for freeform fabrication of hydrogel tissue constructs,” *Mater. Sci. Eng. C*, vol. 27, no. 3, pp. 469–478, Apr. 2007, doi: 10.1016/j.msec.2006.05.023.

[115] D. Therriault, R. F. Shepherd, S. R. White, and J. A. Lewis, “Fugitive Inks for Direct-Write Assembly of Three-Dimensional Microvascular Networks,” *Adv. Mater.*, vol. 17, no. 4, pp. 395–399, Feb. 2005, doi: 10.1002/adma.200400481.

[116] P. M. Bhatt, A. Kulkarni, R. K. Malhan, B. C. Shah, Y. J. Yoon, and S. K. Gupta, “Automated Planning for Robotic Multi-Resolution Additive Manufacturing,” *J. Comput. Inf. Sci. Eng.*, vol. 22, no. 2, p. 021006, Apr. 2022, doi: 10.1115/1.4052083.

[117] “E3D Kraken - 4 Hotend Extrusion Complete kit,” *Digitmakers.ca*. https://www.digitmakers.ca/products/e3d-kraken-4-hotend-extrusion (accessed Feb. 04, 2023).

[118] D. Baca and R. Ahmad, “The impact on the mechanical properties of multi-material polymers fabricated with a single mixing nozzle and multi-nozzle systems via fused deposition modeling,” *Int. J. Adv. Manuf. Technol.*, vol. 106, no. 9, pp. 4509–4520, Feb. 2020, doi: 10.1007/s00170-020-04937-3.

[119] P. S. Mhatre, “Process Planning for Concurrent Multi-Nozzle 3D Printing,” M.S., Rochester Institute of Technology, United States -- New York, 2019. Accessed: Feb. 04, 2023. [Online]. Available: https://www.proquest.com/docview/2239303067/abstract/3CBAA35E2574433APQ/1

[120] S. G. M. Uzel, R. D. Weeks, M. Eriksson, D. Kokkinis, and J. A. Lewis, “Multimaterial Multinozzle Adaptive 3D Printing of Soft Materials,” *Adv. Mater. Technol.*, vol. n/a, no. n/a, p. 2101710, 2022, doi: 10.1002/admt.202101710.

[121] A. Khan, K. Rahman, S. Ali, S. Khan, B. Wang, and A. Bermak, “Fabrication of circuits by multi-nozzle electrohydrodynamic inkjet printing for soft wearable electronics,” *J. Mater. Res.*, vol. 36, no. 18, pp. 3568–3578, Sep. 2021, doi: 10.1557/s43578-021-00188-4.

[122] R. Rajendran, “Gas turbine coatings – An overview,” *Eng. Fail. Anal.*, vol. 26, pp. 355–369, Dec. 2012, doi: 10.1016/j.engfailanal.2012.07.007.

[123] W. H. Xue, S. Y. Gao, D. L. Duan, Y. Liu, and S. Li, “Material transfer behaviour between a Ti6Al4V blade and an aluminium hexagonal boron nitride abradable coating during high-speed rubbing,” *Wear*, vol. 322–323, pp. 76–90, Jan. 2015, doi: 10.1016/j.wear.2014.10.001.

[124] H. Ma, F. Yin, Y. Guo, X. Tai, and B. Wen, “A review on dynamic characteristics of blade–casing rubbing,” *Nonlinear Dyn.*, vol. 84, no. 2, pp. 437–472, Apr. 2016, doi: 10.1007/s11071-015-2535-x.

[125] X. Ma and A. Matthews, “Investigation of abradable seal coating performance using scratch testing,” *Surf. Coat. Technol.*, vol. 202, no. 4–7, pp. 1214–1220, Dec. 2007, doi: 10.1016/j.surfcoat.2007.07.076.

[126] N. Fois, J. Stringer, and M. B. Marshall, “Adhesive transfer in aero-engine abradable linings contact,” *Wear*, vol. 304, no. 1, pp. 202–210, Jul. 2013, doi: 10.1016/j.wear.2013.04.033.

[127] M. Bounazef, S. Guessasma, and B. Ait Saadi, “The wear, deterioration and transformation phenomena of abradable coating BN–SiAl–bounding organic element, caused by the friction between the blades and the turbine casing,” *Mater. Lett.*, vol. 58, no. 27–28, pp. 3375–3380, Nov. 2004, doi: 10.1016/j.matlet.2004.02.049.

[128] Y.-Q. Tong, W. Li, Q.-S. Shi, L. Chen, and G.-J. Yang, “Self-lubricating epoxy-based composite abradable seal coating eliminating adhesive transfer via hierarchical design,” *J. Mater. Sci. Technol.*, vol. 104, pp. 145–154, Mar. 2022, doi: 10.1016/j.jmst.2021.07.017.

[129] S. Wilson, “Thermally sprayed abradable coating technology for sealing in gas turbines,” presented at the The Future of Gas Turbine Technology, 6th International Conference, Brussels, Belgium: Oerlikon Merco, Oct. 2012.

[130] J. Stringer and M. B. Marshall, “High speed wear testing of an abradable coating,” *Wear*, vol. 294–295, pp. 257–263, Jul. 2012, doi: 10.1016/j.wear.2012.07.009.

[131] N. Salvat, A. Batailly, and M. Legrand, “Modeling of Abradable Coating Removal in Aircraft Engines Through Delay Differential Equations,” in *Volume 7B: Structures and Dynamics*, San Antonio, Texas, USA: ASME, Jun. 2013, p. V07BT31A007. doi: 10.1115/GT2013-94400.

[132] F. Ghasripoor, R. Schmid, and M. Dorfman, “Abradable Coatings Increase Gas Turbine Engine Efficiency,” *Mater. World*, vol. 5, no. 6, pp. 328–30, Jun. 1997.

[133] D. P. Rose, G. D. Price, and A. Bosna, “Development of a Nonmetallic Abradable Material System for Gas Turbine Applications,” presented at the ASME 1993 International Gas Turbine and Aeroengine Congress and Exposition, American Society of Mechanical Engineers Digital Collection, Feb. 2015. doi: 10.1115/93-GT-425.

[134] “3M™ Scotch-Weld™ Void Filling Compound EC-3524 B/A Black, 1kg Kit, 2/cs,” *3M*, 2019. https://www.3m.com/3M/en_US/p/d/b40067619/ (accessed Feb. 04, 2020).

[135] C. U. Hardwicke and Y.-C. Lau, “Advances in Thermal Spray Coatings for Gas Turbines and Energy Generation: A Review,” *J. Therm. Spray Technol.*, vol. 22, no. 5, pp. 564–576, Jun. 2013, doi: 10.1007/s11666-013-9904-0.

[136] U. Batra, “Thermal spray coating of abradable Ni based composite,” *Surf. Eng.*, vol. 25, no. 4, pp. 284–286, May 2009, doi: 10.1179/174329407X215087.

[137] E. R. Fotsing, A. Dubourg, A. Ross, and J. Mardjono, “Acoustic properties of periodic micro-structures obtained by additive manufacturing,” *Appl. Acoust.*, vol. 148, pp. 322–331, May 2019, doi: 10.1016/j.apacoust.2018.12.030.

[138] D. L. Johnson, J. Koplik, and R. Dashen, “Theory of dynamic permeability and tortuosity in fluid-saturated porous media,” *J. Fluid Mech.*, vol. 176, pp. 379–402, Mar. 1987, doi: 10.1017/S0022112087000727.

[139] Y. Champoux and J. Allard, “Dynamic tortuosity and bulk modulus in air-saturated porous media,” *J. Appl. Phys.*, vol. 70, no. 4, pp. 1975–1979, Aug. 1991, doi: 10.1063/1.349482.

[140] D. Lafarge, P. Lemarinier, J. F. Allard, and V. Tarnow, “Dynamic compressibility of air in porous structures at audible frequencies,” *J. Acoust. Soc. Am.*, vol. 102, no. 4, pp. 1995–2006, Oct. 1997, doi: 10.1121/1.419690.

[141] R. D. Farahani, L. L. Lebel, and D. Therriault, “Processing parameters investigation for the fabrication of self-supported and freeform polymeric microstructures using ultraviolet-assisted three-dimensional printing,” *J. Micromechanics Microengineering*, vol. 24, no. 5, p. 055020, May 2014, doi: 10.1088/0960-1317/24/5/055020.

[142] C. Xu, B. Quinn, L. L. Lebel, D. Therriault, and G. L’Espérance, “Multi-Material Direct Ink Writing (DIW) for Complex 3D Metallic Structures with Removable Supports,” *ACS Appl. Mater. Interfaces*, vol. 11, no. 8, pp. 8499–8506, Feb. 2019, doi: 10.1021/acsami.8b19986.

[143] E. Ghafar-Zadeh, M. Sawan, and D. Therriault, “A Microfluidic Packaging Technique for Lab-on-Chip Applications,” *IEEE Trans. Adv. Packag.*, vol. 32, no. 2, pp. 410–416, May 2009, doi: 10.1109/TADVP.2008.920655.

[144] B. Li, P. A. Clark, and K. H. Church, “Robust Direct-Write Dispensing Tool and Solutions for Micro/Meso-Scale Manufacturing and Packaging,” in *Proceedings of the 2007 International Manufacturing Science And Engineering Conference*, Atlanta, Georgia, USA, Oct. 2007, p. 7.

[145] L. Griffiths, “Certified 3D printed WAAMpeller signals future for marine parts on demand,” *TCT Magazine*, Dec. 01, 2017. https://www.tctmagazine.com/api/content/f9d8bb4a-d69e-11e7-8990-121bebc5777e/ (accessed Mar. 18, 2020).

[146] L. Yuan *et al.*, “Fabrication of metallic parts with overhanging structures using the robotic wire arc additive manufacturing,” *J. Manuf. Process.*, Apr. 2020, doi: 10.1016/j.jmapro.2020.03.018.

[147] Y. Li, X. Qin, Q. Wu, Z. Hu, and T. Shao, “Fabrication of curved overhanging thin-walled structure with robotic wire and arc additive manufacturing (RWAAM),” *Ind. Robot Int. J. Robot. Res. Appl.*, vol. 47, no. 1, pp. 102–110, Aug. 2019, doi: 10.1108/IR-05-2019-0112.

[148] D. Therriault, “Directed Assembly of Three-Dimensional Microvascular Networks,” PhD thesis, University of Illinois at Urbana-Champaign, Urbana, Illinois, 2003.

[149] V. Tlach, Z. Ságová, and I. Kuric, "Circular and quasi-circular paths for the industrial robots measuring with the Renishaw Ballbar QC20-W," *MATEC Web Conf.*, vol. 254, p. 05007, 2019, doi: 10.1051/matecconf/201925405007.

[150] J. Boulvert *et al.*, "Optimally graded porous material for broadband perfect absorption of sound," *J. Appl. Phys.*, vol. 126, no. 17, p. 175101, Nov. 2019, doi: 10.1063/1.5119715.

[151] C. J. Hansen, W. Wu, K. S. Toohey, N. R. Sottos, S. R. White, and J. A. Lewis, "Self-Healing Materials with Interpenetrating Microvascular Networks," *Adv. Mater.*, vol. 21, no. 41, pp. 4143–4147, 2009, doi: 10.1002/adma.200900588.

[152] G. Postiglione, M. Alberini, S. Leigh, M. Levi, and S. Turri, "Effect of 3D-Printed Microvascular Network Design on the Self-Healing Behavior of Cross-Linked Polymers," *ACS Appl. Mater. Interfaces*, vol. 9, no. 16, pp. 14371–14378, Apr. 2017, doi: 10.1021/acsami.7b01830.

[153] A. Papacharalampopoulos, H. Bikas, and P. Stavropoulos, "Path planning for the infill of 3D printed parts utilizing Hilbert curves," *Procedia Manuf.*, vol. 21, pp. 757–764, Jan. 2018, doi: 10.1016/j.promfg.2018.02.181.

[154] S. Bodkhe, G. Turcot, F. P. Gosselin, and D. Therriault, "One-Step Solvent Evaporation-Assisted 3D Printing of Piezoelectric PVDF Nanocomposite Structures," *ACS Appl. Mater. Interfaces*, vol. 9, no. 24, pp. 20833–20842, Jun. 2017, doi: 10.1021/acsami.7b04095.

[155] T. Yamashita and T. Kobayashi, "Smart Table Tennis Racket Using a Rubber Mounted Ultrathin Piezoelectric Sensor Array," *Sens. Mater.*, vol. 33, no. 3, p. 1081, Mar. 2021, doi: 10.18494/SAM.2021.2954.

[156] G. Zhao, G. Ma, J. Feng, and W. Xiao, "Nonplanar slicing and path generation methods for robotic additive manufacturing," *Int. J. Adv. Manuf. Technol.*, vol. 96, no. 9–12, pp. 3149–3159, Jun. 2018, doi: 10.1007/s00170-018-1772-9.

[157] L. Li, A. Haghighi, and Y. Yang, "A novel 6-axis hybrid additive-subtractive manufacturing process: Design and case studies," *J. Manuf. Process.*, vol. 33, pp. 150–160, Jun. 2018, doi: 10.1016/j.jmapro.2018.05.008.

[158] J.-F. Chauvette, D. Brzeski, I. L. Hia, R. D. Farahani, N. Piccirelli, and D. Therriault, "High-speed multinozzle additive manufacturing and extrusion modeling of large-scale microscaffold networks," *Addit. Manuf.*, p. 102294, Sep. 2021, doi: 10.1016/j.addma.2021.102294.

[159] F. Jiang, M. Zhou, and D. Drummer, "Effects of Fumed Silica on Thixotropic Behavior and Processing Window by UV-Assisted Direct Ink Writing," *Polymers*, vol. 14, no. 15, Art. no. 15, Jan. 2022, doi: 10.3390/polym14153107.

[160] "3iTT test: Anton Paar Wiki," *Anton Paar*. https://wiki.anton-paar.com/ca-en/3itt-test/ (accessed Jul. 19, 2022).

[161] O. S. Toker, S. Karasu, M. T. Yilmaz, and S. Karaman, "Three interval thixotropy test (3ITT) in food applications: A novel technique to determine structural regeneration of mayonnaise under different shear conditions," *Food Res. Int.*, vol. 70, pp. 125–133, Apr. 2015, doi: 10.1016/j.foodres.2015.02.002.

[162] S. G. Marapureddy *et al.*, “Rheology and direct write printing of chitosan - graphene oxide nanocomposite hydrogels for differentiation of neuroblastoma cells,” *Carbohydr. Polym.*, vol. 269, p. 118254, Oct. 2021, doi: 10.1016/j.carbpol.2021.118254.

[163] “7 Scan to CAD Alignment Methods in GOM Inspect Software.” https://www.capture3d.com/knowledge-center/blog/gom-inspect-scan-to-cad-alignment (accessed Oct. 27, 2022).

[164] J. Tabak, *Geometry: The Language of Space and Form*. Infobase Publishing, 2014.

[165] P. Ramachandran and G. Varoquaux, “Mayavi: 3D Visualization of Scientific Data,” *Comput. Sci. Eng.*, vol. 13, no. 2, pp. 40–51, Mar. 2011, doi: 10.1109/MCSE.2011.35.

[166] O. R. Bingol and A. Krishnamurthy, “NURBS-Python: An open-source object-oriented NURBS modeling framework in Python,” *SoftwareX*, vol. 9, pp. 85–94, Jan. 2019, doi: 10.1016/j.softx.2018.12.005.

[167] C. Duty *et al.*, “What makes a material printable? A viscoelastic model for extrusion-based 3D printing of polymers,” *J. Manuf. Process.*, vol. 35, pp. 526–537, Oct. 2018, doi: 10.1016/j.jmapro.2018.08.008.

[168] T. Serra, J. A. Planell, and M. Navarro, “High-resolution PLA-based composite scaffolds via 3-D printing technology,” *Acta Biomater.*, vol. 9, no. 3, pp. 5521–5530, Mar. 2013, doi: 10.1016/j.actbio.2012.10.041.

[169] J. Costa-Baptista, E. R. Fotsing, J. Mardjono, D. Therriault, and A. Ross, “Design and fused filament fabrication of multilayered microchannels for subwavelength and broadband sound absorption,” *Addit. Manuf.*, vol. 55, p. 102777, Jul. 2022, doi: 10.1016/j.addma.2022.102777.

[170] D. L. Ramírez-Gutiérrez, E. Cuan-Urquizo, and A. Gómez-Espinosa, “Adaptable Bed for Curved-Layered Fused Deposition Modeling of Nonplanar Structures: A Proof of Concept,” *3D Print. Addit. Manuf.*, vol. 7, no. 4, pp. 198–201, Aug. 2020, doi: 10.1089/3dp.2019.0086.

[171] B. Zhang, A. Gleadall, P. Belton, T. Mcdonagh, R. Bibb, and S. Qi, “New insights into the effects of porosity, pore length, pore shape and pore alignment on drug release from extrusion-based additive manufactured pharmaceuticals,” *Addit. Manuf.*, p. 102196, Jul. 2021, doi: 10.1016/j.addma.2021.102196.

[172] Y. Hwang and R. N. Candler, “Non-planar PDMS microfluidic channels and actuators: a review,” *Lab. Chip*, vol. 17, no. 23, pp. 3948–3959, 2017, doi: 10.1039/C7LC00523G.

[173] M. Stanojevic, “Proof of the Hero’s formula according to R. Boscovich,” in *Mathematical Communications*, Osijek: Croatian Mathematical Society - Division Osijek, Nov. 1996, p. 83.

[174] R. D. Farahani, M. Dubé, and D. Therriault, “Three-Dimensional Printing of Multifunctional Nanocomposites: Manufacturing Techniques and Applications,” *Adv. Mater.*, vol. 28, no. 28, pp. 5794–5821, 2016, doi: 10.1002/adma.201506215.

[175] B. G. Compton, B. K. Post, C. E. Duty, L. Love, and V. Kunc, “Thermal analysis of additive manufacturing of large-scale thermoplastic polymer composites,” *Addit. Manuf.*, vol. 17, pp. 77–86, Oct. 2017, doi: 10.1016/j.addma.2017.07.006.

[176] C. E. Duty *et al.*, “Structure and mechanical behavior of Big Area Additive Manufacturing (BAAM) materials,” *Rapid Prototyp. J.*, vol. 23, no. 1, pp. 181–189, 2017, doi: 10.1108/RPJ-12-2015-0183.

[177] D. J. Roach, C. M. Hamel, C. K. Dunn, M. V. Johnson, X. Kuang, and H. J. Qi, "The m4 3D printer: A multi-material multi-method additive manufacturing platform for future 3D printed structures," *Addit. Manuf.*, vol. 29, p. 100819, Oct. 2019, doi: 10.1016/j.addma.2019.100819.

[178] H. Ren *et al.*, "Smart structures with embedded flexible sensors fabricated by fused deposition modeling-based multimaterial 3D printing," *Int. J. Smart Nano Mater.*, vol. 13, no. 3, pp. 447–464, Jul. 2022, doi: 10.1080/19475411.2022.2095454.

[179] G. L. Goh *et al.*, "Fabrication of design-optimized multifunctional safety cage with conformal circuits for drone using hybrid 3D printing technology," *Int. J. Adv. Manuf. Technol.*, vol. 120, no. 3, pp. 2573–2586, May 2022, doi: 10.1007/s00170-022-08831-y.

[180] N. Cai, P. Sun, and S. Jiang, "Rapid prototyping and customizable multifunctional structures: 3D-printing technology promotes the rapid development of TENGs," *J. Mater. Chem. A*, vol. 9, no. 30, pp. 16255–16280, Aug. 2021, doi: 10.1039/D1TA04092H.

[181] N. van de Werken, H. Tekinalp, P. Khanbolouki, S. Ozcan, A. Williams, and M. Tehrani, "Additively manufactured carbon fiber-reinforced composites: State of the art and perspective," *Addit. Manuf.*, vol. 31, p. 100962, Jan. 2020, doi: 10.1016/j.addma.2019.100962.

[182] J. Pierre, F. Iervolino, R. D. Farahani, N. Piccirelli, M. Lévesque, and D. Therriault, "Material extrusion additive manufacturing of multifunctional sandwich panels with load-bearing and acoustic capabilities for aerospace applications," *Addit. Manuf.*, vol. 61, p. 103344, Jan. 2023, doi: 10.1016/j.addma.2022.103344.

[183] G. Szczepański, M. Podlesna, and K. Lada, "The study of the acoustical properties of a 3D printed noise barrier," in *INTER-NOISE and NOISE-CON Congress and Conference Proceedings*, Glasgow, Scotland: Institute of Noise Control Engineering, Feb. 2023, pp. 4904–4910. doi: 10.3397/IN_2022_0710.

[184] G. D. Goh, S. J. C. Neo, V. Dikshit, and W. Y. Yeong, "Quasi-static indentation and sound-absorbing properties of 3D printed sandwich core panels," *J. Sandw. Struct. Mater.*, vol. 24, no. 2, pp. 1206–1225, Feb. 2022, doi: 10.1177/10996362211037015.

[185] İ. Türkoğlu and M. Yazıcı, "Acoustic Performance of 3D Printed Auxetic Core Sandwich Structures," presented at the 9th International Congress On Engineering, Architecture And Design, Istanbul, Turkey: Bursa Uludag University, May 2022, pp. 1–11. Accessed: Apr. 23, 2023. [Online]. Available: https://avesis.uludag.edu.tr/yayin/65933a97-6c56-420d-b035-f99fb2262af5/acoustic-performance-of-3d-printed-auxetic-core-sandwich-structures

[186] Y.-Q. Tong, "Lightweight epoxy-based abradable seal coating with high bonding strength," *J. Mater. Sci.*, p. 9, 2021.

[187] O. Rios *et al.*, "3D printing via ambient reactive extrusion," *Mater. Today Commun.*, vol. 15, pp. 333–336, Jun. 2018, doi: 10.1016/j.mtcomm.2018.02.031.

[188] B. Wang, Z. Zhang, Z. Pei, J. Qiu, and S. Wang, "Current progress on the 3D printing of thermosets," *Adv. Compos. Hybrid Mater.*, vol. 3, no. 4, pp. 462–472, Dec. 2020, doi: 10.1007/s42114-020-00183-z.

[189] J.-F. Chauvette, I. L. Hia, R. D. Farahani, R. Plante, N. Piccirelli, and D. Therriault, “Non-planar multinozzle additive manufacturing of thermoset composite microscaffold networks,” *Compos. Part B Eng.*, p. 110627, Feb. 2023, doi: 10.1016/j.compositesb.2023.110627.

[190] F. Iervolino, “Additive Manufacturing of Low and High Temperature Resistant Thermoplastic Composites and Sandwich Panels for Sound Absorption,” Master thesis, Polytechnique Montréal, Montréal, Canada, 2019.

[191] A. M. Tomuta, X. Ramis, F. Ferrando, and A. Serra, “The use of dihydrazides as latent curing agents in diglycidyl ether of bisphenol A coatings,” *Prog. Org. Coat.*, vol. 74, no. 1, pp. 59–66, May 2012, doi: 10.1016/j.porgcoat.2011.10.004.

[192] J. Gotro, “Epoxy Curing Agents – Latent Curing Agents for One Component Systems,” *Polymer Innovation Blog*, Sep. 12, 2022. https://polymerinnovationblog.com/epoxy-curing-agents-latent-curing-agents-for-one-component-systems/ (accessed Feb. 18, 2023).

[193] S. D. Vacche, V. Michaud, M. Demierre, P.-E. Bourban, and J.-A. E. Månson, “Curing kinetics and thermomechanical properties of latent epoxy/carbon fiber composites,” *IOP Conf. Ser. Mater. Sci. Eng.*, vol. 139, p. 012049, Jul. 2016, doi: 10.1088/1757-899X/139/1/012049.

[194] “The Density of Aluminium and its Alloys - thyssenkrupp Materials (UK),” *Materials UK*, 2022. https://www.thyssenkrupp-materials.co.uk/density-of-aluminium.html (accessed Mar. 04, 2023).

[195] J.-P. Immarigeon, R. T. Holt, A. K. Koul, L. Zhao, W. Wallace, and J. C. Beddoes, “Lightweight materials for aircraft applications,” *Mater. Charact.*, vol. 35, no. 1, pp. 41–67, Jul. 1995, doi: 10.1016/1044-5803(95)00066-6.

[196] M. O. Borel, A. R. Nicoll, H. W. Schla¨pfer, and R. K. Schmid, “The wear mechanisms occurring in abradable seals of gas turbines,” *Surf. Coat. Technol.*, vol. 39–40, pp. 117–126, Dec. 1989, doi: 10.1016/0257-8972(89)90046-7.

[197] F. Nyssen, N. Tableau, D. Lavazec, and A. Batailly, “Experimental and numerical characterization of a ceramic matrix composite shroud segment under impact loading,” *J. Sound Vib.*, vol. 467, p. 115040, Feb. 2020, doi: 10.1016/j.jsv.2019.115040.

[198] J. Boulvert *et al.*, “Acoustic modeling of micro-lattices obtained by additive manufacturing,” *Appl. Acoust.*, vol. 164, p. 107244, Jul. 2020, doi: 10.1016/j.apacoust.2020.107244.

[199] W. Johnston and B. Sharma, “Additive Manufacturing of Fibrous Sound Absorbers,” *Addit. Manuf.*, p. 101984, Mar. 2021, doi: 10.1016/j.addma.2021.101984.

[200] J.-F. Chauvette, D. Brzeski, and D. Therriault, “MEPM.” Feb. 19, 2023. Accessed: Feb. 24, 2023. [Online]. Available: https://github.com/lm2-poly/mepm

[201] J.-F. Chauvette and D. Therriault, “MTG.” Feb. 06, 2023. Accessed: Feb. 24, 2023. [Online]. Available: https://github.com/lm2-poly/mtg

[202] M. Chalvin, F. Wulle, S. Campocasso, A. Elser, V. Hugel, and A. Verl, “Orientation smoothing in multi-axis additive manufacturing,” *Procedia CIRP*, vol. 107, pp. 357–362, May 2022, doi: 10.1016/j.procir.2022.04.058.

[203] G. Thürmer, “Smoothing Normal Vectors on Discrete Surfaces While Preserving Slope Discontinuities,” *Comput. Graph. Forum*, vol. 20, no. 2, pp. 103–114, 2001, doi: 10.1111/1467-8659.00482.